



DRAFT

**Attachment 2
ATBD – Limb Profile (IN0092A-107)**

Document Number – IN0092A-107
CI Number – SS0050A
Date: 6 April 1999



**ALGORITHM THEORETICAL BASIS DOCUMENT (ATBD)
(LIMB PROFILE OZONE)**

FOR THE

**Ozone Mapping and Profiler Suite (OMPS)
Of the
National Polar-Orbiting Operational Environmental
Satellite System (NPOESS) Program**

**Contract Number: F04701-99-C-0044
CDRL A012**

**PREPARED FOR:
NPOESS Program Office**

**Prepared by
Ball Aerospace Systems Division (BASD)
Boulder, CO 80306
CAGE Code 13993**

PREPARED BY

Jack Larsen

OMPS-RSTX-Engineer

APPROVED:

Juan Rodriguez

OMPS-Systems Engineer

APPROVED:

Vince Minerva

OMPS Program Manager

Project Release _____

**Revision Record**

Revision	Date	Reasons for Revision	Project Released Date
Draft	March 1, 1999	1 st Draft Release	
Revised Draft	April 6, 1999	Proposal Modifications	



Table of Contents

1	INTRODUCTION.....	5
1.1	System Description	5
1.2	Objectives.....	6
1.3	Scope	6
1.4	Overview	7
1.5	Data Products	7
1.6	Applicable Documents	8
1.6.1	Controlling Documents	8
1.6.2	OMPS Reference Documents.....	8
1.7	Revision History.....	8
1.8	Contributing Authors.....	8
2.	SCIENTIFIC BASIS	9
2.1	Physical Description.....	9
2.2	Sensor Description	10
2.3	Forward Model.....	11
2.3.1	Radiative Transfer Code.....	13
2.3.2	Radiative Transfer Tables	13
2.4	Retrieval	19
2.4.1.	Overview	19
2.4.2	Information Extraction	20
2.4.3	Channel Selection.....	20
2.4.4	Radiance Normalization.....	22
2.4.5	Pair and Triplet Formulations	23
2.4.6	Optimal Estimation	24
2.4.7	Initialization and Setup.....	24
2.4.8	Scene Characterization.....	25
2.4.9.	Neutral Number Density, Inversion and Profile Construction.....	29
2.4.10	Aerosol Inversion	30
2.4.11	Ozone Inversion	30
2.4.12	Convergence Criteria.....	31
2.4.13	Ozone Conversion to Mixing Ratio	32
2.4.14	Horizontal Inhomogeneity Correction	32
2.5	Error Sources.....	37
3.	ALGORITHM DESCRIPTION	38
3.1	SDR Production	38
3.1.1	SDR Description	38
3.1.2	Method	40
3.1.3	Calibration.....	44
3.2	EDR Production	53
4.	ASSUMPTIONS.....	60
5.	INPUT DATA REQUIREMENTS	61
5.1	Primary Sensor Requirements	61
5.2	Other OMPS Sensor Data Requirements	62
5.3	Other NPOESS Sensor Data Requirements	62
5.4	Climatology Data Requirements	62



6. OUTPUT DATA DESCRIPTION	63
6.1 EDRs	63
6.2 Additional Data Products	63
6.3 EDR Content	64
7. SYSTEM ACCURACY AND PRECISION	65
7.1 Profile Accuracy.....	65
7.1.1 Sensor Accuracy Allocations	66
7.1.2 Algorithm Accuracy Allocations	73
7.1.3 Pointing Accuracy Allocations.....	76
7.2 Profile Long Term Stability	77
7.3 Profile Precision	78
7.3.1 Sensor Precision Allocations.....	80
7.3.2 Algorithm Precision Allocations.....	84
7.3.3 Algorithm Altitude Registration Precision Allocation.....	91
7.4 Limb Profile Mapping Uncertainty	96
8 TEST, VALIDATION, AND CALIBRATION	97
8.1 Overview of Plans and Results.....	97
8.2 Simulation and Retrieval Procedures	97
8.2.1 End-to-End Simulations	97
8.3 Test Cases.....	100
8.3.1 Algorithm Performance.....	100
8.3.2 SOLSE/LORE Retrievals.....	100
8.3.3 End-to-End Test Runs	101
8.4 Analysis and Results	101
8.4.1 Algorithm Performance – Monte Carlo Simulations	101
8.4.2 SOLSE/LORE Retrievals.....	101
8.4.3 End-to-End Simulations	106
9 REFERENCES.....	111
APPENDIX A. SOURCE CODE	115



1 Introduction

The Ozone Mapping and Profiler Suite (OMPS) is an important component of the National Polar-Orbiting Operational Environmental Satellite System (NPOESS). The OMPS mission is to provide the NPOESS users with data products that describe the vertical, horizontal and temporal distribution of ozone in the Earth's atmosphere. These data (or Environmental Data Records - EDRs) are derived from the space-borne ultraviolet, visible and near infrared observations of a two sensor system.

1.1 System Description

The nadir system has two focal planes; one operating from 300 to 380 nm for total column ozone observations; the other operating at 250 to 310 nm for profile ozone observations. The limb system has one focal plane operating from 290 to 1000 nm for high vertical resolution profile ozone observations. These systems together with the interface and control electronics are the OMPS sensor suite. Calibrated and un-calibrated sensor data are also provided to the NPOESS users in the form of Sensor Data Records (SDRs) and Raw Data Records (RDRs), respectively. In addition, we use the SDRs from the NPOESS CrIS sensor to generate ozone total column data products for very high solar zenith angles ($>80^\circ$).

The EDR requirements thresholds listed in section 3.2.1.1.1 of the OMPS System Specification, Document Number 542798, shall be met when data from OMPS is processed using the scientific algorithms described in these ATBDs.

The OMPS algorithms include the following:

- 1 **The UV Nadir Total Column Ozone Algorithm** is adapted from the heritage TOMS version 7 algorithm. We have included modular enhancements to meet EDR requirements and to provide for graceful degradation.
- 2 **The UV Nadir Profile Ozone Algorithm** is adopted from the heritage SBUV/2 operational algorithm. The ozone profile from this algorithm not only provides an initialization for the UV/VIS Limb Profile Algorithm but also provides a link to the heritage twenty-year ozone profile data set.
- 3 **The UV/VIS Limb Profile Ozone Algorithm** is adapted from the heritage SOLSE/LORE algorithm. We have included modular enhancements to achieve EDR requirements and to provide graceful degradation.
- 4 **The IR Total Column Ozone Algorithm** is adapted from heritage algorithms used for TOVS, CIRRIS-1A, and EOS-TES data. In order to improve the performance of the ozone retrieval, auxiliary parameters such as temperature and moisture profiles, surface emissivity, and surface skin temperature are retrieved simultaneously with the ozone column amount. The IR ozone values are reported at locations that complement the UV nadir total ozone values (i.e., for SZA greater than 80 degrees).

Figure 1.1-1 maps the flow of the OMPS data from the sensors through the RDR, SDR, and EDR algorithms. For the SDR algorithm, the figure identifies the required inputs as the external EDRs, the climatological databases, and the calibration data. For the EDR algorithms this figure also identifies the connection between the algorithms. The IR total column ozone product is used to expand the geographical coverage of the nadir Total Column sensor.

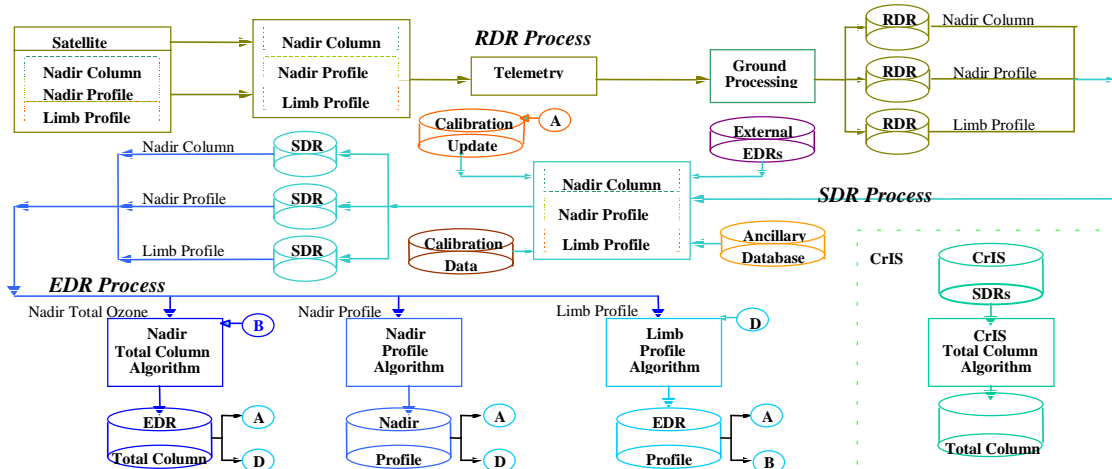


Figure 1.1-1. Overview of the data flow from the sensors through the RDR algorithms to the RDRs and then through the SDR algorithm to the SDRs. The final step takes the SDRs through the four EDR algorithms to the ozone EDRs. The letters indicate use of intermediate and final data products in the production of the SDRs and EDRs.

1.2 Objectives

This Algorithm Theoretical Basis Document (ATBD) describes the algorithm used to retrieve the OMPS Profile Ozone product. This product consists of the values of ozone in 3 km layers from the tropopause (or cloud tops) to 60 km and observed for all solar zenith angle viewing conditions less than or equal to 80 degrees.

This document identifies the sources of input data that are required by the algorithm; provides the physical theory and mathematical background underlying the use of this information; describes practical considerations affecting the detailed algorithm development; lists any assumptions employed in the algorithm retrieval process, describes the EDR products and additional algorithm by-products; details expected sensor and algorithm errors (accuracy and precision); discusses the use of calibration datasets; and outlines our test and validation approaches.

1.3 Scope

An individual document has been developed for each of the four OMPS algorithms. These are summarized with their output products in **Table 1.3-1**.

Table 1.3-1. The OMPS algorithms take advantage of internally generated products while minimizing dependence on external data.

Product	Nadir Total Column	UV/VIS Limb	Nadir Profile	IR Total Column	Algorithm
Nadir Total Column O ₃	E				
UV/VIS Limb O ₃ Profile		E			
Nadir O ₃ Profile					
Cloud Fraction (Reflectivity)					
Visible Surface Reflectivity					
Aerosol Index					
Volcanic SO ₂					
Aerosol Profile					
Neutral Number Density Profile					
Temperature Profile					
Cloud Height					
Surface Reflectivity/Type					
<div> <div>E</div> EDR Product <div></div> Algorithm Input Generated Internally by OMPS <div></div> Additional Product Produced by OMPS (P₃) <div></div> Algorithm Input Supplied by External EDR (preferred) or Climatological Database </div>					

A7785_161

1.4 Overview

The UV/VIS Limb Profile Ozone Algorithm is adapted from the Herman Limb Scattering Algorithm. (Herman et al, 1995a, and Herman et al, 1995b). The algorithm was employed with the Shuttle Ozone Limb Scatter Experiment (SOLSE) and the Limb Ozone Retrieval Experiment (LORE). The algorithm is based on the comparison of measured normalized scene radiance to calculated normalized scene radiance (using a Radiative Transfer Model) for the specific measurement geometry, viewing conditions and surface conditions. The algorithm takes the IFOV information from the SDR, determines the viewing geometry and characterizes the scene from either external EDR information or climatological data. It constructs the normalized scene radiance as the ratio of each of the measured radiance to the radiance at a reference altitude. From the Radiative Transfer Model, the normalized scene radiance is calculated for the given viewing conditions. After correcting for the radiance contributions from neutral density scattering and from aerosol scattering, the measured and modeled scene radiance is compared to the measured values and an ozone estimate determined. After data quality flags are set the EDR output file is constructed.

1.5 Data Products

The EDR produced by the limb profile ozone algorithm is the vertical distribution of ozone covering altitudes from the tropopause to 60 km in 3 km vertical cells.



1.6 Applicable Documents

1.6.1 Controlling Documents

1. OMPS System Specification – Document Number 542798
2. OMPS Algorithm Development Specification – Document Number 542808

1.6.2 OMPS Reference Documents

1. OMPS Algorithm Theoretical Basis Document: Nadir Total Column Ozone Algorithm—Document Number IN0092A-106.
2. OMPS Algorithm Theoretical Basis Document: UV/VIS Limb Profile Ozone Algorithm—Document Number IN0092A-107.
3. OMPS Algorithm Theoretical Basis Document: Nadir Profile Ozone Algorithm—Document Number IN0092A-108.
4. OMPS Algorithm Theoretical Basis Document: IR Total Column Ozone Algorithm—Document Number IN0092A-109.

1.7 Revision History

The original version of this document was dated March 1, 1999.

1.8 Contributing Authors

Contributors to each of the four OMPS ATBDs include:

Lead: Nadir Total Column Ozone Algorithm	Colin Seftor	Raytheon
Lead: Nadir Profile Ozone Algorithm	Charles Wellemeyer	Raytheon
Lead: UV/VIS Limb Profile Ozone Algorithm	Jack Larsen	Raytheon
Lead: IR Total Column Ozone Algorithm	Hilary Snell, John Pickle	AER

Other contributors include:

Susan Beresford	AER, Inc.
Brent Canova	Ball Aerospace & Technologies Corp.
Kelly Chance	Harvard-Smithsonian
David Flittner	University of Arizona
Jennifer Hegarty	AER, Inc.
Benjamin Herman	University of Arizona
Glen Jaross	Raytheon
James Leitch	Ball Aerospace & Technologies Corp.
Jean-Luc Moncet	AER, Inc.
John Qu	Raytheon
Hélène Rieu	AER, Inc.
Juan Rodriguez	Ball Aerospace & Technologies Corp.
James Russell	Hampton University
Thomas Swissler	Consultant

2. Scientific Basis

2.1 Physical Description

To interpret the radiance measurements made by the OMPS limb profile ozone sensor requires an understanding of how the Earth's atmosphere scatters ultraviolet, visible, and near infrared radiation as a function of solar zenith angle. Incoming solar radiation undergoes absorption and scattering in the atmosphere by atmospheric constituents such as ozone and aerosols, and Rayleigh scattering. Radiation that reaches the ground is scattered by surfaces of widely varying reflectivity.

To achieve vertical coverage from the tropopause to 60 km, the OMPS limb sensor ozone channels were selected to observe a range of strongly absorbing to weakly absorbing features in the Hartley-Huggins and Chappuis ozone bands. At all of these wavelengths absorption by other atmospheric components is normally negligible compared to that of ozone. The ozone absorption coefficients differ from band to band, increasing as the wavelength decreases. Consequently, as wavelength decreases, significant absorption occurs at progressively higher levels in the atmosphere. Although in principle the scattered intensity at a given wavelength depends upon the entire ozone profile from the top of the atmosphere to the surface, in practice it is sensitive only to the profile over a restricted range in altitudes. Consequently, measurements of scattered radiation at shorter wavelengths yield information on the ozone profile at higher levels of the atmosphere than measurements at longer wavelengths.

At wavelengths shorter than about 295 nm, solar radiation is almost completely absorbed above the ozone density peak at 20-25 km. Because the intensity of the scattered radiation at these wavelengths is determined solely by the ozone profile above the peak, it can be used to derive that part of the ozone profile. At these wavelengths, tropospheric features, including clouds, aerosols and terrain height, do not affect the radiation scattering and can be ignored. The computation of atmospheric scattering for the shorter wavelengths is easier than it is for the longer wavelengths.

Between 295 nm and 310 nm, scattering takes place over a wide range of altitudes. The scattered intensity depends upon the height of the ozone peak as well as the ozone amount below the peak. Radiation at these wavelengths thus provides profile information near and below the ozone peak. Tropospheric features have only a small effect on the radiances at these wavelengths.

For wavelengths longer than 310 nm, the scattered radiance consists primarily of solar radiation that penetrates the stratosphere and is reflected back by the dense tropospheric air, clouds, aerosols and the Earth's surface; scattering takes place predominantly in the troposphere. The amount of ozone below the scattering layer is small. Because most of the ozone is in the stratosphere, the principal effect of the total atmospheric ozone is to attenuate both the solar flux going to the troposphere and the component reflected back to the sensor. This separation of the absorbers in the stratosphere (i.e., ozone) and the "reflector" in the troposphere (i.e., atmospheric scattering, clouds and Earth surface) causes scattered radiances longer than 310 nm to depend weakly on the vertical distribution of ozone in the stratosphere. Clouds, surface reflectances, aerosols and terrain height strongly influence the diffuse radiation field in the troposphere and lower stratosphere.

Derivation of atmospheric ozone content from measurements of the scattered radiance requires a treatment of scattering from the Earth's surface, by clouds, and by other aerosols. These scattering processes are not isotropic; the scattered light depends upon both incident angle and viewing angle. In

principle, then, the reflectivity is a function of solar zenith angle. Studies by Dave (1978) and by Fraser and Ahmad (1978) show that, in practice, the contribution of clouds and aerosols to the scattered intensity can be treated by assuming that radiation is reflected from a particular pressure level called the “scene pressure” with an effective “scene reflectivity” R . Thus, in addition to deriving a reflectivity for the albedo calculations, a pressure level for the effective reflecting surface must be defined for each instantaneous field of view (IFOV).

2.2 Sensor Description

The NPOESS satellite will operate in a near circular, sun-synchronous orbit. The nominal orbit for the satellite is 833 km altitude, 98.7 degree inclination. The orbit will be a “precise” orbit (i.e., altitude maintained to ± 17 km, ± 0.05 degrees inclination and nodal crossing times maintained to 10 minutes throughout the mission lifetime) to minimize orbital drift (precession). The NPOESS platform will be capable of flying at any equatorial node crossing time. However, the nominal configuration will be a nodal crossing time of 1330.

The OMPS limb sensor is a triple-slit prism spectrometer that senses atmospheric radiance and solar irradiance over the wavelength range of 290 to 1000 nm. The 3 slits provide three adjacent IFOVs; one centered above the ground track (to compare with nadir profile) and one on either side. The slit separation is 4.25 deg on each side, which is 250 km in object space. A single 16 mm aperture telescope feeds the 3 slits. The telescope also contains a depolarizer to keep the linear polarization sensitivity below 1% and a short wavelength blocking filter to prevent overlap of adjacent spectra on the focal plane.

The vertical FOV of each slit is 2.5° , covering the 0-65 km altitude range and allowing for alignment boresight offsets, spacecraft pointing variation, and limb motion due to the varying earth radius and orbit radius variation. Ref.: ICSR E8121803 (Vertical registration of sensor FOV).

The sensor uses a single CCD focal plane to measure the spectra from the 3 slits. Vertical sample size is 1.0 km at the tangent distance of 3365 km. The horizontal sample size is 2.5 km.

The spectral measurements for all altitudes are made simultaneously to eliminate any variation due to non-coincident observations and for accurate normalization to reference altitude. Radiance measured simultaneously at all wavelengths gives accurate wavelength ratios of absorbing to non-absorbing radiance.

Sixteen spectral channels are produced for the ozone retrieval algorithm. The center wavelengths of the channels are 290, 293, 296, 299, 302, 310, 320, 350, 353, 400, 500, 525, 575, 602, 675, and 1000 nm. The spectral bandpass (for 2 adjacent summed pixels) ranges from 1.5 nm FWHM at 290 nm to 40 nm at 1000 nm due to the varying dispersion of the prism spectrometer. The wavelengths and number of pixels contained in each channel is programmable from the ground for flexibility.

The integration time per frame is variable depending on the scene radiance. The nominal integration time is 1.26 s. The reporting period is 38 s, corresponding to 250-km horizontal cell size along track. All available frames (about 30) are co-added per reporting period to maximize SNR.

To handle the large dynamic range of the limb radiance and solar irradiance, three images per slit are produced on the focal plane with each image differing from the next by a factor of 10 in radiance. The full signal image is used for the low radiance high altitude measurements, while the reduced intensity

images are used for the bright lower limb. Regions of the image having valid data in several images are used to get an accurate in-flight measure of the gain ratio between the images.

On-orbit calibration is provided by solar irradiance measurements with a transmissive quartz plate diffuser at the entrance aperture. Working and reference diffusers are used to monitor diffuser degradation. The ground calibration is based on combined FEL irradiance and integrating-sphere radiance (Heath et al., 1993).

2.3 Forward Model

In terms of the standard polarization parameters the radiation field may be represented as,

$$I = (I_l, I_r, U, V) = (I_1, I_2, I_3, I_4)$$

In this representation unpolarized plane parallel solar radiation at the top of the atmosphere with unit radiance is expressed as,

$$F_0 = (0.5, 0.5, 0, 0)$$

The formal solution to the radiative transfer equation in integral form using the nomenclature of Herman et al., 1995, may be written for the p th polarization component as,

$$I_p(s, \theta, \phi) = I_p(s_0, \theta, \phi) e^{-\tau(s, s_0)} + \int_{s_0}^s J_p(s', \theta, \phi) e^{-\tau(s, s')} \kappa \rho ds'$$

where θ is the polar view angle, ϕ the azimuthal view angle, s is distance along the line of sight, and $J_p(s, \theta, \phi)$ is the source function. The source function accounts for single and multiple scattering, and emission. Emission contributions to the source function at atmospheric temperatures in the ultraviolet, visible, and near infrared spectral regions used by OMPS are much smaller than solar scattering contributions and may be neglected without loss of accuracy. The first term on the right hand side represents incident radiation that is attenuated by atmospheric scattering and absorption processes when traversing from s to s' . For the OMPS limb observations, which view radiation from the earth's limb against the background of space, this term is zero.

The optical depth along the line of sight, $\tau(s, s')$, is given by,

$$\tau(s, s') = \int_{s'}^s \kappa \rho ds'$$

from point s' to s . κ is the mass extinction coefficient and ρ is the mass density. The source function may be split into two components based on whether the observed radiation is the result of a single scattering event or has been multiply scattered.

$$J_p(s', \theta, \phi) = J_p^{ss}(s', \theta, \phi) + J_p^{ms}(s', \theta, \phi)$$

For a conservative scattering atmosphere the single scattering source function, $J_p^{ss}(s', \theta, \phi)$, is defined by,

$$J_p^{ss}(s', \theta, \phi) = P_{pq}(s', \theta, \phi, \theta_0, \phi_0) F_q(s', \theta_0, \phi_0)$$

and the multiple scattered source function, $J_p^{ms}(s', \theta, \phi)$, by,

$$J_p^{ms}(s', \theta, \phi) = \int_0^{2\pi} \int_0^\pi P_{pq}(s', \theta, \phi, \theta', \phi') I_q(s', \theta', \phi') \sin \theta' d\theta' d\phi'$$

$F_q(s', \theta_0, \phi_0)$ is the q th polarization parameter of the attenuated incident solar radiation at position s' in the direction θ_0, ϕ_0 while the scattering phase matrix, $P_{pq}(s', \theta, \phi, \theta', \phi')$, describes the scattering of radiation from the θ', ϕ' incident direction to the θ, ϕ scattered direction. $I_q(s', \theta', \phi')$ represents the q th component of the diffuse radiation field. Substituting the single and multiple scattering source functions into the formal solution leads to,

$$I_p(s, \theta, \phi) = \int_{s_0}^s J_p^{ss}(s', \theta, \phi) e^{-\tau(s, s')} \kappa \rho ds' + \int_{s_0}^s J_p^{ms}(s', \theta, \phi) e^{-\tau(s, s')} \kappa \rho ds'$$

and

$$I_p(s, \theta, \phi) = I_p^{ss}(s, \theta, \phi) + I_p^{ms}(s, \theta, \phi)$$

where

$$I_p^{ss}(s, \theta, \phi) = \int_{s_0}^s P_{pq}(s', \theta, \phi, \theta_0, \phi_0) F_q(s', \theta_0, \phi_0) e^{-\tau(s, s')} \kappa \rho ds'$$

and

$$I_p^{ms}(s, \theta, \phi) = \int_{s_0}^s \int_0^{2\pi} \int_0^\pi P_{pq}(s', \theta, \phi, \theta', \phi') I_q(s', \theta', \phi') \sin \theta' d\theta' d\phi' e^{-\tau(s, s')} \kappa \rho ds'$$

For limb viewing geometry the integration along the line of sight begins at the top of the atmosphere (s_0), continues down to altitude of closest approach by the line of sight to the earth's surface, also known as the tangent height (z_{th}), and then upwards to the top of the atmosphere (s). Given that a one to one correspondence exists between a particular line of sight and the tangent height, it is convenient to express the limb radiance in terms of the tangent height as,

$$I_p(z_{th}, \theta, \phi) = I_p^{ss}(z_{th}, \theta, \phi) + I_p^{ms}(z_{th}, \theta, \phi)$$

The sensor responds to the sum of the first two polarization components,

$$I(z_{th}, \theta, \phi) = I_1(z_{th}, \theta, \phi) + I_2(z_{th}, \theta, \phi)$$

and analogous equations may be written for the single and multiple scattered components.

Separating the limb radiances into single and multiple scattered components offers modeling and computational advantages. The single scattering component depends only on the absorption and scattering characteristics of the atmospheric constituents while the multiple scattering component also includes surface effects in the form of reflections from ground surfaces and cloud top. Single scattering calculations typically require much less computational time than the multiple scattering component. To reduce overall computation time, single scattering calculations are coupled with pre-calculated multiple scattering tables. Depending on the wavelength, both components can vary by more than three orders of magnitude over tangent altitude but the ratio of multiple scattered to single scattered varies by much less. Section 2.3.2 describes how this ratio is developed and applied.

2.3.1 Radiative Transfer Code

Accurate limb radiances require full treatment of atmospheric sphericity. The fully spherical polarized code of Herman et al., 1995 was adopted for the OMPS limb profiler. The code includes Rayleigh and aerosol scattering and absorption by ozone and may be easily expanded to include scattering and absorption by other constituents. The Herman code uses the Gauss-Seidel method to calculate the diffuse radiation field on the zenith. Integration along the line of sight uses this diffuse solution to construct I^{ss} and I^{ms} .

2.3.2 Radiative Transfer Tables

The approach taken in developing the limb multiple scattering tables mirrors that of the nadir total column described in section 2.3.1 of that document (Nadir Total Column Ozone ATBD, Doc. No. IN0092A-106). Consider an atmosphere bounded below by a Lambertian reflecting surface of reflectivity R . The scattered radiance emerging from the top of the atmosphere as seen by the sensor, I_m , is the sum of purely atmospheric scatter I_a , and reflection of the incident radiation from the reflecting surface I_s ,

$$I_m(z_{th}, \lambda, \theta_0, \Omega, P_0, R) = I_a(z_{th}, \lambda, \theta_0, \phi, \Omega, P_0) + I_s(z_{th}, \lambda, \theta_0, \Omega, P_0, R),$$

where

z_{th}	=	altitude of tangent height
λ	=	wavelength
θ_0	=	solar zenith angle
ϕ	=	relative azimuth angle
Ω	=	ozone profile
P_0	=	pressure at the reflecting surface
R	=	effective reflectivity at the reflecting surface

Note that the I_a term includes single scattering and multiple scattering that occurs without surface interaction.

The intensity due to atmospheric scattering can be expressed as a harmonic series in azimuth as:

$$I_a(z_{th}, \lambda, \theta_0, \Omega, P, R) = \sum_{m=0}^N I_m(z_{th}, \lambda, \theta_0, \Omega, P, R) \cos(m\phi)$$

N=2 for Rayleigh scattering, yielding two azimuthally dependent terms and one azimuthally independent term:

$$I_a = I_0 + I_1 \cos \phi + I_2 \cos 2\phi$$

where I_0 , I_1 , and I_2 are expansion coefficients.

The surface reflection term, I_s , can be expressed as:

$$I_s(z_{th}, \lambda, \theta_0, \Omega, P_0) = \frac{RT(z_{th}, \lambda, \theta_0, \Omega, P_0)}{1 - RS_b(\lambda, \Omega, P_0)}$$

$$T(z_{th}, \lambda, \theta_0, \Omega, P_0) = I_d(z_{th}, \lambda, \theta_0, \Omega, P_0) f(z_{th}, \lambda, \Omega, P_0)$$

where

- S_b = fraction of radiation reflected from surface that atmosphere reflects back to surface
- I_d = total amount of direct and diffuse radiation reaching surface at P_0
- f = fraction of radiation reflected toward satellite in direction θ that reaches the satellite,

The denominator accounts for multiple reflections between the ground and atmosphere, where S_b is the fraction of the reflected radiation scattered back to the surface by the atmosphere.

The total limb radiance observed by the sensor can therefore be written as (dropping subscripts for convenience):

$$I^t = I_0 + I_1 \cos \phi + I_2 \cos 2\phi + \frac{RT}{1 - RS_b}.$$

The same azimuthal expansion can be applied to the single scattered limb radiance,

$$I^{ss} = I_0^{ss} + I_1^{ss} \cos \phi + I_2^{ss} \cos 2\phi$$

The ratio of multiple to single scattered limb radiance is,

$$R^{ms/ss} = (I^t - I^{ss}) / I^{ss}$$

In practical application, one calculates I^t and I^{ss} over a wide variety of atmospheric models and then stores either I^t and I^{ss} or the appropriate expansion coefficients in tabular form. To construct total limb radiances, $I^{t,p}$, for a particular case, single scattering radiances $I^{ss,p}$ are first calculated for that case.

Then, the tabular information is used in an interpolation process to calculate $R^{ms/ss}$ which defines the multiple scattering contribution. The total limb radiance is given by

$$I^{t,p} = I^{ss,p} + R^{ms/ss} I^{ss,p} = (1 + R^{ms/ss}) I^{ss,p}$$

The accuracy of the multiple scattering contributions depends on the tabular grid spacing and the tabular values must span the full range of conditions likely to be encountered in the atmosphere.

Table 2.3-1 lists the independent variables that largely determine limb radiances and their range of values needed for the OMPS limb sensor.

Table 2.3-1 Table node points

Quantity	Number	Values
Channel Wavelength	16	290, 293, 296, 299, 302, 310, 320, 347, 353, 400, 500, 525, 575, 602, 675, 1000 nm
Tangent Altitudes	81	0.5-80.5 km
Solar Zenith Angle	6	0, 20, 40, 60, 80, 85°
Azimuthal Angle	6	0, 30, 60, 90, 120, 150, 180°
Pressure	4	1.0, 0.7, 0.4, 0.2 atm
Aerosol Profiles	4	None, Background, Aged, Fresh Volcanic
Ozone Profiles	26	6 low, 10 mid and high latitude

Not shown in Table 2.3-1 are the range of surface reflectances used for each wavelength. At wavelengths less than or equal to 300 nm limb radiances are calculated only for surface reflectances of zero. Between 300 and 400 nm limb radiances are calculated at 0.0, 0.6, and 1.0. Above wavelengths of 400 nm reflectances of 0.0, 0.4, and 1.0 are used. At shorter wavelengths the limb radiances are insensitive to surface reflectance and only one value is necessary, zero was arbitrarily chosen. At the other wavelengths the middle reflectance value was adjusted to minimize the fitting error in I_s .

To reduce computational time, I^t and I^{ss} are calculated with slit averaged solar fluxes, ozone cross-sections, and Rayleigh scattering cross-sections. The averaging process is described in section 2.3.2.2.

The 6 low latitude profiles range from 225 to 475 Dobson Units (DU) in steps of 50 DU. The 10 mid and 10 high latitude profiles range from 125 to 575 DU in steps of 50 DU. These standard ozone and temperature profiles were determined from an Empirical Orthogonal Function (EOF) analysis of the entire SAGE II data set as described in section 2.3.2.1.

As described above, the multiple scattering is based on a standard set of ozone and temperature profiles. To correct for deviations between the actual temperature profiles and the standard profiles, the OMPS limb algorithm adjusts the tabulated $R^{ms/ss}$ with the help of a second multiple scattering table calculated with the node points listed in Table 2.3-1 with perturbed temperature profiles.

2.3.2.1 Standard ozone and temperature profile determination

The OMPS limb algorithm's table is based on a set of climatological ozone profiles that account for the dependence of the measured radiances on the total amount of ozone and its vertical distribution [Klenk et al., 1982]. To develop this set of standard profiles, empirical orthogonal functions (EOF) were derived for an external data set comprising SAGE II profiles over the period from launch in October, 1984 through June, 1991 (when the eruption of Mt. Pinatubo began to impact the SAGE II ozone retrieval). This problem is bounded by using only the first two EOF to define a two dimensional space that explains most of the variability in the ozone profile. To provide statistically consistent lower layers for SAGE II profiles, a set of balloonsonde profiles in the period from November 1978 through 1987 for 20 ground sites distributed about the globe were used in conjunction with the SAGE II profiles. The derived climatology spans the ensemble of possible profiles. For details of the analysis, see *Wellemeyer, et al., 1997*. The standard OMPS profiles are defined in Umkehr layers (**Table 2.3-2**), so the SAGE II profiles are converted to pressure coordinates using the NMC temperature profiles provided with the archived data and integrated into Umkehr layers. The resulting standard ozone and temperature profiles are given in **Tables 2.3-3 and 2.3-4** below. For application to the OMPS limb multiple scattering table generation process, the ozone and temperature profiles were reconstructed on a 1 km grid from the surface to 81 km with a spline interpolation process. Transforming from the coarse Umkehr layers to 1 km layers results in profiles smoother than the original SAGE II profiles.

Table 2.3-2. Umkehr Layers Used for Ozone Profiles

Umkehr Layer No	Layer Pressure (mb)	Pressure at Altitude of Midpoint (mb)	Layer Midpoint (km)
12	0.000 -0.247	-	-
11	0.247 - 0.495	.350	56.5
10	0.495 - 0.990	.700	51.0
9	0.990 - 1.980	1.40	45.5
8	1.980 - 3.960	2.80	40.2
7	3.960 - 7.920	5.60	35.2
6	7.920 - 15.80	11.2	30.4
5	15.80 - 31.70	22.4	25.8
4	31.70 - 63.30	44.8	21.3
3	63.30 -127.0	89.6	17.0
2	127.0 - 253.0	179.0	12.5
0 & 1	253.0 - 1013	507.0	5.5



Table 2.3-3. OMPS Standard Ozone Profiles

Prof	Umkehr Layer Number										
	0	1	2	3	4	5	6	7	8	9	> 9
225L	15.0	9.0	5.0	7.0	25.0	62.2	57.0	29.4	10.9	3.2	1.3
275L	15.0	9.0	6.0	12.0	52.0	79.2	57.0	29.4	10.9	3.2	1.3
325L	15.0	9.0	10.0	31.0	71.0	87.2	57.0	29.4	10.9	3.2	1.3
375L	15.0	9.0	21.0	53.0	88.0	87.2	57.0	29.4	10.9	3.2	1.3
425L	15.0	9.0	37.0	81.0	94.0	87.2	57.0	29.4	10.9	3.2	1.3
475L	15.0	9.0	54.0	108.0	100.0	87.2	57.0	29.4	10.9	3.2	1.3
125M	6.0	5.0	4.0	6.0	8.0	31.8	28.0	20.0	11.1	3.7	1.4
175M	8.0	7.0	8.0	12.0	26.0	41.9	33.6	22.3	11.1	3.7	1.4
225M	10.0	9.0	12.0	18.0	44.0	52.1	39.2	24.5	11.1	3.7	1.4
275M	16.0	12.0	15.0	29.0	58.0	63.7	40.6	24.5	11.1	3.7	1.4
325M	16.0	14.0	26.0	45.0	74.7	66.9	41.7	24.5	11.1	3.7	1.4
375M	16.0	16.0	39.0	64.0	85.7	71.1	42.5	24.5	11.1	3.7	1.4
425M	16.0	18.0	54.0	84.0	97.7	71.7	42.9	24.5	11.1	3.7	1.4
475M	16.0	22.0	72.0	107.7	101.0	72.6	43.0	24.5	11.1	3.7	1.4
525M	16.0	26.0	91.0	127.7	108.0	72.6	43.0	24.5	11.1	3.7	1.4
575M	16.0	30.0	110.0	147.7	115.0	72.6	43.0	24.5	11.1	3.7	1.4
125H	9.5	7.0	18.3	7.6	8.2	28.6	22.0	12.4	7.7	2.5	1.2
175H	9.5	8.0	22.8	22.0	26.9	32.3	26.8	15.0	8.0	2.5	1.2
225H	10.0	9.0	27.6	45.7	41.0	35.0	28.8	15.4	8.3	2.9	1.3
275H	14.0	12.0	34.0	66.9	54.2	36.0	28.8	15.4	8.9	3.4	1.4
325H	14.0	15.0	46.8	82.6	65.2	41.7	28.8	17.2	8.9	3.4	1.4
375H	14.0	20.0	61.2	93.8	75.2	45.9	32.5	18.7	8.9	3.4	1.4
425H	14.0	25.0	76.2	104.9	84.2	51.4	35.6	20.0	8.9	3.4	1.4
475H	14.0	32.0	91.0	117.1	93.0	55.8	37.5	20.9	8.9	3.4	1.4
525H	14.0	41.0	107.1	128.1	101.0	60.2	38.2	21.7	8.9	3.4	1.4
575H	14.0	49.0	123.2	142.2	111.0	60.6	38.8	22.5	8.9	3.4	1.4

Table 2.3-4. OMPS Standard Temperature Profiles

Prof	Umkehr Layer Number										
	0	1	2	3	4	5	6	7	8	9	> 9
225L	283.0	251.0	215.6	200.7	210.7	221.6	231.1	245.3	258.7	267.4	265.4
275L	283.0	251.0	215.9	203.5	211.9	222.5	231.1	245.3	258.7	267.4	265.4
325L	283.0	251.0	216.5	207.0	213.6	223.0	231.1	245.3	258.7	267.4	265.4
375L	283.0	251.0	216.0	210.0	216.0	224.0	231.1	245.3	258.7	267.4	265.4
425L	283.0	251.0	216.0	213.0	217.0	224.5	231.1	245.3	258.7	267.4	265.4
475L	283.0	251.0	216.0	216.0	219.0	225.0	231.1	245.3	258.7	267.4	265.4
125M	237.0	218.0	196.0	191.0	193.0	210.0	227.6	239.4	253.6	263.9	262.6
175M	260.0	228.0	201.7	198.0	202.1	214.3	227.6	239.4	253.6	263.9	262.6
225M	273.0	239.0	213.3	207.5	211.7	219.1	227.6	239.4	253.6	263.9	262.6
275M	273.0	239.0	217.1	212.2	214.9	220.4	227.6	239.4	253.6	263.9	262.6
325M	273.0	239.0	219.1	216.6	217.0	220.8	227.6	239.4	253.6	263.9	262.6
375M	273.0	239.0	220.2	219.0	219.0	221.9	227.6	239.4	253.6	263.9	262.6
425M	273.0	239.0	220.9	220.7	221.0	223.7	227.6	239.4	253.6	263.9	262.6
475M	273.0	239.0	221.5	222.5	222.7	224.4	227.6	239.4	253.6	263.9	262.6
525M	273.0	239.0	222.3	224.8	225.5	225.8	227.6	239.4	253.6	263.9	262.6
575M	273.0	239.0	225.0	227.0	227.0	227.0	227.6	239.4	253.5	263.9	262.6
125H	237.0	218.0	196.0	191.0	193.0	210.0	223.3	237.1	251.6	262.4	265.6
175H	260.0	228.0	201.7	198.0	202.1	214.3	223.3	237.1	251.6	262.4	265.6
225H	260.0	228.0	209.7	208.5	212.5	222.0	228.0	237.1	251.6	262.4	265.6
275H	260.0	228.0	222.6	223.4	223.8	226.5	231.6	237.1	251.6	262.4	265.6
325H	260.0	228.0	222.6	223.4	223.8	226.5	231.6	237.1	251.5	262.4	265.6
375H	260.0	228.0	222.6	223.4	223.8	226.5	231.6	237.1	251.5	262.4	265.6
425H	260.0	228.0	222.6	223.4	223.8	226.5	231.6	237.1	251.5	262.4	265.6
475H	260.0	228.0	222.6	223.4	223.8	226.5	231.6	237.1	251.5	262.4	265.6
525H	260.0	228.0	222.6	223.4	223.8	226.5	231.6	237.1	251.5	262.4	265.6
575H	260.0	228.0	222.6	223.4	223.8	226.5	231.6	237.1	251.5	262.4	265.6

2.3.2.2 Spectral slit averaging

The OMPS limb profile sensor measures radiances in the spectral range from 300 to 1000 nm. The limb profile algorithm uses 15 wavelengths from this range (details of the wavelength selection are given in Section 2.4.3).

The OMPS sensor cannot actually measure monochromatic radiance, $I(\lambda)$, because of its finite bandwidth. Mathematically, in the ideal case, the slit-average radiance can be written

$$\bar{I}(\lambda_0) = \frac{\int I(\lambda)S(\lambda)d\lambda}{\int S(\lambda)d\lambda},$$

where λ_0 is the central slit wavelength and $S(\lambda)$ is the response function (slit function). 10 to 20 calculations of $I(\lambda)$ would be required to accurately perform the wavelength integration. Therefore, as described in ICSR 8092902, the limb algorithm accounts for parameter spectral variation by calculating

channel averages. The averaged parameters are then used in a single limb radiance calculation. The generalized mathematical form of the averaging process is given by,

$$\bar{Y}(\lambda_0) = \frac{\int Y(\lambda) S(\lambda) d\lambda}{\int S(\lambda) d\lambda}$$

where Y represents the solar flux, ozone cross-section, or Rayleigh scattering cross-section.

2.4 Retrieval

2.4.1. Overview

The OMPS limb retrieval algorithm converts the observed radiances in 16 channels between 290 and 1000 nm to a vertical profile of ozone that satisfies the EDR requirements. Byproducts of this process are vertical profiles of aerosol extinction at 4 channels, a neutral number density profile, cloud fraction, and visible surface reflectances. The retrieval algorithm or EDR algorithm is the second step in a two step process. The first step, generation of SDRs with the SDR algorithm, is described in section 3.1. The SDR stores calibrated radiances and all auxilliary information needed for EDR processing except for the multiple scattering tables. The overall process of EDR formation is shown in **Figure 2.4-1**.

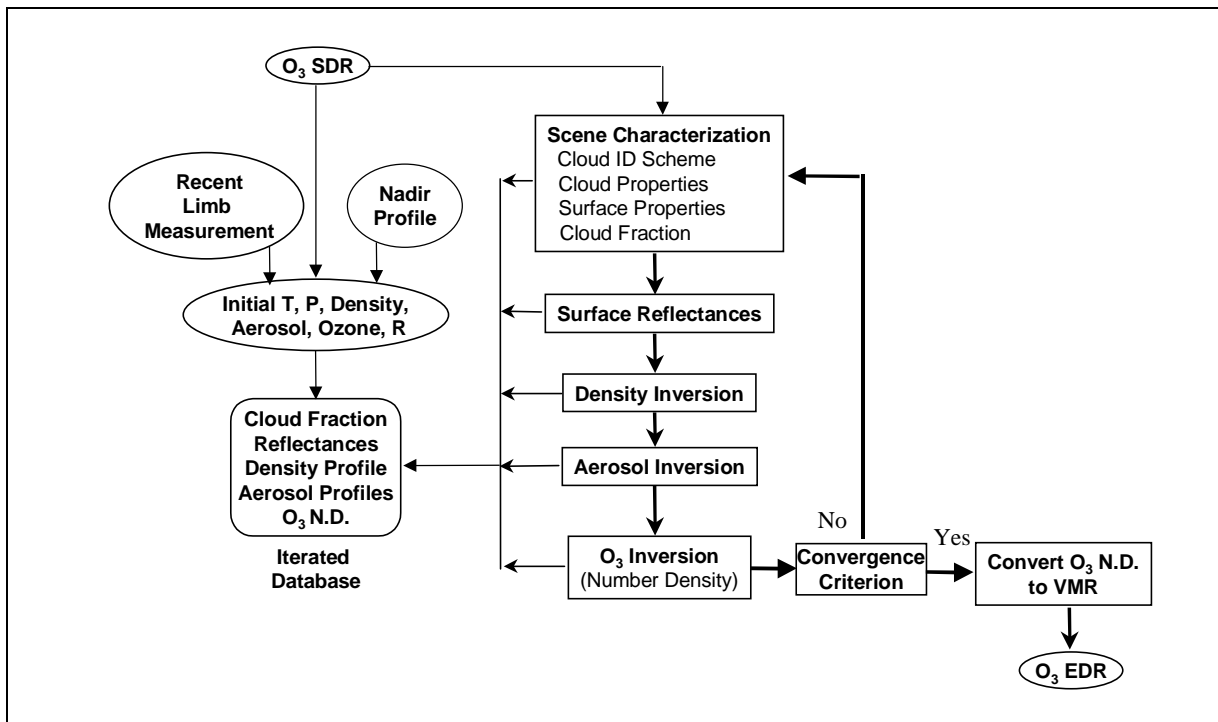


Figure 2.4-1. OMPS Limb EDR algorithm process flow

The series of procedures taken within the EDR algorithm follow a logical sequence dictated by the physics of the limb scattering process. As one might expect, this sequence also provides rapid convergence with minimum computation time. The series of procedures fall in three broad categories. The first category is concerned with defining the lower boundary conditions of the radiative transfer equation. The reflectance characteristics, in the form of surface reflectance and cloud top reflectance,

determine I_s at wavelengths longer than 320 nm. Since reflectance characteristics, through I_s , affect the convergence quality of all the profile inversions they must be determined first. The second category addresses all other quantities that must be specified before the ozone inversion is performed. This includes specifying the neutral number density, which defines the Rayleigh scattering component in each of the channels, and the aerosol profiles at the ozone channel wavelengths. After specification of the experimental variables affecting the limb radiances at ozone channel wavelengths is complete, ozone may be inverted, which is the last category.

2.4.2 Information Extraction

The OMPS limb algorithm approach to ozone inversion resembles that of SAGE II and SAGE III in many ways. Like these two experiments, OMPS must account for Rayleigh scattering and aerosols at the ozone wavelengths. In addition, OMPS must also take into consideration lower boundary reflectances to properly account for multiple scattering effects. Because the SAGE series of experiments measures limb extinction, it is possible to separate the extinction contributions by atmospheric constituent to yield distinct profiles of optical depth for each constituent that may be independently inverted. The complexity of the limb scattering process hinders a similar constituent separation for OMPS. Instead, each of the experimental variables is updated using the most recent updates of the other variables in the limb radiance calculations. The variable update sequence follows that shown in Figure 2.4-1. The order of these steps was specifically designed to provide rapid ozone convergence by ensuring the ozone inversion always uses the most recent experimental values. As shown in Figure 2.4-1, the iterative return loop runs from the convergence criterion step back up to the beginning of the scene characterization process. Each time the loop is traversed density, aerosol, and ozone undergo one iterative update. For these profile quantities, iterative adjustments are made based on the measured-calculated limb radiance difference and on the kernels, which describe the sensitivity of the limb radiance to profile quantity, using the optimal estimation methodology. However, visible surface reflectance and cloud fraction are iterated to solution, with the secant method, for each loop traversal. To date, ozone and neutral number density have been found to converge with three updates or loop traversals.

2.4.3 Channel Selection

The OMPS limb channel selection process began with analyzing the characteristics of the ozone kernels over wavelength. This analysis showed, that to achieve vertical coverage from 0 to 60 km, it would take a complement of channels distributed throughout the ultraviolet and visible spectral regions. Ozone cross-sections in the Hartley-Huggins bands provide excellent sensitivity above 25-28 km. A series of channels were chosen in this region to provide overlapping vertical coverage. For a given sensor signal to noise ratio, each channel has a range of altitudes where it is most sensitive to ozone. At the shortest OMPS wavelength, 290 nm, the cross-sections are greatest and provide coverage from 50-60 km. As the wavelength increases, the cross-section values decrease, and the range of usable altitudes moves downwards until, at 320 nm, the bottom altitude of the range is 25-28 km. Coverage below 28 km is provided by the much weaker ozone absorption from the Chappuis band in the visible spectral region. Because it is weak, the Chappuis band contributes very little to the ozone inversion above 30 km. Ozone vertical coverage as a function of wavelength is shown in **Figure 2.4-2**.

To accurately calculate Rayleigh scattering that is present in all of the channels requires a neutral number density profile. Spectral regions where Rayleigh scattering is the primary contributor to the limb radiances provide maximum sensitivity and at the same time, largely uncouple the neutral number density inversion from other atmospheric constituents. Rayleigh scattering cross-sections scale by the inverse of the wavelength to the fourth power. Below 800 nm Rayleigh scattering is greater than aerosol

scattering. Eliminating the spectral region covered by the Hartley-Huggins bands and Chappuis band leaves the 340 to 500 nm region. The NO₂ band located in this region leaves the 350 and 480 nm region as possible candidates for use in the neutral number density inversion. The 350 nm region was chosen for its heritage link to RSAS (Janz et al., 1996) and SOLSE/LORE (Flittner et al., 1998a,b) and because the Rayleigh component relative to aerosol is greater at 350 nm than at 480 nm.

Aerosol radiance wavelength dependence is characterized at ozone wavelengths by Angstrom power law interpolation from ozone “free” channels. Ozone “free” channels were identified in the wings of the Chappuis band at 500, 525, and 675 nm. Two additional channels, at 400 and 1000nm, were selected to improve knowledge of the aerosol wavelength variation. The 400 nm channel also improves accuracy of the aerosol extrapolation to 350 nm. While aerosol vertical coverage will vary with aerosol loading, if the aerosol loading is too low to invert, then it will also have little effect on the ozone channels.

Channels suitable for cloud fraction determination should be largely free of ozone and aerosol contributions. In addition, the surface reflectance must be known. Surface reflectances in the visible display considerably more seasonal and vegetative variations than in the UV. Surface reflectances in the UV have been characterized (Herman, J.R. and E.A. Celarier, 1997). These requirements limit the cloud fraction channel to the 350 nm wavelength region. Visible surface reflectances are simply calculated from the visible channels using radiances at tangent altitudes unaffected by ozone and aerosol (i.e. 35-55 km).

The altitude coverage of the neutral number density inversion, the aerosol channels, cloud fraction radiances, and visible surface reflectance radiances are also shown in Figure 2.4-2. **Table 2.4-1** summarizes the baseline channel complement and altitude range utilized in the solution process.

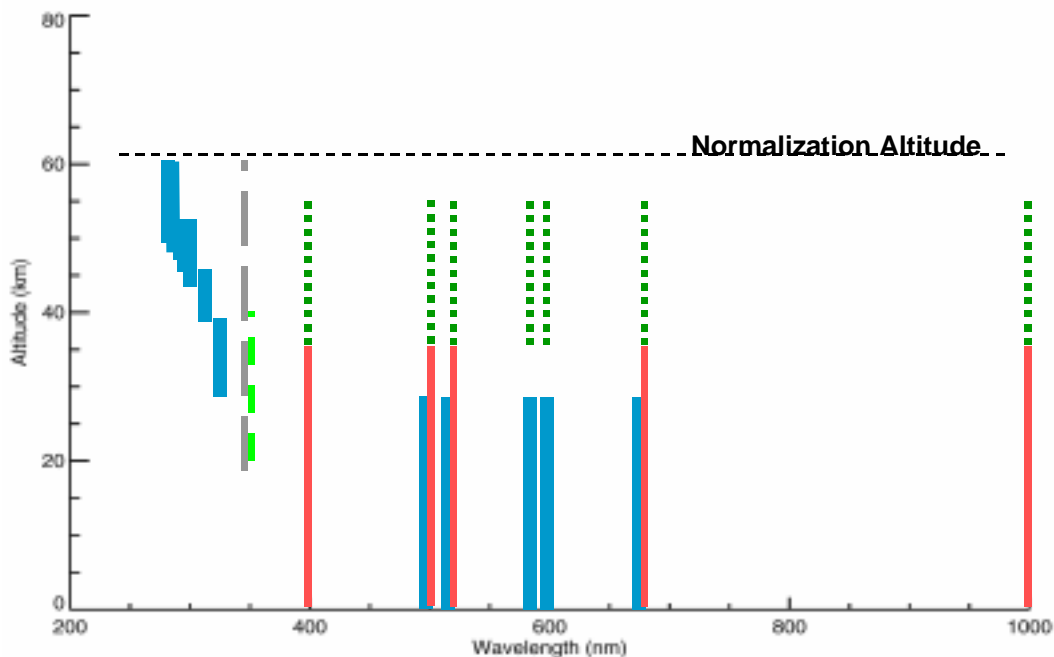


Figure 2.4-2. Solid thick lines indicate ozone channels, solid thin lines are aerosol channels, long dash line is neutral number density, short dash line is cloud fraction, and dotted lines are visible surface reflectances.

Table 2.4-1. Channel selection for limb sensor

Wavelength	Bandwidth	Application
290 nm	3 nm	Ozone 50-60 km
293 nm	3 nm	Ozone 50-60 km
296 nm	3.5 nm	Ozone 47-53 km
299 nm	3.5 nm	Ozone 47-53 km
302 nm	4 nm	Ozone 43-53 km
310 nm	4 nm	Ozone 38-45 km
320 nm	5 nm	Ozone 28-38 km
347 nm	6 nm	Neutral number density 18-60km, Cloud fraction 23-43 km
353 nm	6 nm	Neutral number density 18-60 km, Cloud fraction 23-43 km
400 nm	5 nm	Aerosol 0-35 km, Surface reflectivity 35-55 km
500 nm	9 nm	Aerosol 0-35 km, Surface reflectivity 35-55 km
525 nm	11 nm	Aerosol 0-35 km, Surface reflectivity 35-55 km
575 nm	14 nm	Ozone trop-28 km, Surface reflectivity 35-55 km
602 nm	16 nm	Ozone trop-28 km, Surface reflectivity 35-55 km
675 nm	21 nm	Aerosol 0-35 km, Surface reflectivity 35-55 km
1000nm	40 nm	Aerosol 0-35 km, Surface reflectivity 35-55 km, Cloud ID and cloud top altitude

2.4.4 Radiance Normalization

The effects of surface reflectance and cloud top reflectance appear in I_s at all altitudes to varying degrees. This influence can be greatly reduced by forming a [profile](#) ratio of limb radiances as follows,

$$N_m(z_{th}, \lambda, \theta_0, \Omega, P_0, R) = \ln[I_m(z_{th}, \lambda, \theta_0, \Omega, P_0, R) / I_m(z_{Norm}, \lambda, \theta_0, \Omega, P_0, R)]$$

Here, z_{NORM} identifies the normalization altitude and the logarithm of the ratio is taken to be consistent with previous presentations. [The normalized profile ratio, \$N_m\$, is formed by dividing the limb radiance value for each tangent height, \$z_{th}\$, by the limb radiance at \$z_{NORM}\$.](#) The normalization altitude should be selected such that the constituent being inverted makes a small contribution to the limb radiance at that altitude and yet should have an acceptable sensor signal to noise ratio (ICSR E8091501). Normalized radiances are used in the ozone, neutral number density, and aerosol inversions. [The normalization altitude for the ozone and neutral number density inversions is 61.5 km. A lower normalization altitude, around 45 km, is used in the aerosol inversion from the 400, 500, 525, 675, and 1000 nm channels. The normalization altitudes used in the three profile inversions will not change during the sensor operational lifetime unless significant changes in sensor characteristics or aerosol loading occur. \(High aerosol loading from a recent volcanic eruption may require a higher normalization altitude.\)](#)

The normalization process is not applied when solving for cloud fraction or visible surface reflectance. In this situation, maximum sensitivity to cloud fraction and surface reflectance is desired. Cloud fraction and neutral number density can be derived simultaneously from the 347 and 353 nm channels by using I_m for cloud fraction and N_m for density.

The power of the normalization technique is shown in **Figure 2.4-3.** Here, the percent change in limb radiance relative to the $R = 0.0$ limb radiance is compared with (dotted lines) and with out (solid lines) normalization, for surface reflectance values of 0.2 and 0.8. The percent change in limb radiance for both surface reflectance values is considerably smaller when normalization is applied.

The EDR algorithm uses the normalization technique to reduce errors in ozone caused by uncertainties in surface reflectance and cloud fraction as follows. First, as part of the scene generation process, iterative solutions for visible surface reflectances (described in Section 2.4.8.1) and cloud fraction (described in Section 2.4.8.5) are obtained from limb radiances that have not been normalized. Then, the visible surface reflectances and cloud fraction are used in the neutral number density, aerosol, and ozone profile inversions. The normalization technique used in these inversions reduces the effects of errors in visible surface reflectance and cloud fraction on the limb radiances. In a like manner, the normalization technique also substantially reduces ozone errors due to terrain height and cloud top altitude errors.

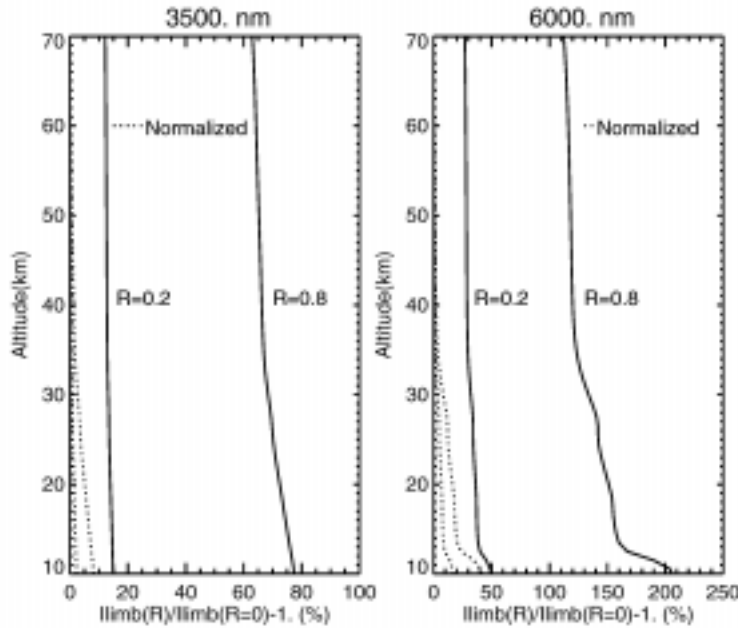


Figure 2.4-3.—A comparison of limb radiances with (dotted line) and without (solid line) normalization at 61.5 km calculated with the mid-latitude 325 DU model atmosphere.

2.4.5 Pair and Triplet Formulations

In addition to the radiance normalization, where all the radiances at a given wavelength are normalized by a radiance from a given altitude to reduce the influence of the surface, channel to channel ratios reduce errors due to channel or wavelength independent uncertainties. Pair and triplet combinations of the OMPS ozone channels are formed from the normalized signals. The pair formulation is simply,

$$Y_m(\lambda_i, \lambda_j, z) = N_m(\lambda_i, z) - N_m(\lambda_j, z)$$

while the triplet is stated as,

$$Y_m(\lambda_i, \lambda_j, \lambda_k, z) = N_m(\lambda_i, z) - (w_1 N_m(\lambda_j, z) + w_2 N_m(\lambda_k, z))$$

where i, j, k designate a particular channel. w are weights determined by the wavelength separation of the three channels. In the triplet formulation one can think of the weighted combination of channels j, k as a “virtual” channel that is paired with channel i . In the pair formulation channel i should exhibit

stronger absorption than channel j . In the triplet formulation, channels j, k are placed in the wings of the Chappuis band where ozone absorption is weak.

The UV channels are paired to the 353 nm channel and pairs and triplets are used in the visible spectral region. The pair and triplet formulations are very effective in reducing errors due to uncertainties in temperature, density, and wavelength independent radiance calibrations. The triplet formulation also provides a linear aerosol correction for channel i at altitudes where it is not possible to invert aerosol.

2.4.6 Optimal Estimation

The ozone, aerosol and neutral number density profile are inverted with the optimal estimation method of Rodgers (1976). If X represents the profile of either of these three constituents, the $n + 1$ iteration is given by,

$$X_{n+1} = X_0 + S_x K^T (K S_x K^T + S_e)^{-1} [Y_m - Y_n] - K(X_0 - X_n)$$

where S_x is the covariance matrix of X , S_e is the error covariance of Y_m , and Y_n is the calculated normalized and ratioed limb radiance. The kernel, K , or weighting function, is mathematically defined as the incremental change in the limb radiance signal at all tangent altitudes z due to an incremental change in X at altitude a .

$$K_n(\lambda_i, \lambda_j, z, a) = dy_n(\lambda_i, \lambda_j, z) / dx(a)$$

In the pair formulation the kernel is given as

$$K(\lambda_i, \lambda_j, z) = K(\lambda_i, z) - K(\lambda_j, z)$$

while in the triplet formulation it becomes,

$$K(\lambda_i, \lambda_j, \lambda_k, z) = K(\lambda_i, z) - (w_1 K(\lambda_j, z) + w_2 K(\lambda_k, z))$$

Since the kernels depend on X , they must be recalculated as the iterative process proceeds. At first glance, one would expect this to be prohibitive considering the amount of time multiple scattering calculations, needed for I or Y , require. However, kernels based on single scattering radiances have been shown (Herman et al., 1995) to provide equivalent convergence properties for which analytical forms can be developed for each of the constituents.

2.4.7 Initialization and Setup

Before the iterative process can begin the parameters in the iterated data base must be initialized. This includes cloud fraction, cloud top altitude/pressure, visible surface reflectances, neutral number density profile, aerosol profiles, and the ozone profile.

Highly accurate values are not needed since they are all replaced by the end of the first iteration but good estimates accelerate convergence.

Default values are used for all parameters, except ozone, when initializing the first measurement in an orbit's worth of data. After the first measurement the parameters are initialized with values from the

previous limb measurement. In both situations, the ozone profile from the nadir profiler serves to initialize the limb profiler. Should it not be available, a TOMS standard ozone profile closest in latitude will serve for the first measurement in an orbit with the previous limb measurement used thereafter.

The precision and accuracy of the reported ozone profile is not affected by the choice of initialization values for any of the parameters. The optimal estimation method used to invert ozone, aerosol, and density yields the same profile result regardless of initial starting profile. The same is true of the method used to solve for visible surface reflectance and cloud fraction.

Inverted aerosol is reported in terms of extinction/km. To convert between extinction/km and the parameters used in the radiative transfer program requires additional knowledge of the aerosol characteristics such as particle size distribution, particle composition, and refractive indices. Default values corresponding to background aerosols can be used for most observing conditions. However, if aerosols from a recent large volcanic eruption are present, the aerosol model will have to be changed to reflect that situation.

2.4.8 Scene Characterization

The OMPS algorithm accounts for the influence of complex lower boundary conditions on the radiative transfer calculations with a simple physical model. The limb radiance is assumed to be affected by reflectance from the terrain surface and from cloud tops. Thus, with knowledge of the terrain height and terrain reflectance a cloud free limb radiance profile is calculated. Similarly, with knowledge of cloud top height/pressure and reflectance, limb radiances can be computed for completely cloudy conditions. Limb radiances for mixed scenes are calculated from a weighted combination of each of the limb radiances using cloud fraction as the weighting factor.

The sequence of steps taken to fully characterize the scene is as follows. First, the terrain height is determined followed by the terrain type, clear ground or ground covered with snow/ice. This determines the UV reflectance. Next, the presence of cloud is determined along with cloud altitude/pressure. If cloud is present, the cloud fraction is calculated and used in the visible surface reflectance calculations.

2.4.8.1 Terrain Height and Reflectance

In the calculation of the terrain limb radiances, external terrain pressure information from CrIS is used to determine terrain height. If not available, a data set compiled from the TUG87 geophysical model [Weiser, 1987] is used. This data set contains a 1° latitude by 1.25° longitude grid of pressure values.

For surface reflectivities, external data from VIIRS is used to determine if snow or ice is on the ground. If the external EDRs are unavailable, a snow/ice database is used.

Terrain surface reflectances in the UV and visible are treated in following sections.

Ultraviolet Surface Reflectances

When the ground is determined to be free of snow/ice, the UV surface reflectivity is determined from a database of minimum UV surface reflectivity developed using the 15 year Nimbus-7/TOMS data set (Herman J.R. and E.A. Celarier, 1997) applicable from 340-380 nm. This data-set contains a 1° latitude by 1.25° longitude grid of minimum UV surface reflectivity for each month. This climatology is more than adequate for specifying surface reflectances in all channels below 380 nm (ICSR E8091401).

When the ground is snow/ice covered a surface reflectance of 0.8 is assumed.

Visible Surface Reflectances

After the terrain surface is known and the cloud height/pressure and cloud fraction have been determined it is possible to solve for the surface reflectances in the visible channels. To preserve maximum sensitivity to surface reflectance, the solution method uses limb radiances that have not been normalized or ratioed. Because the influence of R on I appears at all altitudes, there is some degree of freedom available for selecting the limb radiance altitude range employed in the solution. For all channels from 400 to 1000 nm we use the limb radiances from 35 to 55 km. Use of multiple limb radiances will reduce the effect of precision errors on the surface reflectance calculations. Ozone absorption in all channels is weak in this altitude range and aerosol scattering has little effect.

If $I_c(R, z)$ represents the calculated limb radiances for a mixed scene corresponding to measured radiances $I_m(z)$, we solve,

$$I_c(R, z) - I_m(z) = 0$$

The secant method provides a fast iterative solution to this equation for R . Recasting the previous equation leads to an expression for relative error,

$$RE(R) = 0$$

where

$$RE(R) = \frac{\sum_{z=35}^{z=55} [\ln(I_m(z)) - \ln(I_c(R, z))]}{\sum_{z=35}^{z=55} \ln(I_m(z))}$$

The secant method is iterated to solution. The secant iterations are uncoupled from the overall iterative updates associated with moving from the top to the bottom in Figure 2.4-1. The secant method requires RE calculated at two R before predicting a new solution. The first value of RE is calculated with an initial value of R, R_0 . This initial value is either the surface reflectance set at the initialization stage or the value calculated during the last update. The second value is calculated by adjusting R_0 as follows,

$$R_1 = R_0 \frac{\sum_{z=35}^{z=55} \ln(I_m(z))}{\sum_{z=35}^{z=55} \ln(I_c(R_0))}$$

A new value of R, R_2 , is predicted using the values of $RE(R_0)$ and $RE(R_1)$. The relative error is calculated for R_2 and then the surface reflectance with the largest relative error is dropped from the iterative process and the remaining two values are used in the next prediction. Typically, convergence is achieved within 8 iterations.

2.4.8.2 Node Point Selection

Before $R^{ms/ss}(z)$ can be calculated from the pre-stored limb radiances comprising the multiple scattering tables, values corresponding to node point quantities must be defined along with methods to

extract the limb radiance information. Of the node point quantities listed in Table 2.3-1, channel wavelength, tangent altitudes, solar zenith angle, and azimuthal angle are fixed during the iterative update process. For these quantities, direct interpolation or use of expansion coefficients provide a suitable method. Terrain pressure is also fixed but cloud top height/pressure may change during the updating process. Direct interpolation over pressure within the table is the most straightforward way to account for pressure variations.

Ozone and aerosol will definitely change during the updating process. For ozone we will take a slightly different approach to extracting the required information from the limb radiance tables.

The process begins with an estimate of total column ozone. The initial estimate of total column ozone may be taken from the nadir total column, the nadir profiler, climatology, or the limb profile from a recent measurement. Accurate values are not required since they do not affect the final limb ozone profile but accurate values will reduce the number of iterations. After the first iteration, total ozone will be calculated from the $n - 1$ limb profile iterate. The radiative transfer tables include ozone and temperature profiles for three broad latitude bands; low (15°), middle (45°) and high (75°). Total ozone and tangent point latitude are used in a two step interpolation scheme in the multiple scattering tables.

Each ozone profile has four aerosol profiles associated with it. Simple interpolation over the tabulated values suffices for aerosol.

2.4.8.4 Cloud Presence, Cloud Top Pressure/Altitude & Cloud Reflectance

The OMPS long wavelength channels are sensitive to the presence of clouds. They are particularly useful for detecting optically thin clouds that might go undetected by nadir sensors. On the other hand, nadir sensors may do a better job of detecting uniform cloud cover than the limb sensor.

We intend to use the VIIRS cloud fraction and cloud top altitude/pressure in conjunction with the 1000 nm channel to identify the presence of cloud and cloud top altitude/pressure. Limb radiances from the 1000 nm channel will be examined for rapid variations in radiance such as those observed in the SOLSE/LORE data. The highest altitude of rapid variation will be identified as the cloud top. To detect the presence of uniform cloud cover, which may not produce discrete features in the limb radiance profiles, we compare the measured limb radiances to a database of pre-calculated radiances. If the measured radiances exceed the pre-calculated radiances by a physically derived threshold, the cloud top altitude is set to the highest altitude at which this occurs. After the 1000 nm cloud analysis is complete, the 1000 nm analysis and the VIIRS cloud analysis are reconciled. If only one of the analyses reports the presence of cloud, the cloud top altitude/pressure associated with that identification is used. If both analyses report the presence of cloud, the highest cloud top altitude/pressure is used in the radiative transfer calculations.

In all situations where cloud is present, cloud fraction is calculated from the OMPS limb radiances as described in the following section. VIIRS cloud fraction is used only as a flag to indicate presence of cloud and is not used in the radiative transfer calculations. VIIRS cloud top information is used when appropriate.

If the VIIRS cloud information is not available, the 1000 nm channel analysis will be used. If it is believed that a uniform cloud layer is present but altitude determination is difficult, a data set compiled from the International Satellite Cloud Climatology Project (ISCCP) is used to determine the cloud-top

pressure. This data-set, similar to the terrain data set described above, contains a 1° latitude by 1.25° longitude grid for each month.

A cloud reflectivity of 80 percent is assumed.

2.4.8.5 Cloud Fraction Determination

The OMPS algorithm accounts for the presence of clouds using a simple physical model that assumes a scene can be represented by two separate reflecting surfaces, one for the ground and one for clouds. The fractional contribution of each to the mixed scene limb radiance is given by

$$I(z) = I_{ter}(z) + f(I_{cld}(z) - I_{ter}(z))$$

where $I_{ter}(z)$ are the limb radiances for pure ground, $I_{cld}(z)$ are limb radiances for pure cloud and f is the cloud fraction. Since radiance changes due to surface reflectance and cloud fraction changes are largely indistinguishable, the surface reflectance must be specified prior to solving for cloud fraction. This limits the technique to the UV channels where the UV surface reflectance climatology is well known.

After the terrain surface height and reflectance is known and the cloud height/pressure has been determined, we solve for the cloud fraction. To preserve maximum sensitivity to cloud fraction, the solution method uses limb radiances that have not been normalized or ratioed. Because the influence of f on I appears at all altitudes, there is some degree of freedom available for selecting the limb radiance altitude range employed in the solution. For the 353 nm channel we use the limb radiances from 23 to 43 km. Use of multiple limb radiances will reduce the effect of precision errors on the cloud fraction calculations. Ozone absorption at this wavelength is extremely weak to non-existent and aerosol scattering is small when compared to Rayleigh scattering.

If $I_c(f, z)$ represents the calculated limb radiances for a mixed scene corresponding to measured radiances $I_m(z)$, we solve,

$$I_c(f, z) - I_m(z) = 0$$

The secant method provides a fast iterative solution to this equation for f . Recasting the previous equation leads to an expression for relative error,

$$RE(f) = 0$$

where

$$RE(f) = \frac{\sum_{z=23}^{z=43} [\ln(I_m(z)) - \ln(I_c(f, z))]}{\sum_{z=23}^{z=43} \ln(I_m(z))}$$

The secant method is iterated to solution. The secant iterations are uncoupled from the overall iterative updates associated with moving from the top to the bottom in Figure 2.4-1. The secant method requires RE calculated at two f before predicting a new solution. The first value of RE is calculated with an

initial value of f , f_0 . This initial value is either the surface reflectance set at the initialization stage or the value calculated during the last update. The second value is calculated by adjusting f_0 as follows,

$$f_1 = f_0 \frac{\sum_{z=23}^{z=43} \ln(I_m(z))}{\sum_{z=23}^{z=43} \ln(I_c(f_0))}$$

A new value of f , f_2 is predicted using the values of $RE(f_0)$ and $RE(f_1)$. The relative error is calculated for f_2 and then the surface reflectance with the largest relative error is dropped from the iterative process and the remaining two values are used in the next prediction. Typically, convergence is achieved within 8 iterations.

2.4.9. Neutral Number Density, Inversion and Profile Construction

Limb radiances and neutral number density single scattering kernels are calculated in the 347 and 353 nm channels using the most recently updated experimental quantities and normalized to limb radiance values at 61.5 km. Then the optimal estimation equation is used to produce an updated density profile. An example of the neutral number density single scattering kernels are shown in **Figure 2.4-4** for 350 nm, kernels for 347 and 353 are nearly identical. The sharp functional peaks result from the limb geometry.

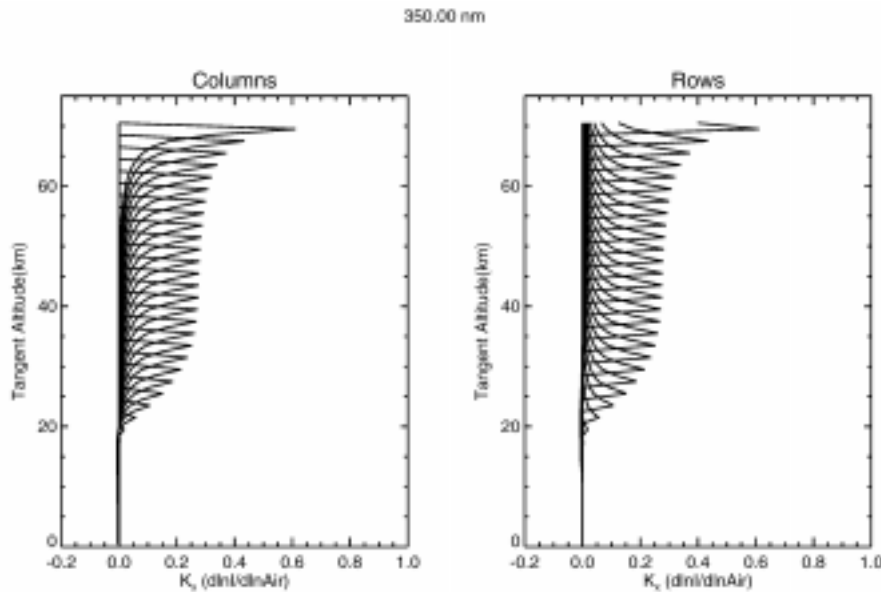


Figure 2.4-4. Single scattering kernels calculated assuming the M325 standard atmosphere with a solar zenith angle of 40° and an azimuthal angle of 0° .

The rows in this figure correspond to the standard graphical presentations of kernels. The column functions represent the delta function response of the limb radiances to a delta change in density. The kernels display excellent sensitivity from 20 to 60 km. Below 20 km the kernel amplitudes rapidly decrease and precision errors correspondingly increase. The CrIS temperature profile and derived pressure profile are used to construct a density profile. The CrIS derived density profile will be used in its entirety from the surface to 18km. Between 18 and 22 km the OMPS and CrIS derived density profiles will be blended to provide a smooth transition from one to the other. If the CrIS temperature and derived pressure are unavailable climatological values are used.

2.4.10 Aerosol Inversion

Limb radiances and aerosol single scattering kernels are calculated in all the aerosol channels (400, 500, 525, 675, 1000nm) using the most recently updated experimental quantities and are normalized to limb radiance values at 61.5 km. Next, the optimal estimation equation is used to produce an updated aerosol extinction profile for each one of the aerosol channels. The Angstrom power law is used to model the wavelength dependence of the aerosol.

$$\alpha = -\Delta \ln(\text{extinction} / \text{km}) / \Delta \ln \lambda$$

α varies with altitude and ideally should only be applied at wavelengths bracketed by the wavelengths used in its derivation. Aerosol extinction at the ozone channels of 575 and 602 nm would be calculated with α calculated from the 525 and 675 nm channels. In low accuracy situations, the Angstrom power law can also be used for extrapolation. Aerosol extinction at 347 and 353 nm will be calculated with α calculated from the 400 and 500 nm channels.

It is anticipated that the aerosol inversion can be carried down to 18 km at 400nm, at least 15 km at 525 nm, and at least 10 km at 675 and 1000nm.

2.4.11 Ozone Inversion

Limb radiances and ozone single scattering kernels are calculated in all the ozone channels using the most recently updated experimental quantities and normalized to limb radiance values at 61.5 km. The 290, 293, 296, 299, 302, 310, and 320 nm channels are paired to the 353 nm channel in the UV spectral region. In the visible the 575 and 500 nm channels are paired and the 602, 525, and 675 nm channels are combined in the triplet formulation. At altitudes where aerosol cannot be inverted, the 575-500 nm pair will be replaced with a 575, 500, and 675 nm triplet to take advantage of the linear aerosol correction provided by the triplet formulation. Next, the optimal estimation equation is used to produce an updated ozone profile. A subset of the single scattering kernels are shown in **Figure 2.4-5**. The sharp functional peaks result from the limb viewing geometry.

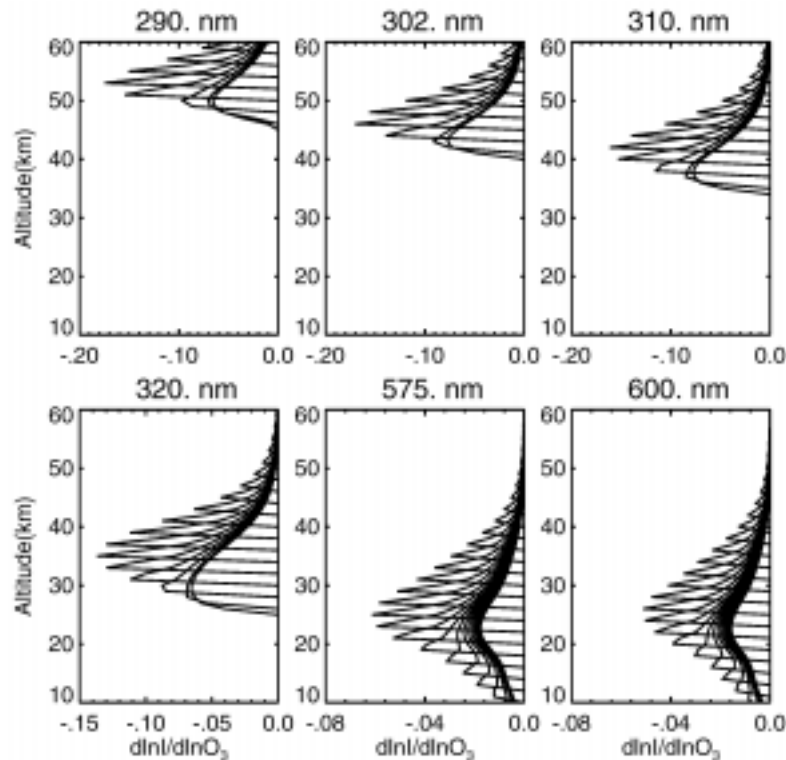


Figure 2.4-5. Single scattering kernels calculated assuming the M325 standard atmosphere with a solar zenith angle of 40° and an azimuthal angle of 0° . Not all baseline channels shown.

2.4.12 Convergence Criteria

To account for the interplay between the surface reflectances, cloud fraction, neutral number density, aerosol, and ozone in the limb radiances requires an iterative solution. The order of these steps was specifically designed to provide rapid ozone convergence by ensuring the ozone inversion always uses the most recent experimental values. As shown in Figure 2.4-1, the iterative return loop runs from the convergence criteria step back up to the beginning of the scene characterization process. Each time the loop is traversed density, aerosol, and ozone undergo one iterative update. However, visible surface reflectance and cloud fraction are iterated to solution for each loop traversal.

To date, ozone and neutral number density have been found to converge with three updates or loop traversals even when solving for visible surface reflectance and cloud fraction simultaneously. A fourth or fifth update has been found to have negligible effects on the inverted profile. Aerosol inversions should exhibit similar traits. It has not yet been necessary to establish specific convergence tests but the convergence criterion process box in Figure 2.4-1 has been retained for future use.

The entire system of equations has excellent convergence qualities because of the choice of channels and the manner in which they are used. The high altitude ozone derived from the UV channels are unaffected by surface conditions. The neutral number density-cloud fraction channels are independent of the ozone values and largely independent of aerosol. The same channels can be used for each by switching between normalized and un-normalized radiances. Visible surface reflectances are calculated with limb radiances where ozone and aerosol display small effects. The aerosol channels were chosen for their low ozone absorption. Of course, Rayleigh scattering effects are present in all of the channels, but they in turn depend on the neutral number density profile for which a good estimate is available.

2.4.13 Ozone Conversion to Mixing Ratio

All of the radiative transfer and atmospheric modeling governing equations are cast using number density to specify constituent levels. The SRD requires that ozone be reported in terms of volume mixing ratio. The neutral number density profile will be used to convert the ozone profile from number density to volume mixing ratio.

2.4.14 Horizontal Inhomogeneity Correction

Ozone variations along the limb line-of-sight (LOS) may not be symmetrical about the tangent point and could cause errors in inverted limb observations. The effect of asymmetry on limb viewing inversions has been studied (Boughner et al., 1980) and Rinsland et al. (1984) developed correction methods using photochemical model runs for species whose rapid photochemistry causes significant variations across the terminator. They successfully applied these asymmetry corrections to the retrieval process for NO and NO₂. In the OMPS limb-viewing geometry, photochemically-induced variations in ozone are not significant. However, similar to the concept applied in the above studies, we can construct correction fields for ozone spatial variations along the LOS by using the readily available ozone measurements from the OMPS nadir sensor.

From the nadir total column ozone, ozone profiles are reconstructed using the TOMS V7 standard profiles for the orbital swath along which the limb sensor is making profile measurements. These ozone profiles are combined with the simultaneous nadir profile data. The nadir profile provides reliable data particularly from the ozone peak up. Used with the total column measurements, this will help constrain the information on the ozone LOS variation to regions below the ozone peak. The variations along the LOS below the peak are approximated by the variations in the derived “adjusted” TOMS standard profiles. The reconstructed ozone profiles produce a two-dimensional ozone field. This field defines the relative variation of ozone along the limb LOS from which correction factors to the tangent layer ozone value can be computed and applied during the ozone limb retrieval.

Figure 2.4-6 is a representation of the limb viewing geometry for an n-layer atmosphere with each layer equal to 1 km. The optical depth along the LOS, τ (s, s'), is described on page ATBD LP-7. For a n-layer atmosphere at layer j as illustrated in Figure 2.4-6:

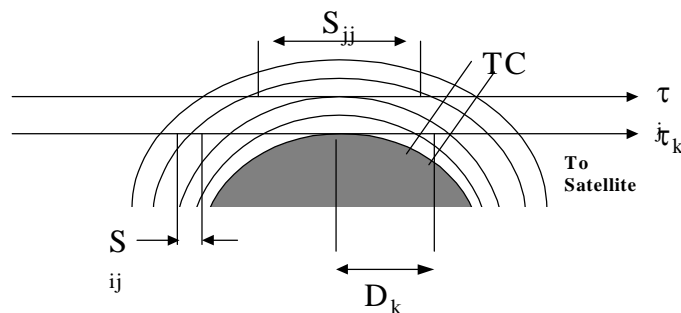


Figure 2.4-6. Limb viewing geometry for an n-layer atmosphere

$$\tau_j = 2 \sum_i \kappa_j \rho_i S_{ij} \quad (2.4.14-1)$$

where κ_j is the limb attenuation coefficient, ρ_i is the ozone number density, and S_{ij} is the path length for the LOS path through tangent layer j and the i atmospheric layers.

For an inhomogeneous atmosphere equation 2.4.14-1 becomes:

$$\tau_j = \kappa_j \sum_i (\rho_i^+ + \rho_i^-) S_{ij} \quad (2.4.14-2)$$

where ρ_i^+ is the density in the i^{th} layer nearest the satellite (in front of the tangent point) and ρ_i^- is the density in the i^{th} layer farthest from the satellite (behind the tangent point). For diagonal terms, ($i = j$), $\rho_i^+ = \rho_i^- = \rho_i$.

With the following definitions

$$\begin{aligned} C_i^+ &= \rho_i^+ / \rho_i, \text{ and} \\ C_i^- &= \rho_i^- / \rho_i. \end{aligned} \quad (2.4.14-3)$$

τ_j becomes:

$$\tau_j = \kappa_j \sum_i \rho_i (C_i^+ + C_i^-) S_{ij} \quad (2.4.14-4)$$

The coefficients, C_i , are constructed from the nadir total column measurements (TC) in the following manner. Each TC measurement is determined through a process of interpolation and fitting of the TOMS standard profiles as described in the ATBD-TC, IN0092A-106 (pages 9-11) and in the Nimbus 7 TOMS User's Guide (McPeters et al., 1996). The TOMS standard profiles are derived from eigenfunctions that span a climatology of over 23,000 ozone profiles derived from SAGE II and balloonsonde measurements. The correlation between total ozone and the coefficient of the primary eigenfunction, which represents most of the ozone peak, is 0.87 (Wellemeyer et al., 1997). Subsequently each final TC value has a unique "adjusted" TOMS standard profile associated with it. This TC equivalent profile can be expressed in 1 km layers from 0 to 50+ km. The distance between the measured TC for each LOS path length, S_{ik} , and the k^{th} tangent layer is determined from the TC geolocation data and indicated by D_k as shown in Figure 2.4-6. All TC measurements located within the measurement volume of S_{ik} are averaged together.

The coefficients C_i^+ and C_i^- are determined along the LOS for layer j using the corresponding values of ρ_i^+ , ρ_i^- , and ρ_i . The coefficients, C_i , are subsequently applied to the calculation of τ_j . The inhomogeneous atmospheric model uses the measured values of the ozone gradients as observed by the nadir sensor, accounting for spatial variations. The analysis is applied to each limb radiance channel.

We have examined this atmospheric inhomogeneity model by using Nimbus-7 TOMS measurements from September 18, 1992, to study C_i along a constant longitude strip of 100 degrees west. We chose this day and this longitude because they include examples of a steep gradient at the edge of the ozone hole (at 62°), a homogeneous atmosphere (at 0°), and a frontal zone region (at 45°). Figure 2.4-7 (top)



illustrates the TOMS TC results for this day, with the solid white line on the map indicating the longitude strip and the crosses indicating these 3 points along the strip.

For each degree of latitude along the strip, we determined the unique profile used by the Version 7 algorithm to calculate total column ozone. We then used these profiles to calculate, for the 3 points mentioned above, the inhomogeneity coefficients C_i at 15, 20, 25, and 30 km tangent heights at 50 km intervals along the limb retrieval LOS at positions both nearer to the satellite (ρ_i^+ from equation 2.4.14-3) and farther from the satellite (ρ_i^- from equation 2.4.14-3). Figure 2.4-7 (bottom) shows the results.

At the equator the coefficient remains close to 1, indicating that the ozone field is relatively constant and there is little variation in ozone in the ozone profile along the LOS. At 45 degrees north latitude, the effect of the ozone gradient at the boundary of the front is clearly seen, particularly in the lower stratosphere. At the higher atmospheric layers, both in the tangent height and along the LOS, the coefficients remain close to 1, again indicating little variation.

At 62 degrees south latitude, the effect of the strong ozone gradient on either side of the polar vortex is evident. In this case, the coefficient at large distances far from the satellite does not return close to 1, indicating profile variability remains at high altitudes (50 km). However, the effect of these large coefficients on the LOS optical depth is reduced by the ratio of the lower density at 50 km to the tangent point density, about an order of magnitude.

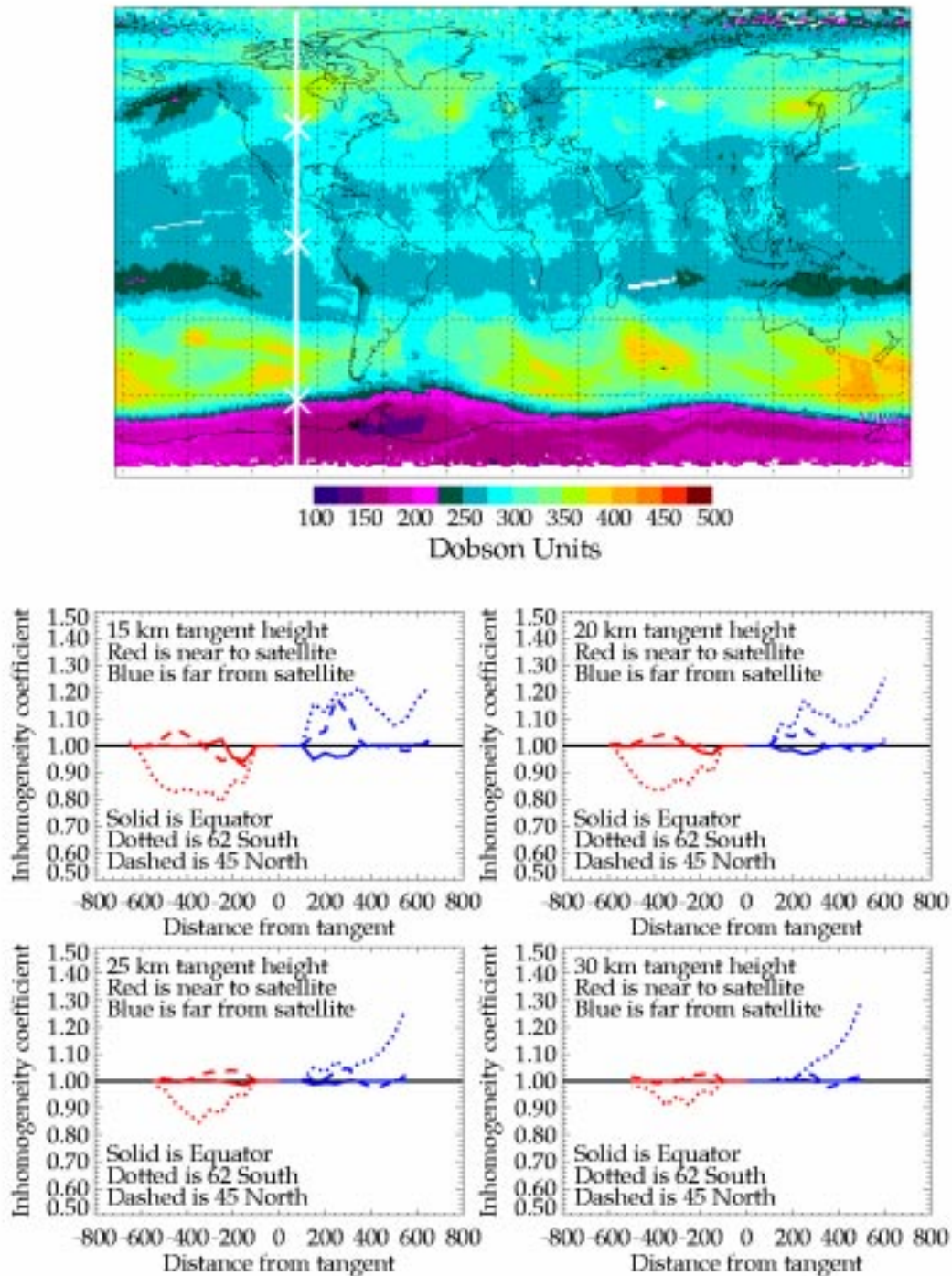


Figure 2.4-7. (Top) Nimbus 7 TOMS ozone from September 18, 1992. (Bottom) Inhomogeneity coefficients derived for the three observation points indicated by crosses, as described in the text.

The profiles for this tangent point (62 degrees) as well as the profiles nearer to (67 degrees) and farther from (57 degrees) the satellite are shown in Figure 2.4-8. From this figure it is clear that the variability results from differences in the TOMS standard profiles for total ozone values at the vortex (226 DU) and away from the vortex (306 DU) at altitudes greater than 40 km. This variability may not be actually

present in the real atmosphere. But in cases such as these, measurements from the OMPS nadir profiler will be very useful in constraining the derived variability to regions below the ozone peak.

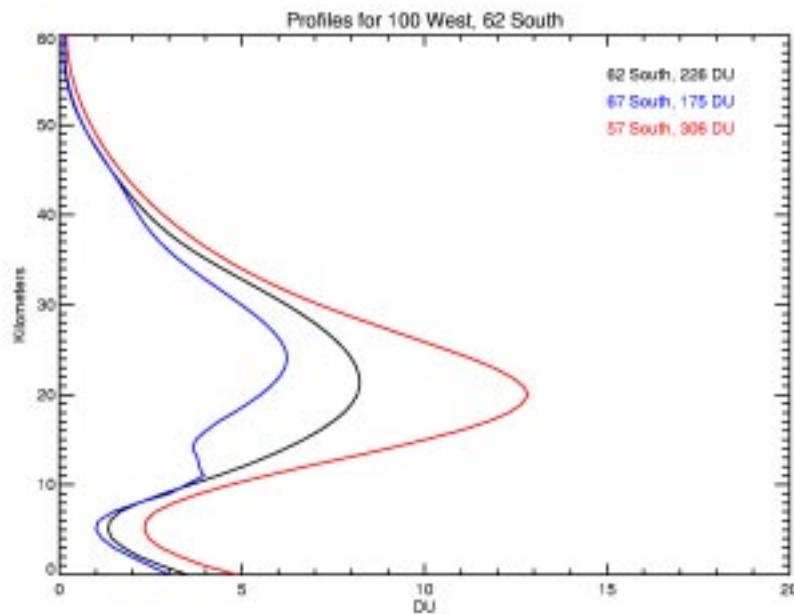


Figure 2.4-8. Profiles at 57S, 62S, and 67S, representing the strong ozone gradient across the polar vortex. The 62S profile represents the tangent point. The 57S (67S) profile is representative of the profile behind (in front of) the tangent point from the perspective of the OMPS limb sensor.

Variations in the Rayleigh and aerosol scattering along the LOS will also occur. Rayleigh scattering variations will be caused by density variations along the LOS. Density variations along the LOS should be smaller than those associated with ozone. While the density inversion may produce a density profile that is slightly in error due to the LOS density gradients, use of the density profile at other wavelengths should properly reconstruct the Rayleigh scattering contribution to the limb radiances. If modeling studies do not support this assumption, the CrIS temperature external EDRs and derived pressure profiles can be used to construct a density field. Inhomogeneity correction coefficients can be constructed for density as was described for ozone. After a recent volcanic eruption, LOS gradients in aerosol might exceed that expected for ozone. After enough time has passed to allow for horizontal and vertical mixing to take place, the gradients will decrease. We make the same argument for aerosol as was made for density. LOS gradients may cause errors in the inverted aerosol profiles but it should be possible to reconstruct accurate limb radiances at other wavelengths even with the slightly inaccurate aerosol profiles.

The net effect of variations in surface and cloud reflectivity below the LOS appears in the diffuse radiation field. We use the diffuse field to solve for “effective” visible surface reflectances and cloud fraction. Thus, the effect of these variations is already accounted for by the EDR algorithm. The algorithm also exhibits error compensation. Cloud fraction is calculated from limb radiances in the 350 nm region using an assumed cloud reflectivity. If the cloud fraction should be incorrect for some reason, or if the cloud reflectivity is different at the visible wavelengths than at 350 nm, an incorrect visible surface reflectance will be calculated. However, the cloud fraction, visible cloud reflectance value, and visible surface reflectance, when used together in the limb radiance calculations, will produce the correct limb radiances. In addition, errors in properly defining the lower boundary reflectivity parameters will



[be reduced by altitude normalization. Modeling studies represent the best approach to verifying algorithm performance when variations in surface reflectivity parameters occur under the LOS.](#)

2.5 Error Sources

Table 2.5-1 summarizes the sources of error in the limb profile algorithm. Section 7 provides more detail about each error and how it affects the ozone retrieval.

Table 2.5-1. Sources of error affecting the accuracy and precision of the ozone retrieval

Sensor Accuracy	Algorithm Accuracy
Wavelength dependent albedo calibration	Rayleigh scattering coefficients
Wavelength independent albedo calibration	Absolute ozone absorption coefficients
Linearity of electronics and CCD	Temperature dependent ozone absorption coefficients
Wavelength calibration	Aerosol
Wavelength shift	Cloud top and surface pressure
Polarization	Multiple scattering table interpolation
Out-of-field stray light	Neutral number density
Out-of-band stray light	Non-homogenous surface reflectivity
Sensor Precision	Algorithm Precision
Wavelength signal-to-noise	Temperature dependent ozone absorption coefficients
Solar calibration	Neutral number density
	Aerosol
	Surface and cloud top pressures
	Surface reflectivity
	Cloud reflectivity
	Cloud fraction
	Inter-slit inhomogeneity
	Inhomogeneity along line-of-sight

3. Algorithm Description

3.1 SDR Production

This section describes the process by which Sensor Data Records (SDRs) are generated. The discussion follows ICSR-8092402. Each SDR is primarily an archival product containing both calibrated and uncalibrated radiances. We have taken the philosophy that each SDR should contain all the information necessary, under normal circumstances, for a retrospective processing of the raw data into EDRs. As such, SDR processing uses inputs from the following sources:

1. RDR headers and records
2. Geophysical databases
3. EDR products from other sensors
4. Time-dependent calibration factors

External data, either climatological values or EDRs from other NPOESS sensors, are stored in the SDR. Climatological data include:

- terrain height data
- cloud height climatology
- temperature, pressure, and neutral number density profile
- snow/ice climatology

In the case of EDRs, the data is appropriately co-located with OMPS data cells. External EDRs include:

- temperature, pressure, number density profiles – CMIS and CrIS
- cloud cover – OMPS-Total Column or VIIRS
- cloud top pressure – VIIRS, CMIS, and CrIS
- snow/ice coverage – VIIRS and CMIS
- column ozone – OMPS-Total Column
- profile ozone – OMPS-Nadir Profiler

The threshold horizontal and vertical cell sizes specified by the VIIRS, CMIS, and CrIS SRDs for the external EDRs listed above are sufficient for OMPS. The co-location of the external EDRs with OMPS data cells is performed as part of SDR processing and is based on time tags.

Calibration data are detected in the SDR data stream and analyzed. Some, but not all, results from the calibration analyses are fed back automatically as calibration updates for use in subsequent SDR processing. All derived calibration parameters are part of an extensive monitoring database which is used to assess the quality of SDR (and ultimately EDR) products. This database alerts the science team to problems with the products, and points the way towards further data studies.

3.1.1 SDR Description

Sufficient information should be contained in the SDR to permit complete retrospective processing of the data and detailed analysis of the data. Records such as uncalibrated sensor signals should be included, since it is likely that these data would be re-calibrated in any reprocessing. The processes of housekeeping data conversion and radiance data geolocation are unlikely to be repeated, so their precursors need not be saved in the SDR.

Sensor data records are organized in files. The SDR files shall contain all science data, information related to the sensor observation, and the state of a sensor needed to produce EDRs for that sensor. A SDR file can cover any length of time, but because downlinked RDR data must be sorted and ordered sequentially prior to SDR processing we envision the minimum coverage of an operational SDR file to be one full orbit.

The following information shall be written in the header record of each OMPS-Limb SDR file:

- SDR identification tag
- Spacecraft identification tag
- Sensor identification tag
- Generation software name
- Software version numbers: Flight & SDR
- Generation date and time
- Processing environment
- Ancillary data file names and version numbers
- Beginning Julian date and time tag
- Ending Julian date and time tag
- Channels included, including current band centers
- Reference solar flux
- Radiance calibration coefficients used

Each individual sensor data record is associated with a group of data cells representing the full 38 s integration period. The contents of each record are as follows:

- Orbit Number
- Ascending Node date and time tag
- Transmission date and time
- Operation mode
- Data quality flags
- Date and time at start & end of period
- Date and time at end of sequence
- Subsatellite Lat, Lon at start & end
- Spacecraft altitude at start & end
- Solar right ascension at start & end
- Solar declination at start & end
- S/C centered solar azimuth at start & end
- S/C centered solar elevation at start & end
- S/C geocentric position (X,Y,Z) at start & end
- S/C attitude (difference from nominal; in Roll, Pitch, Yaw) at start & end
- Sensor status bits
- Sensor housekeeping data
- FOV Lat, Lon
- FOV solar zenith angle, satellite zenith angle, and relative azimuth angle
- Cloud top pressure – VIIRS, CMIS, *or* climatology
- Cloud coverage – OMPS-Total Column or VIIRS
- Terrain pressure – database
- Surface category and UV reflectance – database

- Snow/Ice coverage – VIIRS and CMIS *or* climatology
- Ozone profile amounts – OMPS Nadir Profiler *or* climatology
- Ozone column amounts – OMPS Total Column
- Temperature profile – CMIS and CrIS *or* climatology
- Pressure profile – CMIS and CrIS *or* climatology
- Neutral number density profile – CMIS and CrIS *or* climatology
- Calibrated earth radiances
- Raw (uncorrected) sensor counts

A more precise description of the SDR content is given in the Algorithm Specification Document.

3.1.2 Method

SDR generation for the Limb sensor begins by ingesting the RDR product for the time period of interest. The RDR file can represent a fraction of an orbit of data. The processing flow for each raw data record is shown in **Figure 3.1-1**. Indices in the figure are used as reference points for descriptions in the following sections. The process begins by converting housekeeping data into temperatures, voltages, etc. Corrections to the raw science signals are then performed. These can include any thermal or other environment-related adjustments. Each resulting science data element is tagged with a spacecraft clock time. Once a time is assigned to an OMPS data element, matchups with other EDRs can proceed. Orbital locations are computed using the ephemeris data. An appropriate spacecraft attitude, as determined by the flight software, is assigned to each science data element.

The processing path then splits for earth radiance and solar irradiance data. Earth data are geo-located and view angles computed. Solar angles are computed for both radiance and irradiance data. The remainder of the solar data flow and calibration are discussed in section 3.1.3

Earth radiances are calibrated by dividing by the measured solar irradiance. An external calibration file, ACF, contains time-dependent calibration adjustments based on solar data. The adjustment values are ingested and used to generate normalized radiances. Finally, all time-independent calibration adjustments are applied to the radiance data. The normalized, calibrated radiances are written to an SDR along with the other data stored for output.

A second input to sensor calibration is band center registration. Unlike the Nadir sensor, results of wavelength monitoring will be included in the SDR for use in EDR processing. The non-grating design of the Limb sensor optics means that band center variations are much more likely than for the Nadir sensor. An external file containing band centers, WVCAL, is ingested and written to the header of each SDR file.

The following are discussions of individual portions of the SDR processing algorithm.

Housekeeping Data: Sensor housekeeping data generally includes information from thermistors, currents and voltages. They can also include any feedback from mechanical systems, command verification, etc. Most housekeeping data, particularly from thermistors, is telemetered in raw form and must be converted (1) to a physical quantity. Only converted quantities are written to the SDRs. Conversions algorithms are provided by the OMPS sensor contractor. These data generally do not require time tagging because they vary slowly. In cases where multiple measurements are available for a single data cell, results are averaged. A historical summary of housekeeping data is maintained in a file called HOUSKP for use in offline analysis.

A major part of the housekeeping algorithm will be analysis of flat-fielding lamp data. This analysis is part of housekeeping since the lamp data will not be used operationally in sensor calibration. Mean pixel responses are computed and written to the LAMP file.

Sensor response correction: The science data may require initial corrections (2) prior to applying the calibration. An example of such a correction is an adjustment for radiometric response dependence on sensor temperature. Zero offsets, such as from dark currents, are subtracted here. If any stray light correction is required, it will be applied at this point in the processing.

Another type of correction involves the removal of bad-pixel information from the data stream. This removal occurs in the flight software prior to binning. Information related to pixel removal is contained in the RDR. The calibration change resulting from such a removal will be handled automatically through the sensor calibration procedure, but only as a smooth change over many weeks. A database of calibration shift sensitivities, generated during prelaunch testing, can be used to immediately correct for most or all of the shift caused by pixel removal. Any residual change is then accounted for slowly through the normal sensor calibration.

Time tagging and geo-location: A start and end spacecraft clock time is assigned to a data cell using the relationship between the instrument and spacecraft clocks (3). Time tags accompany data elements and are written in each SDR. It is then possible to relate each data element to other pieces of information such as ephemeris, spacecraft attitude, and external EDRs. Using the ephemeris, a spacecraft location is associated with each data element. The RDR contains any adjustments from nominal for spacecraft attitude. If more refined adjustments are available through post-processing by the TSPR contractor, these are ingested at this time. Attitude corrections are assigned to data cells via the time tag (4). Earth radiance data can then be geo-located (5). Solar illumination and sensor view angles are calculated (8) for the center of each data cell. Spacecraft centered solar illumination angles are calculated (13) for any solar irradiance data. All angles accompany data elements and are in each SDR.

Data cell altitude registration is part of geo-location algorithm. This registration is first computed using the spacecraft attitude information stored on the RDR. Following data cell co-location with the Nadir Profiler EDRs, the Limb data cell altitude registration may be refined using the C- σ technique. Selection of the altitude registration source depends on the reported uncertainties in the Nadir Profiler EDRs.

Following geo-location of radiance data, climatological database quantities will be read in for the correct latitude, longitude and time (6). The values will be stored in the appropriate fields of the SDR. Climatological quantities are discussed in Section 3.1.1.

Altitude registration: We have investigated a method of altitude registration for the Limb profiler which does not rely on precise attitude information from the spacecraft. Attitude data included in each RDR are first used to establish a baseline altitude registration for the Limb sensor vertical cells. Co-located C and σ data from the Nadir profiler are then ingested and averaged for the center Limb cell. The C and σ data describe ozone profile in the "exponential" region of the atmosphere, generally above 3 mbar, and are computed in the Nadir Profiler EDR algorithm directly from calibrated radiances. Using the limb scattering forward model, theoretical limb radiances are generated as a function of altitude using the following formula

$$X = C p^{1/\sigma}$$

where C is the column ozone amount above 1 mbar and X is the column amount above a pressure p . A χ^2 minimization with the measured Limb radiances yields the most probable altitude registration of the Limb vertical cells.

EDR matchup: Each SDR may contain EDR information from OMPS Nadir, VIIRS, CMIS, and CrIS, if available. The geophysical quantities from each are listed in Section 3.1.1. EDR information will overwrite existing climatological values. In the event that an EDR parameter is unavailable or has been flagged as having poor quality, this information will not be read in.

EDR information will require minimal additional processing. Temperature profile information from CMIS and/or CrIS will be used to compute the tropopause height for each Total Column data cell. This algorithm will determine the altitude of the most probable temperature minimum given the available input data and their reported uncertainties.

The threshold horizontal and vertical cell sizes specified by the VIIRS, CMIS, and CrIS SRDs for the EDRs listed above are sufficient for OMPS. In all cases multiple horizontal cells must be combined to match the coverage of a single limb profiler data cell. The co-location of the external EDRs with OMPS data cells is performed as part of SDR processing (7) and is based on time tags. Once the orbital altitude and mounting angles for the various sensors are known, the relative geometry of all relevant data cells can be computed for each instrument in question, and is then constant. The overlap of two data cells from different sensors is then solely a function of the time difference between the cells. Differing integration times may require the summation of multiple and/or fractional EDR reporting intervals. In the case of interval fractions, an appropriate interpolation scheme for the sensor in question will be used. During SDR processing the appropriate external EDRs are selected for each OMPS data cell using a matchup table and time tags from each sensor. The matchup table consists of an EDR data cell mask for each Total Column data cell, and will be generated prior to or soon after launch.

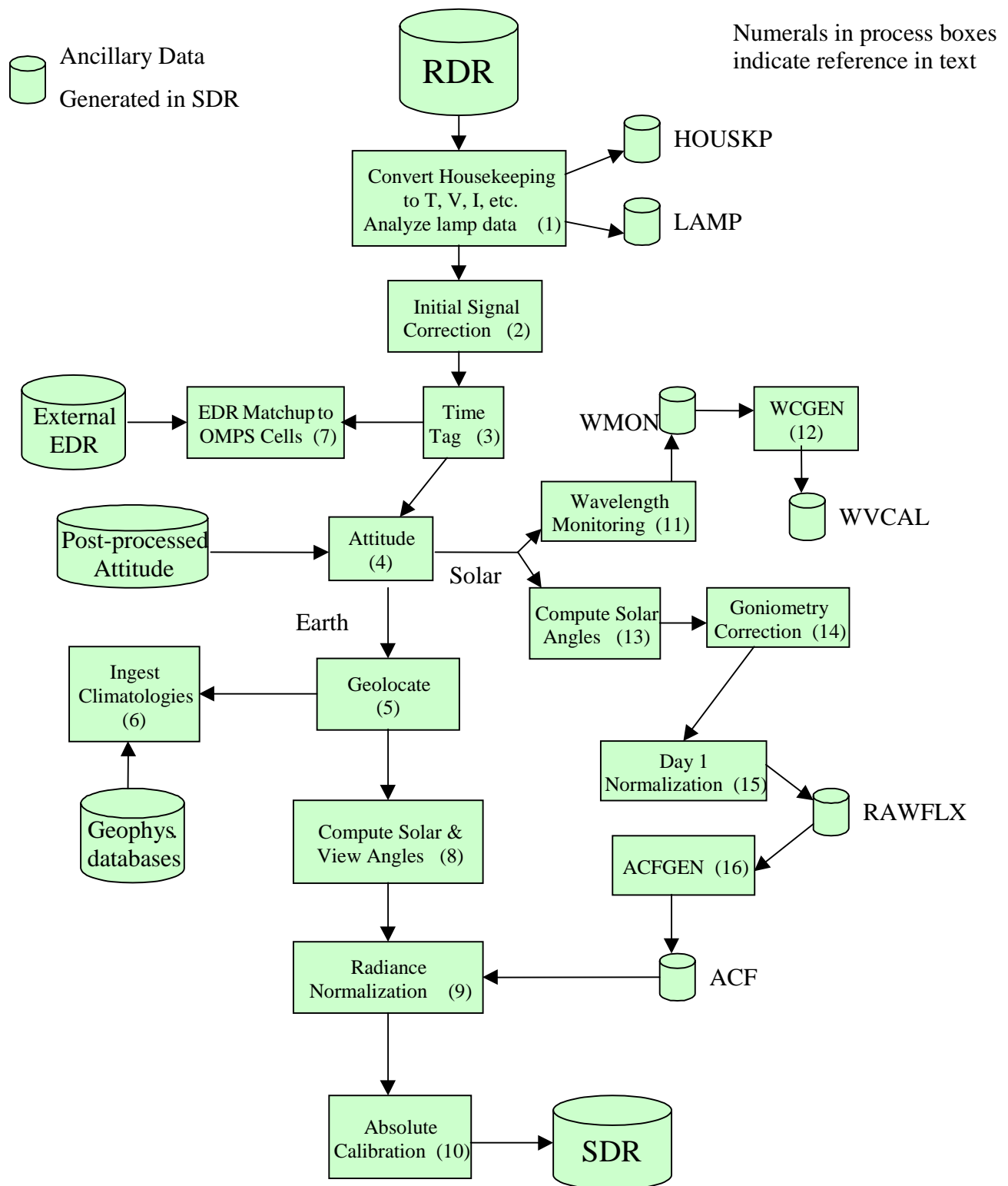


Figure 3.1-1. Schematic showing SDR generation process.

3.1.3 Calibration

The calibration concept for the Limb sensor follows closely that of the Total Column and TOMS. The TOMS calibration procedures are described in Jaross, et al., 1995, Seftor et al., 1997, and McPeters, et al., 1998. The implementation for OMPS has been described in ICSR-8092402. The use of diffusers is described in ICSR-8110501.

On-orbit changes in sensor response are tracked using the solar-irradiated, transmissive diffuser. Changes in the working diffuser are detected by comparing it with a infrequently-used and protected reference diffuser. This general approach is the same as for the Nadir sensor, except the Nadir sensor uses a reflective diffuser.

3.1.3.1 Theoretical Basis

Conceptually, the calibration of measured Earth radiance and solar irradiance may be considered separately. The measured Earth radiance in a single channel can be written as a function of the corrected instrument counts in the following way:

$$I_m(t) = \frac{C_r k_r}{\tau(t)}$$

where

- $I_m(t)$ = derived Earth radiance
- C_r = radiance counts, corrected by Initial Signal Corrections algorithms
- k_r = radiance calibration constant (from pre-launch calibration)
- $\tau(t)$ = sensor throughput changes ($\tau(t=0) = 1$)

The measured solar irradiance, F_m , can be written as:

$$F_m(t) = \frac{C_i k_i}{g \rho(t) \tau(t)}$$

where

- C_i = irradiance mode counts (corrected)
- k_i = irradiance calibration constant (from pre-launch calibration)
- $\tau(t)$ = sensor throughput changes ($\tau(t=0) = 1$)
- $\rho(t)$ = solar diffuser plate transmission ($\rho(t=0) = 1$)
- g = relative angular correction for diffuser reflectivity

The constants k_r and k_i are not accurately determined separately. The primary quantity measured by UV sensors, and used to derive ozone from the Limb sensor, is the normalized radiance $I_m(t)/F_m(t)$. The advantage of this approach is that sensor throughput changes, τ , affecting both Earth and solar

measurements cancel in the ratio. The Limb retrieval algorithm has additional radiance normalization in altitude, but this does not remove all the retrieval sensitivity to changes $\tau(t)$. The expression for solar-normalized radiances becomes:

$$\frac{I_m}{F_m} = K \frac{C_r}{C_i} g \rho(t)$$

where K is a combined calibration constant for normalized radiances, often referred to as the Albedo Calibration Constant. This and g are determined in pre-launch calibrations. Since the sensor changes affecting both the Earth and solar measurements cancel in the ratio, the quantity critical to time-dependent calibration of the normalized radiances is the diffuser plate transmission, $\rho(t)$.

Monitoring of this quantity is carried out periodically by deploying the Reference diffuser. The initial deployment frequency will be once every 6 months, and may decrease once adequate statistics of Working diffuser change $\rho(t)$ are obtained. Section 3.1.3.3 contains a more detailed discussion of diffuser monitoring and diffuser deployment. Based on monitoring results, the Working diffuser changes estimated and adjusted automatically. However, adjustments to the rate of change are only introduced manually (in ACFGGEN). Since the diffuser changes affecting ozone retrievals occur very slowly, it may be years after launch (and possibly never) before statistically significant changes in the Working diffuser are observed. Consequently, adjustments to diffuser rates of change may occur only 2-3 times. These adjustments will only be made with the concurrence of the OMPS science team.

3.1.3.2 Diffuser Monitoring System

The diffuser monitoring approach is broadly based on the system used on TOMS instruments. The Nadir and Limb sensors each have two diffusers referred to as Working and Reference. The TOMS have a third diffuser, called Cover, but data from it have never been used for calibration. Each diffuser is protected from the space environment when not in use. Solar measurements using the Working diffuser are the main tool for monitoring changes in OMPS sensor calibration.

Reference diffuser solar measurements will facilitate long term sensor calibration by providing a correction for Working diffuser degradation. The Reference diffuser will be used between 1 and 5 times per year, depending on observed Working diffuser degradation rates. In a multi-diffuser monitoring system, the concept is not to directly measure the change in Reference reflectance, but rather to keep its exposure so low that the uncertainty in any change is within limits. These limits are based on the long-term ozone drift requirement of 2% over the life of the Limb sensor, and the retrieval sensitivities to calibration errors. The primary assumption in this monitoring concept is that degradation does not occur except in the presence of solar irradiation. All evidence from BUV instruments suggests this is the case (see Jaross et al., SPIE 3427, 1998). Given this assumption, the uncertainty in changes in Reference reflectance can be reduced practically to zero (note that when monitoring with a lamp there is always a lower limit resulting from the lamp measurement uncertainties).

When Reference measurements are made, Working measurements are performed on the preceding and following orbits to reduce the effect of goniometry errors. These errors are caused by light scattered onto the diffuser and are a large source of uncertainty in comparing solar measurements. Goniometry errors are repeatable with spacecraft orientation, so minimizing angle changes tends to minimize goniometry errors. The sensor calibration can be tracked with the Working measurements, using corrections for degradation, or with the Reference measurements, using Working measurements for

interpolation. The two approaches are functionally equivalent in a retrospective reprocessing. For operational calibration the former approach is simpler and results in smaller uncertainties.

3.1.3.3 Diffuser Deployment Schedule

The Working diffuser measurement schedule is driven not by degradation issues, but by sensor stability and solar measurement precision. Its schedule is discussed in ICSR-E8110501. The Working deployment frequency is driven primarily by the variance in solar measurements. This variance is mostly a result of errors in the goniometry correction, not a result of sensor noise. Weekly solar measurements are more than adequate for the solar variance observed on TOMS. We assume the same variance for the Limb sensor, and therefore recommend a 1 week Working deployment frequency. This frequency will be assessed, and adjusted if necessary, based on actual solar measurement variance observed in the initial post-launch period.

Reference diffuser exposure must be reduced in order to reduce its degradation uncertainty. From the discussion in Section 3.1.3.2 it would seem that the best Reference schedule would have one measurement at the beginning of the data record and one at the end, thereby minimizing the Reference degradation uncertainty. One obvious problem is that we cannot know when the end of the data record will occur. Also, we cannot assume that Working diffuser degradation will depend linearly on exposure. So, at least a few more Reference measurements are needed.

The estimates for $\rho(t)$ will be based on regressions of the Working/Reference ratio values. All BUY diffuser data indicate that diffuser degradation is a slowly varying, monotonic function, appropriate for regression. In fact, for the degradation rates we anticipate, the dependence on solar exposure should be approximately linear. When applying a regression to the Working/Reference ratios, the uncertainty in the derived reflectance ratio decreases with time for a given measurement frequency. Thus the Reference measurement frequency should be high early in the sensor life and decrease with time in order to maintain a constant Working degradation uncertainty.

Consider a 2% layer ozone uncertainty for the end-of-mission. Using the sensitivity to wavelength-dependent albedo calibration errors discussed in Section 7.1.1 implies an allowed diffuser degradation of about 0.5% between visible wavelengths. We estimate that an individual Working/Reference ratio has a 1σ wavelength-dependent uncertainty of about 0.25% (from TOMS/EP data). The degradation uncertainty at the end-of-mission can be found for various measurement frequencies by applying a 1st order regression in time, assuming that degradation is linear in solar exposure. Results indicate that semi-annual Reference measurements are required during the first 2 years in order to meet 2% ozone uncertainty. By Year 7, less than 1 deployment every 1.5 years is needed. Our baseline deployment schedule is once every 6 months.

3.1.3.4 Operational Processing

The expression for normalized radiances $I_m(t)/F_m(t)$, given in Section 3.1.3.1, implies that time-dependent calibrations (apart from diffuser changes) are obtained by merely computing the ratio of sensor radiance signal to sensor irradiance signal. But this is not possible, since solar irradiance measurements are obtained only once per week. The solution is to characterize changes in the solar signal in order that the ratio can be computed as though irradiance measurements had been simultaneous with Earth radiance measurements.

After solar angles are generated for irradiance data in the SDR processing (13), a goniometric correction g is applied (14). Data are averaged to obtain a single value for a solar measurement sequence. This quantity is, from the above expression for $F_m(t)$,

$$\frac{C_i(t)}{g(t)} = \frac{\rho(t)F_m(t)\tau(t)}{k_i}$$

where the goniometric correction g depends explicitly on time due to the slowly changing solar beta angle. From the baseline irradiance measurement immediately following launch,

$$\frac{C_i(0)}{g(0)} = \frac{F_m(0)}{k_i}$$

The goniometry-corrected solar signals are normalized by the baseline value (15) and the results $T(t)$ written to the file RAWFLX. The expression for each value $T(t)$ is:

$$T(t) = \frac{C_i(t)}{g(t)} \frac{g(0)}{C_i(0)} = \rho(t)\tau(t) \frac{F_m(t)}{F_m(0)}$$

For the wavelengths longer than 310 nm the solar fluxes are practically constant, and the values $\rho(t)$ are nearly 1. Thus the quantities in RAWFLX are an estimate of the sensor throughput changes since the baseline calibration.

The calibration algorithm (16) yields a characterization of the quantities $T(t)$. The inverse of this characterization is often referred to as the Albedo Correction Factor, $A(t)$. In fact, the ACF $A(t)$ is not a characterization but a prediction based on a characterization. In an operational environment with infrequent solar measurements, Earth radiance measurements always occur well in advance of solar measurements. The calibration algorithm, called ACFGGEN, adopts the TOMS procedure of using a first order regression of the preceding solar measurements to yield predicted $A(t)$ values. Predictions are made for at least one solar calibration period (1 week in this case), and are divided into discrete daily values. The ACFGGEN routine runs only when solar data are encountered and produces a new set of predictions beginning with the following day. A small discontinuity in an $A(t)$ generally occurs between the two days. The daily values of $\rho(t)A(t)$ for each channel are stored in the file ACF. The expression for normalized radiance becomes

$$\frac{I_m(t)}{F_m(t)} = C_r \cdot \left(\frac{Kg(0)}{C_i(0)} \right) \cdot \rho(t)A(t)$$

Returning to the main SDR processing flow (9,10), each radiance signal C_r is multiplied by $\rho(t)A(t)$, read from ACF, and then by the absolute calibration correction $Kg(0)/C_i(0)$ from pre-launch calibrations and the baseline post-launch calibration.

The same solar irradiance data used in radiance normalization is used to monitor shifts in sensor wavelength registration. The wavelength algorithm (11) runs when solar data is encountered in the RDR. Results are accumulated for a solar measurement sequence, averaged, and written to a summary file called WMON. The values stored in WMON cannot be used directly to adjust band center position

information because of their large uncertainties. The algorithm WCGEN (12) functions much the same as ACFGGEN by smoothing the raw results and producing a running prediction of band center wavelengths as a function of time. Before being written in each SDR, the values from WVCAL are adjusted to account for the known sensitivity to sensor thermal variations.

3.1.3.5 Wavelength Registration Monitoring

Both Limb and Nadir sensors will use the solar Fraunhofer spectrum to monitor postlaunch wavelength shifts. Separate monitoring algorithms are employed for each of the three focal planes. The readout position, in the spectral dimension of the CCD, of strong solar absorption lines is monitored by comparison to their reference positions. In the case of monitoring, these reference positions are determined from the baseline solar measurements immediately following launch. Each weekly solar measurement provides data on the readout position of the absorption lines that can be compared to their reference positions. This approach is similar to the monitoring algorithm currently used for the GOME sensor.

Three main factors affect the sensitivity of this technique to shifts in the sensor wavelength registration: solar measurement errors, the depth of the absorption features, and the density of Fraunhofer lines in spectrum of interest.

The latter factor favors wavelengths shorter than 500 nm. This is important because ozone cross sections in the UV are more sensitive to bandpass errors than are those in the VIS (see Section 7 for an assessment of retrieval errors from wavelength shifts). Because wavelength registration changes are well behaved spectrally (i.e. a functional form can usually be used to describe the shift at one wavelength based on the measured shift at another), a greater density of Fraunhofer lines reduces the shift uncertainty statistically in the particular spectral region of interest. Uncertainties in wavelength registration allocated in the PDR (see PDR pages 44 & 319) do not assume the combining of multiple lines as just described. The sparse information available from solar lines longer than 500 nm can also be augmented using atmospheric absorption lines, such as O₂ near 760 nm. We have not yet investigated using the earth spectrum, but believe it represents a viable option should solar lines in the VIS provide insufficient shift resolution.

Since our monitoring technique is sensitive to the depth of solar absorption features, potential errors exist from solar flux variations. Such variations are of consequence only for the Nadir profiler.

The WMON Algorithm

The algorithm begins by summing calibrated irradiances I_z in the spatial dimension

$$I_\lambda = \frac{1}{n-m} \sum_{z=m}^n I_{z\lambda}$$

Irradiances $I_{z\lambda}$ are determined in the solar analysis algorithm, described in Section 3.1.3.1. The irradiance mean is used to further reduce random pixel noise by combining up to 1/3 of the CCD used for solar measurements (approximately 40 pixels). By using only 1/3, we retain the ability to monitor wavelength shifts that vary along the entrance slit.

A subset of I are selected surrounding each Fraunhofer line, j . The width of the solar feature relative to the channel bandwidths is the main criterion for selecting each subset I^j . For most narrow features, three channels centered at the feature are sufficient. No added information is provided by additional channels unless shifts approach the channel bandwidth. A set of differences is then computed relative to the reference solar spectrum

$$D_{\lambda}^j = \frac{I_{\lambda}^j - I_{\lambda,ref}^j}{I_{\lambda,ref}^j}$$

The difference arrays provide a simple way to translate signal changes into wavelength registration shifts. As seen more clearly in high resolution, the difference at each strong absorption line consists of a positive and a negative portion on either side of the central channel (see **Figure 3.1-2**). The magnitude of these differences is directly proportional to the wavelength shift. A lookup table M_{DS}^j is used to relate irradiance differences and shifts S^j . For the simplest case of three channels: L_1 , I_0 , and I_1

$$S^j = (D_{-1}^j - D_1^j) M_{DS}^j$$

By using a difference of the differences, changes in the measured solar continuum (such as from sensor degradation) will cancel. The lookup table M_{DS}^j is generated once by introducing shifts in the reference spectrum and observing changes in the quantity $D_{-1}^j - D_1^j$. Generation of the lookup table is discussed below.

Values of S^j for all relevant solar absorption features are tabulated and stored in the WMON database (see Figure 3.1-1) each week. These data are the input to the WCGEN code, which produces a prediction for the band center wavelengths.

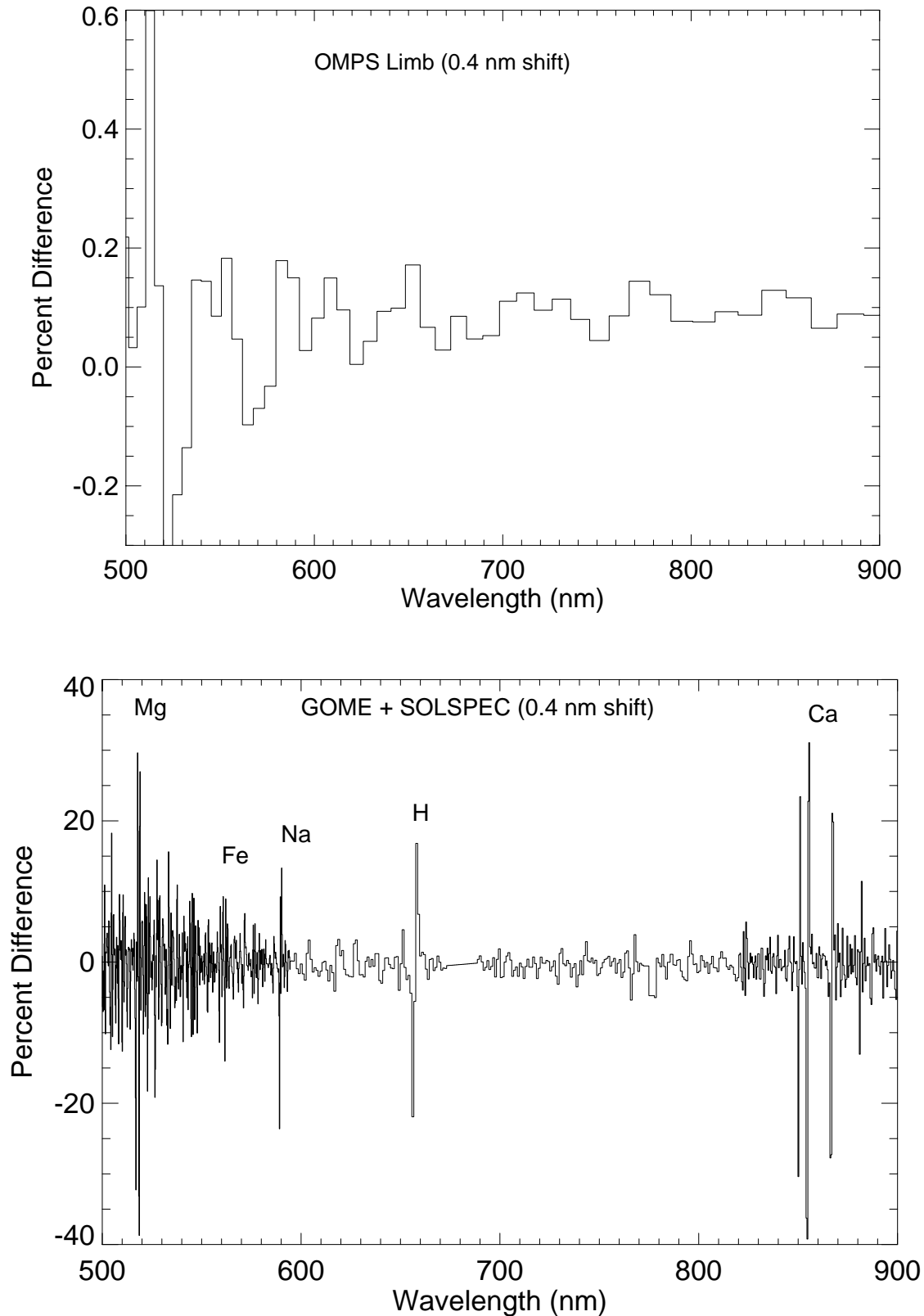


Figure 3.1-2. The difference spectrum is shown in the VIS at high resolution and at Limb sensor resolution. The difference spectrum is calculated by subtracting the measured (shifted) solar spectrum from a reference spectrum.

Wavelength Shift Resolution Study

We performed an analysis of the wavelength shift resolution achieved using the monitoring algorithm described above. For a single Fraunhofer line j , the shift resolution is defined as

$$\Delta S^j = \Delta(D_{-1}^j - D_1^j)M_{DS}^j$$

We generated lookup tables M_{DS}^j by simulating the solar spectrum measured by the limb sensor and by the nadir sensor.

We used GOME solar data to simulate the limb sensor measured spectrum from 300nm to 600 nm, SOLSPEC data from 600 nm to 820 nm, and Kitt Peak Solar Observatory data longer than 820 nm. The spectral resolution of all three is much greater than OMPS, so minimal errors are expected when degrading to the OMPS spectral resolution. The degraded spectrum then became the reference sensor irradiance spectrum, $I_{\lambda,ref}$. Band center selections did not exactly correspond to those reported in the PDR (see PDR page 350), but the final resolution is insensitive to shifts in the wavelength scale. A set of 21 of the deepest Fraunhofer lines were selected between 300 nm and 900 nm. The approximate wavelengths of these lines are shown in **Figure 3.1-3**.

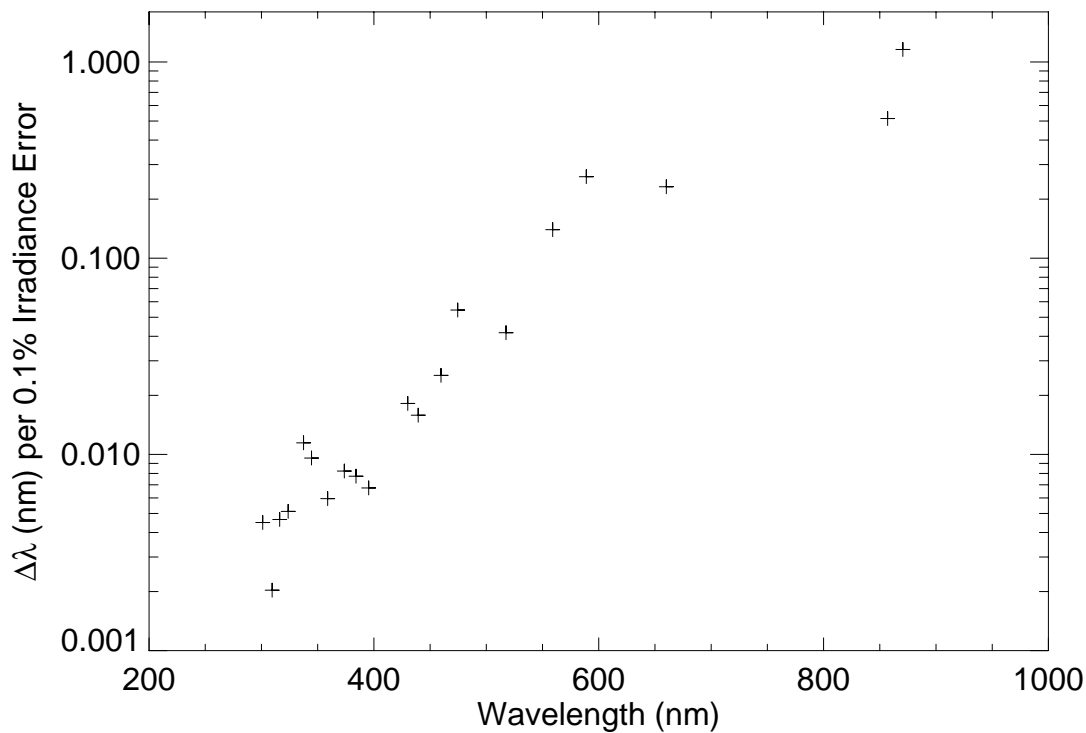


Figure 3.1-3: Wavelength registration shift sensitivities are shown for the Limb sensor WMON algorithm. Each point corresponds to a solar Fraunhofer line. Shifts are computed for a 0.1% irradiance error to indicate the anticipated shift resolution.

A lookup table M_{DS}^j was generated for each solar line j by introducing a series of band center shifts in the high resolution spectrum, regenerating the OMPS spectrum for each, and computing the quantity $D_{-1}^j - D_1^j$ for each. Ten wavelength shift values were used for each line, with the shift range varying according to the expected resolution. Each of the ten entries for M^j are computed as the ratio of the

wavelength shift to the irradiance difference. A single entry is not sufficient because the values of D^j do not vary linearly with the wavelength shift. The quantities M^j evaluated at zero wavelength shift are plotted in Figure 3.1-3. Sensitivities are plotted per 0.1% irradiance change. This is the expected wavelength-dependent uncertainty in OMPS irradiance measurements based on studies of TOMS data (see ICSR-8110501). Since the uncertainty is for a single channel, the value of $(D_{j-1} - D^j_1)$ is $\sqrt{2}$ times greater. Such small signal changes are still in the linear region of M^j , so the wavelength uncertainty S^j scales linearly with $(D_{j-1} - D^j_1)$.

Improvements to shift resolution

The sensitivities shown in Figure 3.1-3 are probably not the final shift resolution for the sensors. Fraunhofer lines do not necessarily fall on or near retrieval wavelengths (600 nm for ozone, for instance), so some form of interpolation between lines will be necessary. This implies knowledge of the functional form of wavelength shifts.

Assuming the functional form for wavelength shifts is standard practice for many sensors that lack monitoring at precisely the wavelengths of interest. The TOMS and SBUV/2 sensors use Mercury lamps whose emission lines are not optimally placed in wavelength. It is assumed for both that wavelength registration changes result from sensor stresses and component shifts that produce smoothly varying errors in wavelength. In particular, TOMS monitoring assumes that all stresses are manifest as a relative grating position error. Shifts measured at 296.7 nm are translated to shifts at the six TOMS channels via the sensor dispersion relation.

It is, therefore, reasonable to assume that OMPS wavelength shifts will also behave smoothly, and that information from many Fraunhofer lines can be combined to yield the most probable shift. We have investigated improvements to Limb sensor wavelength shift resolution by combining multiple solar lines as described above. We simulated the improved resolution by fitting measured shifts at each line to a quadratic function in wavelength. A quadratic was chosen because it closely matches the dispersion relation of the Limb sensor (driven by the prism). We anticipate that temperature-induced changes in the prism index of refraction will be the predominant source of registration shifts for the Limb sensor. Expected shifts are 2.5% of the bandwidth per 1° C.

We introduced a wavelength shift in the simulated Limb solar spectrum corresponding to a 4° C temperature change. The resulting shift is approximately 0.1 nm in the UV and almost 4 nm at 1000 nm. The irradiance values of the shifted spectrum were varied randomly to simulate measurement errors. The shift value S^j was retrieved for each line according to the procedure described in above. These S^j were then fit to a quadratic polynomial in wavelength. We chose to limit the regression to lines longer than 450 nm since the Limb ozone retrieval is most sensitive to errors in the visible wavelengths. The difference between the regression results and the input shift represents the wavelength monitoring error. We repeated the simulation for 2000 trials to develop an ensemble of shift retrieval errors. On average the error is zero since a quadratic closely approximates the original wavelength shift. The standard deviation of errors is shown in **Figure 3.1-4** for the cases of 0.1% and 0.2% 1σ solar irradiance error.

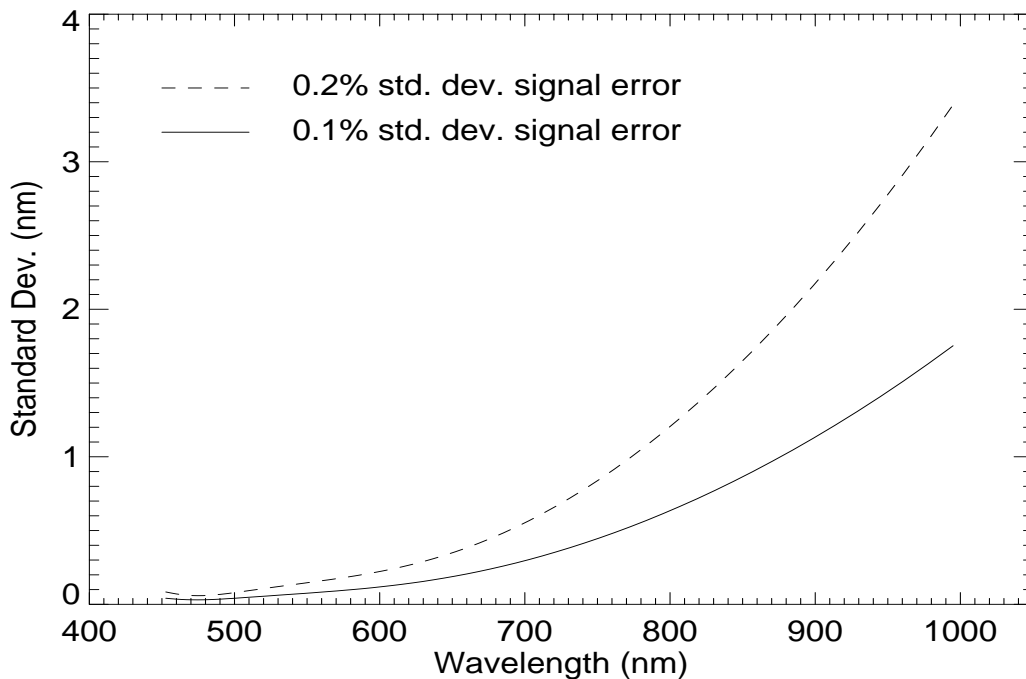


Figure 3.1-4. The shift resolution is shown for the VIS region of the Limb sensor for 0.1% and 0.2% irradiance uncertainties (1σ). The results assume a regression of the measured shifts from the 7 solar lines in this region.

The results of Figure 3.1-4 indicate a significant reduction in shift uncertainty shorter than 700 nm as compared to individual solar lines (Figure 3.1-3). This reduction is important from the standpoint of uncertainty in ozone absorption coefficients. The reductions are not as great between 800 nm and 1000 nm, but the large uncertainties there do not have a direct effect on ozone.

3.2 EDR Production

The following section describes how the UV/Visible/NIR limb profile EDR is produced from the OMPS UV/Visible/NIR limb sensor measurements. Later sections tell of the assumptions contained in the algorithm, and data needs of the algorithm. The algorithm description is presented as a step-by-step processing flow. It is limited to a description of the modules necessary to convert information in the SDR into the EDR ozone value and omits any references to the I/O and other routines.

1) **limb_edr_alg**

The routine **limb_edr_alg** is the main driver for the scientific algorithm.

1) **setup** (partially discussed in Section 2.4.7)

Initialize and set up needed variables.

1) **rdinfo**

Read in viewing geometry, a priori profiles, tangent heights, wavelengths, etc.

2) rdsdr

Read in SDR record.

3) mktanhit

Pre-calculate tangent height grid.

4) makcalc

Define storage structure for calculated limb radiances and associated data products.

5) load_mstab (Sections 2.3.2 and 2.4.8.2)

Load multiple scattering tables.

1) rdmstab

Read in:

- radius of earth (km)
- altitude of observer (km)
- number of tangent heights
- number of solar zenith angles for computations
- number of lambertian surface reflectances used in computations
- number of azimuths in tables
- tangent heights (km)
- solar zenith angle (deg)
- relative azimuth angle (deg)
- limb radiance for surface reflectance = 0 (I_0)
- single scattered radiance (I_{0ss})
- term of $I(r)=I_0+r*C1/(1-r*C2)$
- term of $I(r)=I_0+r*C1/(1-r*C2)$
- optical depth to the tangent point (τ)

6) lim_init4 (partially discussed in Section 2.4.7)

Choose initial profiles to start iteration with.

Set aerosol model parameters used in radiative transfer model.

The following steps (7 – 9) are iterated

lim_scene4

Determine surface characteristics. Solve for cloud fraction and visible surface reflectances (Sections 2.4.8.5 and 2.4.8.1)

1) lim_rad

Calculate limb radiance for cloud fraction wavelength.

7) lim_density (Section 2.4.9)

Main driver for air number density inversion.

1) lim_rad

Runs the forward RTM for the density wavelengths.

1) mk_flg_rt_in

Makes input file needed by for RTM model.

Spawn the radiative transfer model

2) rdcalc

Read in radiative transfer calculations performed by RTM model.

3) gmstab (Section 2.4.8.2)

Correct RTM calculations for multiple scattering.

1) tabl_tot_ss

Estimate the limb radiance for each tangent height of a limb scan, using the precomputed tables.

2) interpth

Interpolate limb scan at tangent heights using the table with sun and phi at tangent height and input (desired values) given at tangent point also:

- 1) For each tangent height, interpolate tables at each sun, phi value for particular tangent height.
- 2) Then interpolate for the particular ϕ using Lagrange 4 pt. interpolation of $\cos\phi$. Assume symmetry about $\phi=0$ & 180 and fill-in 2 extra model points on either side of $\cos\phi$.
- 3) Interpolate for the particular sun angle using Lagrange interpolation of $\ln(\text{chapman function})$ of sun with scale height of 7.0.

- 4) If the desired wavelength is not in the table, then will do an additional wavelength interpolation through the table to the desired wavelength. Interpolate table values to the actual data values.

- 2) **rdkern**

Read in the kernels.

- 3) **loadyynk** (Section 2.4.4 and 2.4.5)

Form channel to channel ratios (pairs, triplets) here

- 1) **g1yynk**

Perform radiance normalization and multiple scattering adjustments

Add ms terms to ss terms to get Itot (ss+ms).

Convert radiance into $\ln(\text{radiance})$ for each wavelength.

- 4) **onr**

Read in initial air density profiles.

- 5) **mlikeli** (Section 2.4.6)

Calculate the maximum likelihood solution for the given set of measurements and a priori profiles.

- 1) **invert**

Compute the inverse of variance of the estimated profile .

- 2) **chkinv**

Check the inverse of the variance of the estimated profile .

- 3) **pltmlikeli**

Plot the output of the maximum likelihood routine.

- 4) **wrtdata**

Write out data.

- 6) **chksolut**

Check for negative values of solution profile. If found, set to half of previous value

7) **onw**

Update the solution profile.

8) **lim_aerosol** (Section 2.4.10)

Main driver for aerosol inversion.

3) **lim_rad**

Runs the forward RTM for the aerosol wavelengths.

1) **mk_flp_rt_in**

Makes input file needed for RTM model.

2) **rdcalc**

Read in radiative transfer calculations performed by RTM model.

3) **gmstab** (Section 2.4.8.2)

Correct RTM calculations for multiple scattering.

1) **tabl_tot_ss**

Estimate the limb radiance for each tangent height of a limb scan, using the precomputed tables.

2) **interpth**

Interpolate table values to the actual data values.

1) **chap**

Calculate chapman function.

2) **rdkern**

Read in the kernels.

3) **loadyynk** (Section 2.4.4 and 2.4.5)

Form channel to channel ratios (pairs, triplets) here

1) **g1yynk**

Perform radiance normalization and multiple scattering adjustments

Add ms terms to ss terms to get Itot (ss+ms).
Convert radiance into ln(radiance) for each wavelength.

4) onr

Read in initial aerosol profiles.

5) mlikeli (Section 2.4.6)

Calculate the maximum likelihood solution for the given set of measurements and a priori profiles.

1) invert

Compute the inverse of variance of the estimated profile .

2) chkinv

Check the inverse of the variance of the estimated profile .

3) pltmlikeli

Plot the output of the maximum likelihood routine.

4) wrtdata

Write out data.

6) chksolut

Check for negative values of solution profile. If found, set to half previous value.

7) onw

Update the solution profile.

9) lim_ozo (Section 2.4.11)

Main driver for ozone inversion.

1) lim_rad

Runs the forward RTM for the ozone wavelengths.

1) mk_f1p_rt_in

Makes input file needed for RTM model.

2) rdcalc

Read in radiative transfer calculations performed by RTM model.

3) gmstab (Section 2.4.8.2)

Correct RTM calculations for multiple scattering.

1) tabl_tot_ss

Estimate the limb radiance for each tangent height of a limb scan, using the precomputed tables.

2) interpth

Interpolate table values to the actual data values.

1) chap

Calculate chapman function.

2) rdkern

Read in the kernels.

3) loadyynk (Section 2.4.4 and 2.4.5)

Form channel to channel ratios (pairs, triplets) here

1) g1yynk

Perform radiance normalization and multiple scattering adjustments

Add ms terms to ss terms to get I_{tot} (ss+ms).

Convert radiance into $\ln(\text{radiance})$ for each wavelength.

4) onr

Read in initial ozone profiles

5) mlikeli (Section 2.4.6)

Calculate the maximum likelihood solution for the given set of measurements and a given a priori.

1) invert

Compute the inverse of variance of the estimated profile.

**2) chkinv**

Check the inverse of the variance of the estimated profile .

3) pltmlikli

Plot the output of the maximum likelihood routine.

4) wrtdata

Write out data.

6) chksolut

Check for negative values of solution profile. If found set to half previous value.

7) onw

Update the solution profile.

The previous steps (7 – 9) are iterated

10) Convert ozone number density to volume mixing ratio (See Section 2.4.13).

11) Output EDR data record.

4. Assumptions

The following summarizes the assumptions described in Sections 2.3, 2.4, and 3.2.

Forward Model
The atmosphere's lower boundary consists of two Lambertian reflecting surfaces, one for the ground and one for clouds
Spatial uniformity of surface reflectance
Retrieval
The limb radiance can be treated as coming from a point source with viewing conditions given by those at the center of the pixel IFOV
Mixed scene can be modeled with two part model, terrain and cloud
The cloud's reflectivity is 0.8
Snow/ice reflectivity is 0.8
Spatial uniformity of surface reflectance assumed
Aerosol wavelength dependence can be modeled with Angstrom power law
Ozone absorption over a finite band can be characterized by an effective absorption coefficient
Rayleigh scattering over a finite band can be characterized by an effective scattering coefficient
Diffuse radiation field solution on tangent point zenith applicable at all points along line of sight
Ozone absorption, aerosol scattering, and Rayleigh scattering are the only physical processes occurring in the OMPS channels

5. Input Data Requirements

5.1 Primary Sensor Requirements

Table 5.1 outlines what the baseline algorithm needs and sensor allocations.

Table 5.1-1. Sensor parameters and performance required by the algorithm

Parameter	Baseline Algorithm Needs	Baseline Sensor Allocation	Comments
Wavelength range	290 -1000 nm	290 – 1000 nm	Ozone and aerosols
Bandwidth	3 nm (290), 5 nm (400) 16 nm (602), 40 nm (1000)	3 nm (290), 5 nm (400) 16 nm (602), 40 nm (1000)	Pair/triplet approach σ error
Samples/FWHM	0.5 or 1 depending on λ	1	λ shift
Number of channels	16	82 selectable to 16	Ozone and aerosols
Vertical reporting interval	1.0 km	1.0 km	Horiz. & vert cell
Vertical coverage	0 to 65 km	0 to 65 km	
Horizontal cell size	250 km	250 km	
Horizontal coverage	750 km	750 km	3 FOVs
SNR	270 –2570	150 – 4000	Ozone precision
Wavelength calibration	.01 FWHM max, 290-400 nm .03 FWHM max, 500-675 nm .10 FWHM max, 1000 nm	.01 FWHM max, 290-400 nm .03 FWHM max, 500-675 nm .10 FWHM max, 1000 nm	σ error
Albedo calibration	2%	2%	Accuracy and stability
Pixel-pixel response	<1%	<1%	Accuracy and stability
Stray light	0.5% max.	0.5% max.	Accuracy

* The 16 wavelengths are: 290, 293, 296, 299, 302, 310, 320, 350, 352.5, 400, 500, 525, 575, 602, 675, 1000 nm.

5.2 Other OMPS Sensor Data Requirements

Table 5.2-1 specifies data from other OMPS sensors required by the limb profile ozone algorithm.

Table 5.2-1. Data requirements for the nadir OMPS sensor

Sensor	Data	Form	Use
Total column	Total column ozone	Co-located, Dobson Units	Starting point for table look-up
Nadir profile	Profile ozone	Co-located, 3 km	First guess

5.3 Other NPOESS Sensor Data Requirements

Table 5.3-1 specifies data from other NPOESS sensors required by the UV/Visible limb algorithm.

Table 5.3-1. lists data products used by OMPS limb profile ozone retrieval coming from other NPOESS systems.

Sensor	Data	Form	Use
CrIS	Temperature-pressure profile	Co-located Kelvin	Temperature profile shape
VIIRS	Cloud fraction	$0.0 < f_{\text{cld}} < 1.0$	Normalized radiance calculation
VIIRS	Cloud top pressure	Co-located Atm	Partial cloud algorithm Calc of normalized radiances
VIIRS	Surface reflectivity	Co-located in percent Percent	Snow/ice indication Calc of normalized radiances

5.4 Climatology Data Requirements

Table 5.4-1 specifies climatological data required by the limb profile algorithm (note: some of the databases are only used if external EDRs are not available).

Table 5.4-1. List of data provided by climatological databases for the profile ozone retrieval.

Data	Form	Source	Use
Surface pressure*	1° x 1.25° grid In mbars	TUG87 geophysical model (see Weiser, 1987)	Calc of normalized radiances
Cloud pressure*	1° x 1.25° x 12 month In mbars	ISCCP	Partial cloud algorithm Calc of normalized radiances
Snow/ice*	1° x 1.25° x 12 month In percent probability	Air Force	Snow/ice indication Calc of normalized radiances
Eclipse	Areal coverage	Astronomical almanac	Flag data
Ozone profile*		TOMS standard profiles	First guess
Temperature profile*		NMC	First guess
Density profile*		NMC	First guess
Ozone profile		HALOE/SAGE	A priori
Density profile		NMC	A priori
Aerosol		SAGE	A priori

*Used if external EDR not available

6. Output Data Description

6.1 EDRs

The specifications for the EDR are given in the **Table 6.1-1**.

Table 6.1-1. UV/Visible limb EDR specifications

SRD Paragraph No.	Description	Allocated (Assured) Performance
SRDO3.2.1.1.1.1-2	Horizontal cell size	250 km
SRDO3.2.1.1.1.1-3	Horizontal Reporting Interval	250 km
	Vertical Cell Size	
SRDO3.2.1.1.1.1-5	1. 0 – trop	N/A
SRDO3.2.1.1.1.1-6	2. trop – 25 km	3 km
SRDO3.2.1.1.1.1-7	3. 25 – 60 km	3 km
SRDO3.2.1.1.1.1-9	Vertical reporting interval	Vertical Cell Size
SRDO3.2.1.1.1.1-10	Horizontal Coverage	SZA ≤ 80 degrees
SRDO3.2.1.1.1.1-11	Vertical Coverage	trop – 60 km
	Measurement Range	
SRDO3.2.1.1.1.1-13	1. 0 – trop	N/A
SRDO3.2.1.1.1.1-14	2. trop – 60 km	0.1 – 15 ppmv
	Measurement Accuracy	
SRDO3.2.1.1.1.1-16	1. 0 – trop	N/A
SRDO3.2.1.1.1.1-17	2. trop – 15 km	20% or 0.1 ppmv
SRDO3.2.1.1.1.1-18	3. 15 – 60 km	10% or 0.1 ppmv
	Measurement Precision	
SRDO3.2.1.1.1.1-20	1. 0 – trop	N/A
SRDO3.2.1.1.1.1-21	2. trop – 15 km	10%
SRDO3.2.1.1.1.1-22	3. 15 – 50 km	3%
SRDO3.2.1.1.1.1-23	5. Profile, 50 – 60 km	10%
SRDO3.2.1.1.1.1-25	Long term stability	2%
SRDO3.2.1.1.1.1-27	Mapping uncertainty	25 km
SRDO3.2.1.1.1.1-29	Mapping local average revisit time	4 days
SRDO3.2.1.1.1.1-31	Maximum local refresh	N/A

6.2 Additional Data Products

Table 6.2-1 specifies the additional output products that are not part of our baseline but are available from the UV/visible limb algorithm.

Table 6.2-1. Additional, non-baseline data products available from the UV/visible limb retrieval algorithm.

Data	Units	Reference
Cloud fraction	$0.0 < f_{\text{cld}} < 1.0$	Section 2.4.8.5
Cloud top pressure	Atmospheres	Section 2.4.8.4
Visible surface reflectivity	Percent	Section 2.4.8.1
Aerosol profile	Scattering coefficient	Section 2.4.10
Neutral number density	cm^{-3}	Section 2.4.9

6.3 EDR Content

The output records of the Limb Profile Ozone EDRs will include the information listed in Table 6.1-1 and Table 6.2-1. (The additional, non-baseline data products are flagged as bold-italicized parameters) This data is organized into a header record followed by a number of science data records. The recommended content of these records follows:

Header record with

- EDR identification
- Spacecraft identification
- Sensor identification
- Date and time of EDR generation
- Date and start time of data in file
- Date and end time of data in file

Data records (approximately 240 per orbit) with

- Orbit Number
- Date and time of data
- Data acquisition orbit number
- Data transmission orbit number
- Ascending Node Julian date and time tag
- Spacecraft altitude
- Identification of SDR calibration parameters
- EDR Algorithm identification number
- EDR Algorithm version number
- Tropopause height
- Number of 3 km layers (N_L) from 0 to 60 km (max 20)
- Normalization height
- Radiance at normalization height
- For each of the N_L layers
 - Latitude
 - Longitude
 - Solar zenith angle
 - Satellite zenith angle
 - Azimuth angle (the angle between the sun and the satellite IFOV)
 - Normalized radiance
 - Layer ozone (number density & volume mixing ratio)
 - Residue (difference between measured and modeled normalized radiance)
 - Integrated stratospheric ozone
 - ***Cloud fraction***
 - ***Cloud height***
 - ***Surface reflectance***
 - ***Neutral number density***
 - ***Aerosol scattering coefficient***
 - ***Data quality flags***

7. System Accuracy and Precision

System accuracy and precision is determined by the sensor performance, by the algorithm sensitivities to parameter uncertainties, by basic atmospheric variability, and by the uncertainty in the spacecraft pointing knowledge.

7.1 Profile Accuracy

The system accuracy for the profile EDR is allocated among the limb sensor, the algorithm, and the alignment and attitude quality of the spacecraft and sensor. The allocations are made for three altitude regions. In the regions of the tropopause to 15 km and 15 to 28 km, visible wavelengths are used for retrievals and the accuracy requirements are 20% and 10%, respectively, with a 0.1 ppmv floor in both regions. In the altitude region between 28 and 60 km, UV wavelengths are used, and the accuracy requirement is the greater of 10% and 0.1 ppmv. The allocated accuracy errors for the sensor and the algorithm are shown in **Figure 7.1-1**.

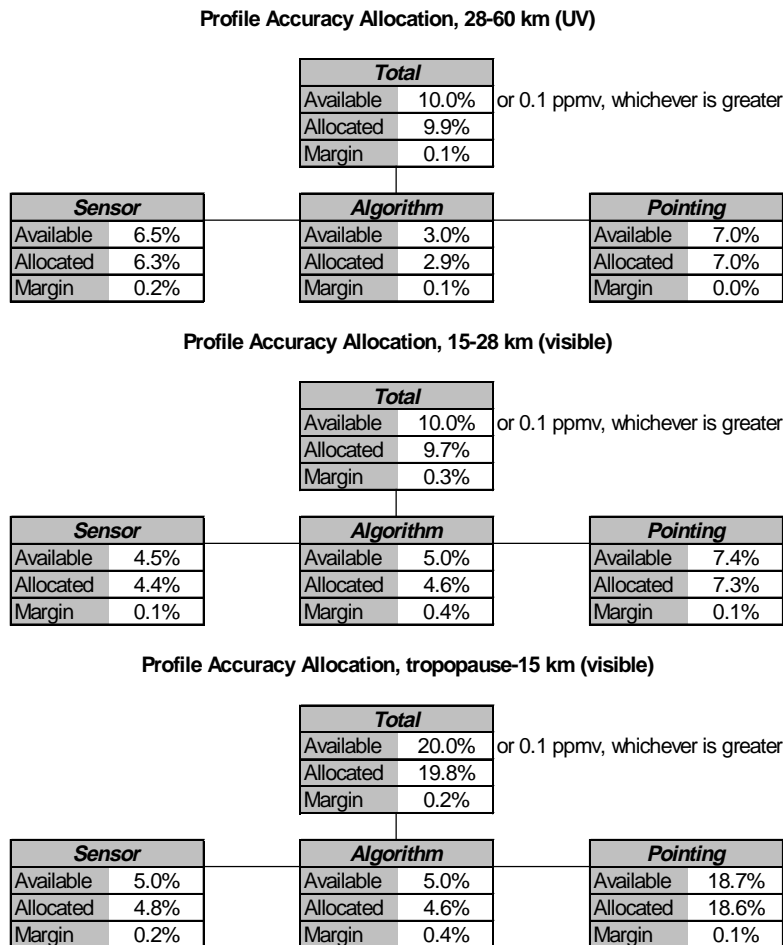
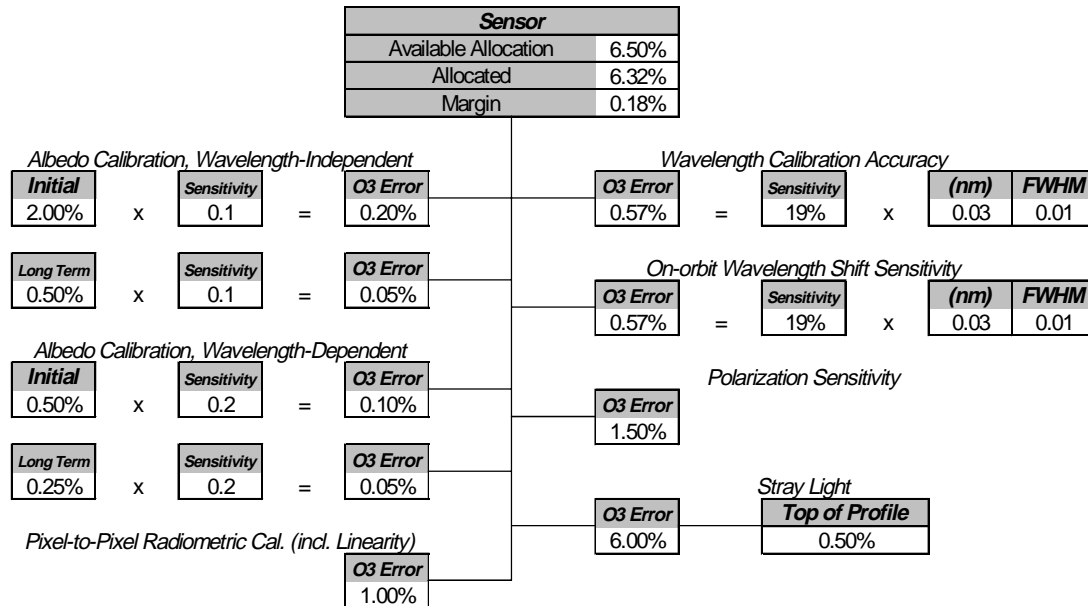


Figure 7.1-1. The error trees show the allocated accuracy errors for the sensor and the algorithm for the 3 altitude regions covering the required profiling range.

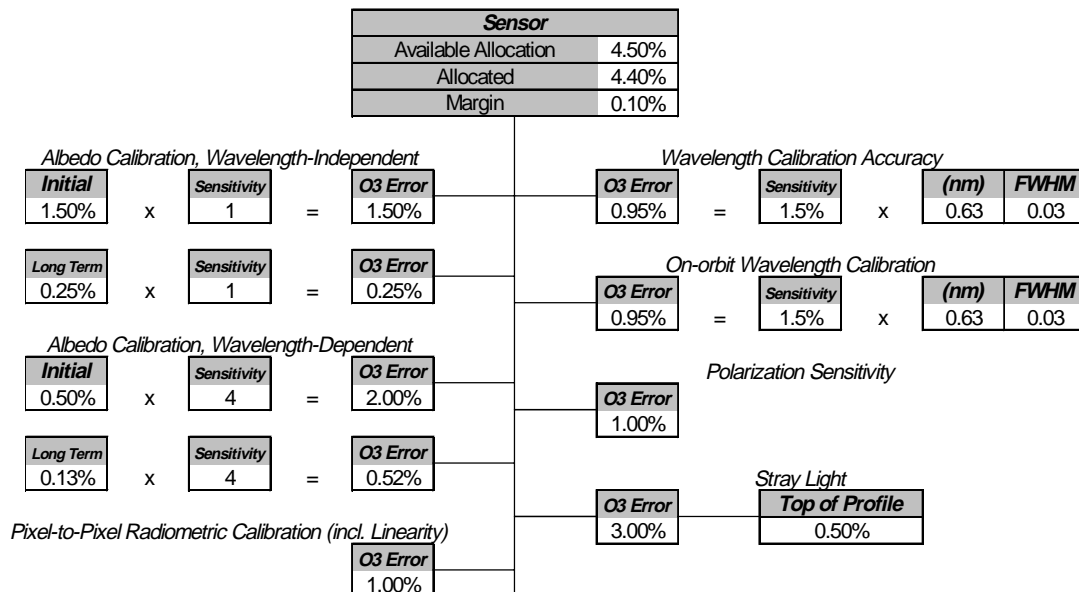
7.1.1 Sensor Accuracy Allocations

The factors affecting the accuracy of the sensor measurements come from calibration errors (radiometric and wavelength) and from instrument effects such as polarization sensitivity and stray light levels. The allocated errors for the sensor are given in **Figure 7.1-2**.

Profile Accuracy Allocation, Sensor, 28-60 km (UV)



Profile Accuracy Allocation, Sensor, 15-28 km (visible)



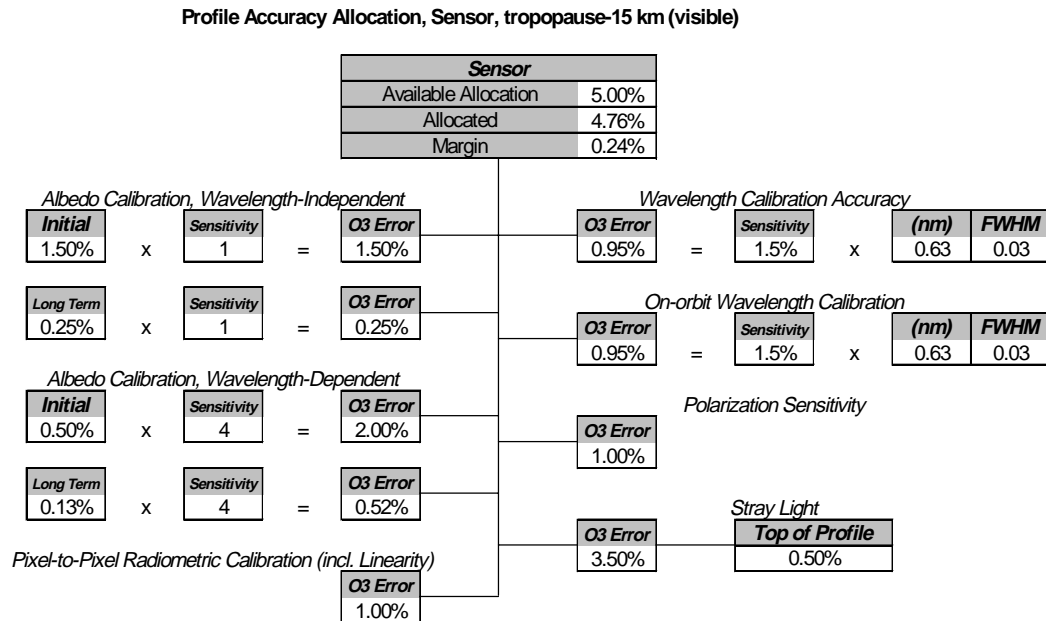


Figure 7.1-2. The error trees show the factors affecting the ozone measurement due to sensor effects and the allocated size of the error in the ozone retrieval .

Albedo Calibration, Wavelength-Independent and Wavelength-Dependent: Although the limb algorithm is basically self-calibrating through normalization of the radiance at each altitude to the radiance at the top of the atmosphere (>60 km), there is a small residual sensitivity to the reflectance of the underlying surface (including clouds). This measurement requires an albedo measurement. The sensitivity to wavelength calibration errors was derived by simulation and is summarized in ICSR E8092901 (29 Sep 98). The uncertainties are given in **Table 7.1-1**.

Table 7.1-1. Contribution of limb albedo calibration accuracy to ozone concentration accuracy. The bold numbers are used in the allocations.

	Test input	O ₃ change	Sensitivity conc/input	Current initial capability	Current long-term capability	O ₃ uncertainty ¹
UV λ-independent	1% radiance	<0.1%	0.1	2%	0.5%	0.21%
UV λ-dependent	0.5% inter-λ	<0.1%	0.2	0.5%	0.25%	0.11%
UV RSS						0.24%
VIS λ-independent	1% radiance	1%	1	1.5%	0.25%	1.52%
VIS λ-dependent	0.5% inter-λ	2%	4	0.5%	0.13%	2.07%
VIS RSS						2.6%

¹ RSS of initial and long term contributions

Pixel-to-pixel Radiometric Calibration (incl. Linearity and Offsets): This contribution includes the uncertainty of flat-fielding and system linearity calibrations (i.e., the residual nonlinearity after linearity calibration), not the actual linearity of the system itself.

Wavelength Calibration Accuracy and On-Orbit Wavelength Shift Sensitivity: We allocate initial wavelength calibration accuracy and a sensitivity to shifts on orbit. The supporting analysis has two parts: the expected shift sensitivity, and the ozone error due to such shifts.

The expected shift sensitivity is shown in Figure 3.1-3. This analysis is fairly conservative because it does not account for correlations in the shift between wavelengths. The expected performance assumes a 0.1% irradiance error, which is reasonable based on experience with TOMS Earth Probe calibrations, which used 1-week extrapolations based on the preceding 10 weeks of data (See ICSR E8110501, 5 Nov 98).

Because of the wavelength-dependent dispersion of the prism, it is sensible to specify wavelength calibration accuracy in terms of a fraction of the resolution FWHM. The allocation based on these results is 0.01 FWHM for UV, 0.03 FWHM for the visible, and 0.1 FWHM for the 1 micron channel. The accuracy for the 16 wavelength channels is shown in **Table 7.1-2**. Earlier allocations (presented at the November 98 TIM), gave too conservative numbers in the UV while the visible allocation was more of a mean than a worst case.

The ozone sensitivity to wavelength shifts is derived from shift sensitivity analysis shown in **Figure 7.1-3** for the UV and visible wavelengths used in limb retrievals. The sensitivity accounts for the spectral resolution of the sensor. Based on this analysis, we have used a sensitivity of 19% per nm for the UV and 1.5% per nm for the visible.

Table 7.1-2. Wavelength accuracy allocation based on simulation results shown in Figure 3.1-4.

Channel w.l. (nm)	FWHM (nm)	Expected accuracy		Allocated accuracy	
		nm	FWHM	nm	FWHM
290	1.5	0.0053	0.0035	0.0150	0.0100
293	1.5	0.0053	0.0035	0.0150	0.0100
296	1.75	0.0061	0.0035	0.0175	0.0100
299	1.75	0.0061	0.0035	0.0175	0.0100
302	2	0.0070	0.0035	0.0200	0.0100
310	2	0.0070	0.0035	0.0200	0.0100
320	2.5	0.0088	0.0035	0.0250	0.0100
350	3	0.0105	0.0035	0.0300	0.0100
352.5	3	0.0105	0.0035	0.0300	0.0100
400	5	0.0175	0.0035	0.0500	0.0100
500	9	0.0900	0.0100	0.2700	0.0300
525	11	0.1100	0.0100	0.3300	0.0300
575	14	0.2800	0.0200	0.4200	0.0300
602	16	0.4800	0.0300	0.4800	0.0300
675	21	0.6300	0.0300	0.6300	0.0300
1000	40	4.0000	0.1000	4.0000	0.1000

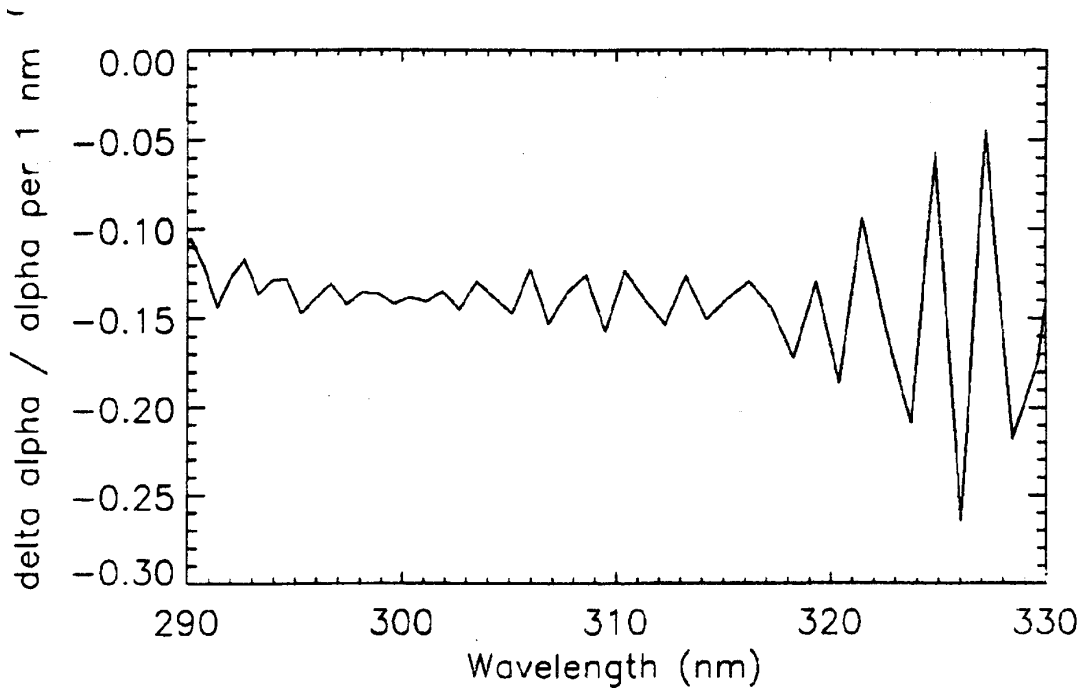


Figure 7.1-3 (a)

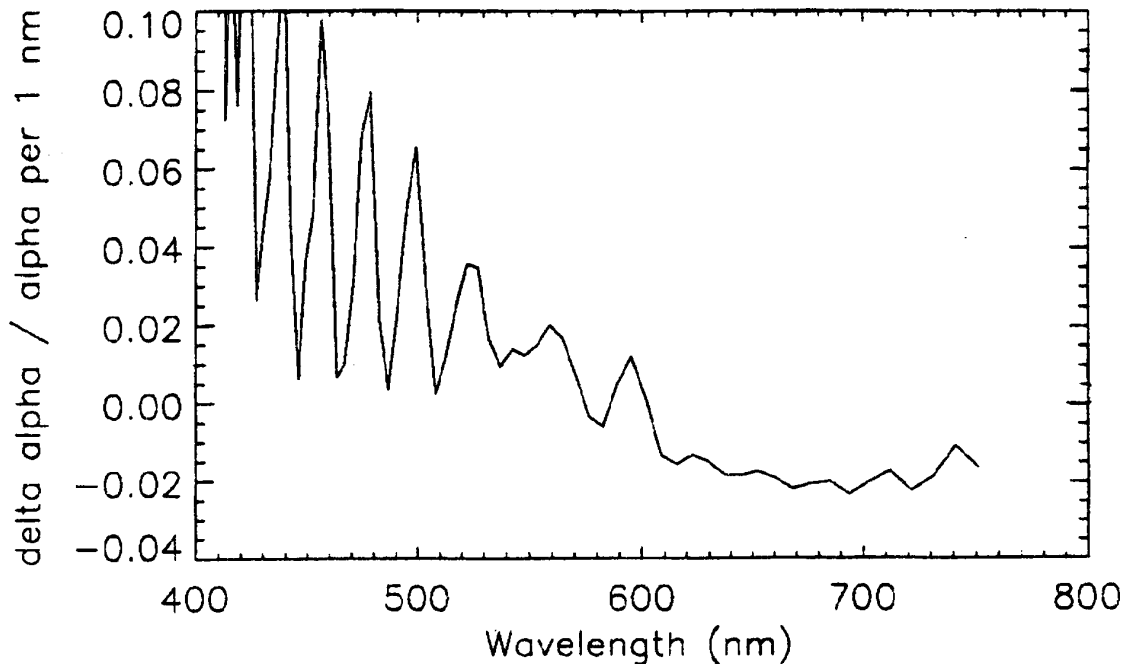


Figure 7.1-3 (b)

Figure 7.1-3. Normalized ozone absorption coefficient shift sensitivity for a 1 nm wavelength shift for (a) UV and (b) visible wavelengths.

Polarization Sensitivity: Polarization of backscattered radiation poses a particular problem in the UV where Rayleigh scattering cross sections are high. Reflective surfaces in the sensor can enhance incident radiation of one polarization state more than the other. This in itself is not a problem, except that the

relative amplitudes of the S and P polarized light will vary with viewing conditions. The result of the difference in sensor throughput for the two polarizations would be cross-track and latitude dependences in the retrieved ozone amounts, and biases at lower altitudes. BUV sensors typically use depolarizers in the fore-optics to reduce the polarization sensitivity of the sensor to acceptable levels. The limb sensor is designed with a depolarizer at its entrance aperture. The expected linear polarization sensitivity of the sensor is less than 0.2%, with the allocated performance being 1% (PDR, p. 368).

Any effect from polarization sensitivity is due to a difference in polarization of the light coming from the observed altitude and the normalization altitude. The UV profile retrievals benefit from fairly uniform polarization through the altitude range of interest (as seen in **Figure 7.1-4a** and from both altitude and 350 nm normalizations. The uncertainties in the visible retrievals are greater due to the large variation in the degree of polarization with altitude. For example, 675 nm varies from 65% polarized at 40 km down to 28% polarized at 20 km (**Figure 7.1-4b**). This 37% difference is reduced by the allocated 1% polarization performance of the limb sensor to 0.37.

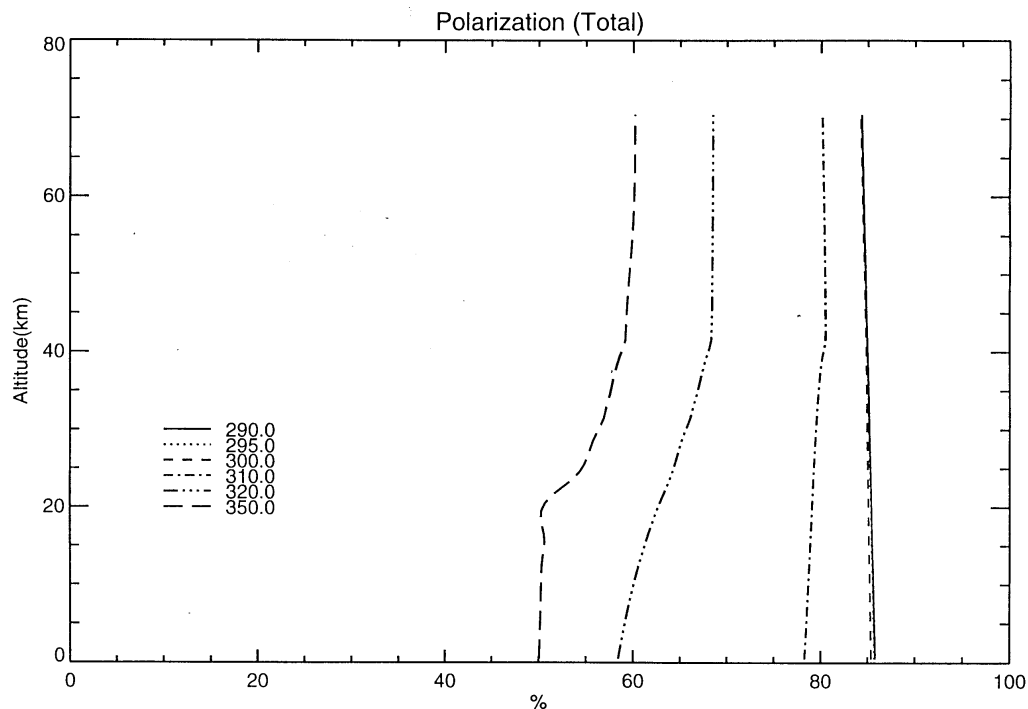


Figure 7.1-4 (a)

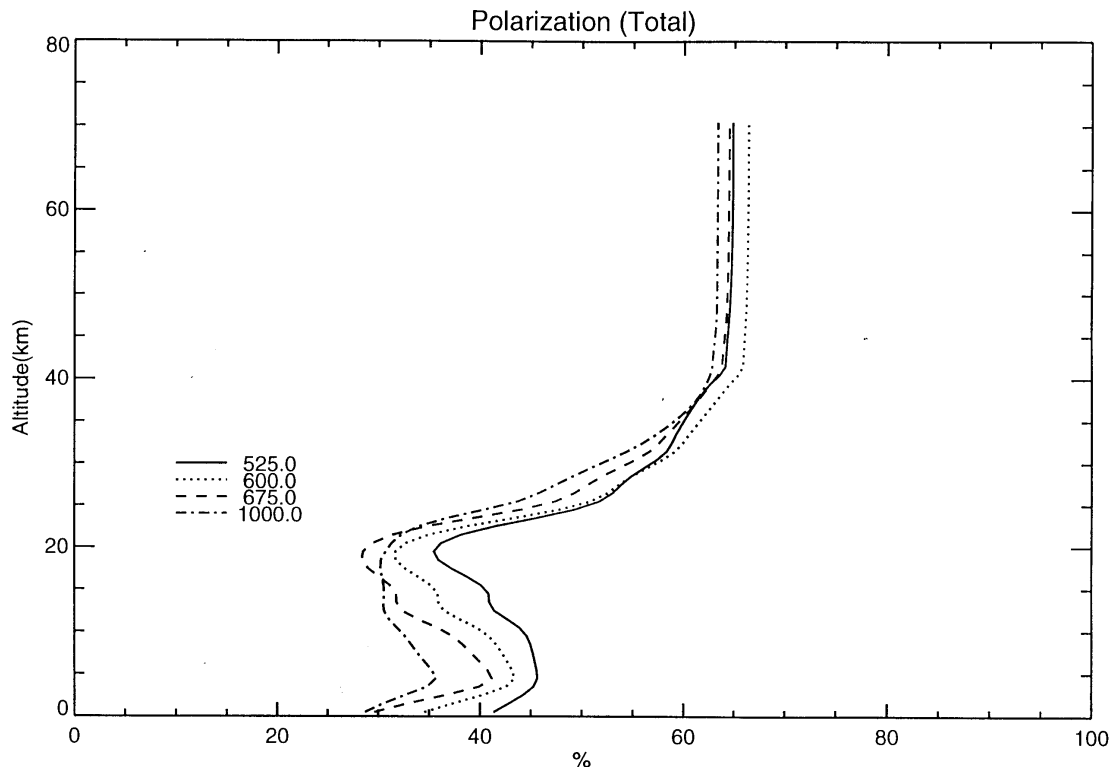


Figure 7.14(b)

Figure 7.1-4. Scene polarization as a function of altitude for various wavelengths used in the limb retrievals.

Stray Light: Because the algorithm normalizes profiles with radiance measured at the top of the atmosphere, the retrieval is particularly sensitive to stray light biasing the normalization radiance. The stray light allocation is based on the effect of stray light at the top of the profile. The benchmark is the 300 nm radiance at 61.5 km (expected to represent the minimum measured radiance). Based on Monte Carlo simulations, we allocate an altitude dependent error in the ozone retrieval due to stray light at the top of the profile. The altitude dependence of this error is shown in **Figure 7.1-5**. (This analysis is described in ICSR E8120801, 8 Dec 98.)

Channels(bw) Rectangular
290(1.5) 295(1.5) 300(1.5) 310(1.5) 320(1.5)
525(13.) 600(13.) 675(13.)
400 sec Integration Time, Normalization at 61.5km, 10 noise sets
1km layers, with Multiple Scattering
Aerosol, June 23,1993 30.2N, Aged Volcanic
Stray Lite .005
290,295,300,310,320 ratioed to 350

SZA_{obs}=40.0 ϕ_{obs} = 0.0 ρ_{srfc} = 0.1 Z_{obs}=833.0

M325 Ozone
P&T US76

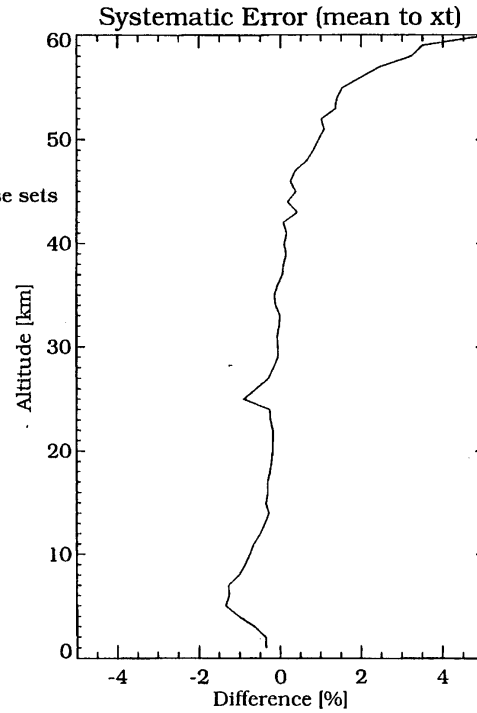
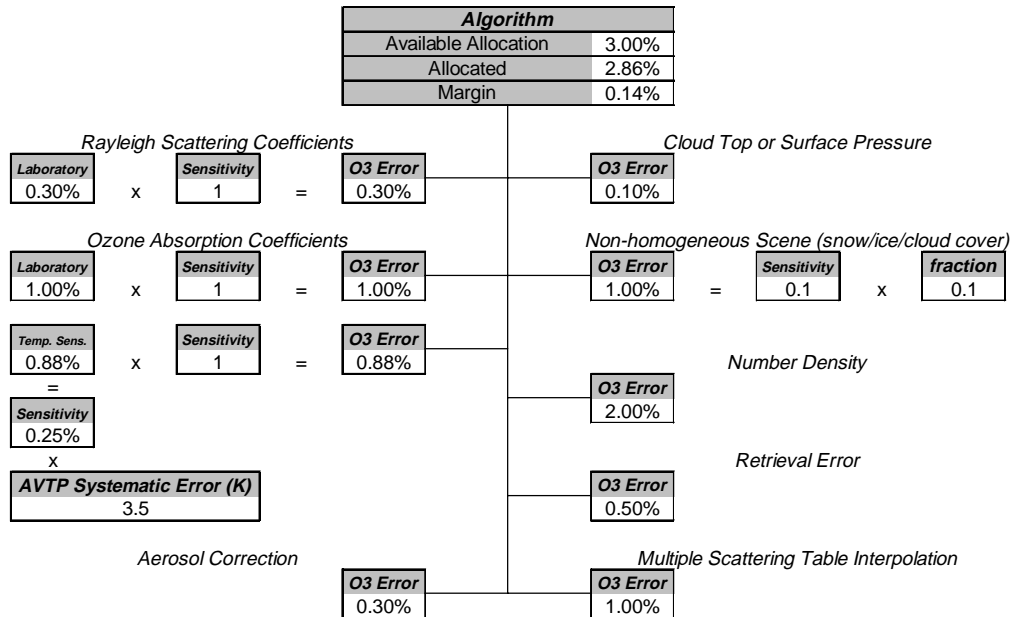


Figure 7.1-5. Systematic error as a function of altitude due to 0.5% stray light at 61.5 km.

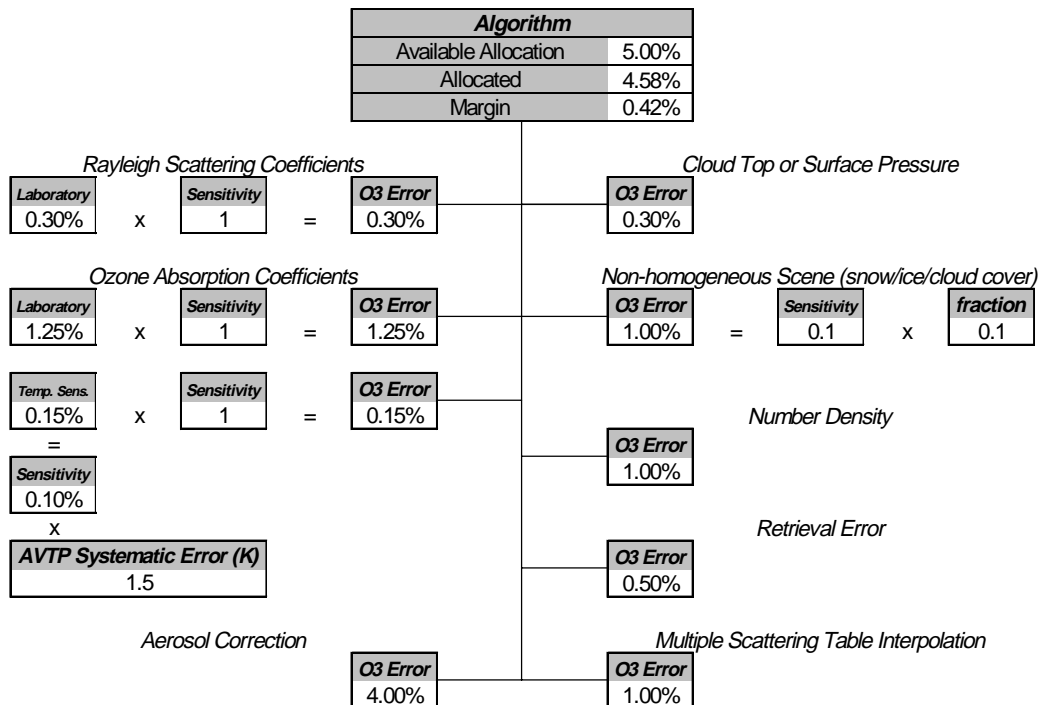
7.1.2 Algorithm Accuracy Allocations

The uncertainties affecting the accuracy of the algorithm's retrieval enter through coefficient uncertainties, table interpolations, surface reflectivities, and the accuracy of the number density and aerosol retrievals. The allocated values of these errors are shown in **Figure 7.1-6**.

Profile Accuracy Allocation, Algorithm, 28-60 km (UV)



Profile Accuracy Allocation, Algorithm, 15-28 km (visible)



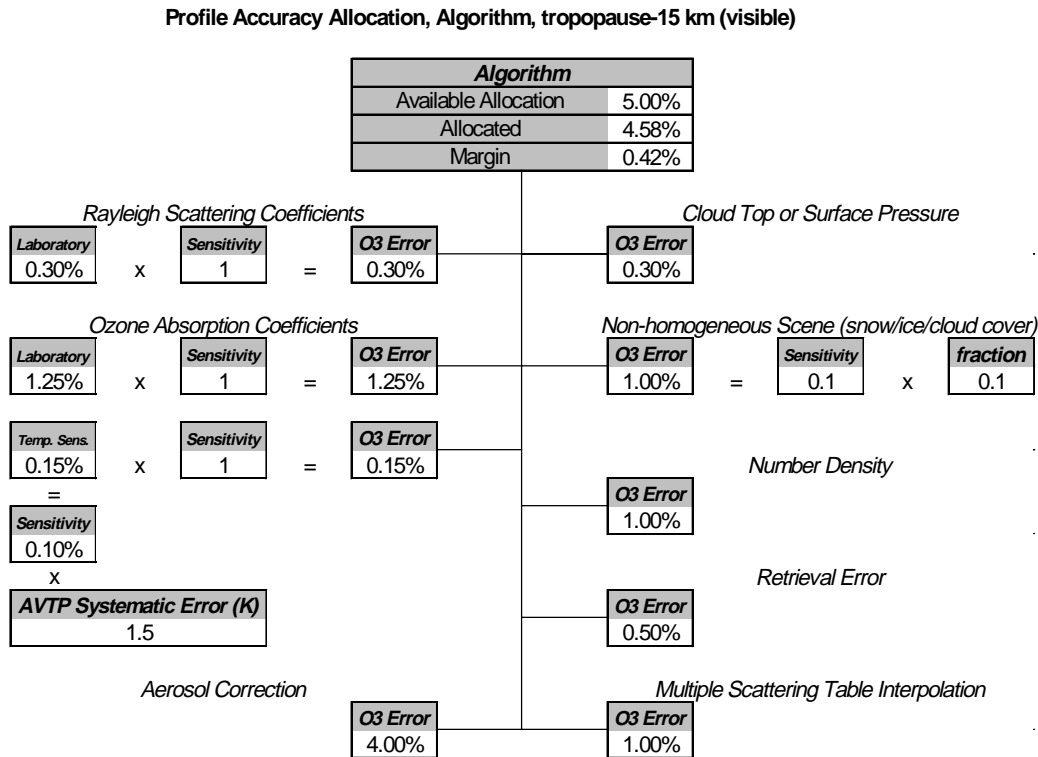


Figure 7.1-6. Errors affecting the accuracy of the algorithm’s ozone retrieval are listed along with the allocated values for the three altitude ranges covered by the limb profiler.

Rayleigh Scattering Coefficients: We allocate the 0.3% accuracy given by Fleig et al. (1990, Table 7.2).

Ozone Absorption Coefficients, Absolute: We estimate the ozone absorption coefficient error in the visible Chappuis band to be 1.25%, based on recent measurements by Anderson and Mauersberger [1992] and Burkholder and Talukdar [1994]. (There is a 1% uncertainty with respect to the reference wavelengths and <1% uncertainty in the reference values.) As with the total column, we allocate 1.0% in the UV based on analysis comparing Bass-Paur and more recent measurements of ozone absorption coefficients.

Ozone Absorption Coefficients, Temperature Dependence: Based on simulations, we estimate a 0.25% error for every 1 K temperature systematic error at altitudes greater than 28 km—the region where UV wavelengths are used for ozone inversions. The sensitivity is much lower in the visible since the ozone absorption coefficients in the Chappuis band are temperature insensitive.

The external AVTP EDR has its error specified as “uncertainty,” which, in the limiting case, is the RSS of precision and accuracy. Since the uncertainty in AVTP from CrIS and CMIS will not be parsed into precision and accuracy, we assume a worst case situation in which the uncertainty is entirely precision or entirely accuracy and account for the worst case in both precision and accuracy error allocations. The systematic error resulting from this assumption is likely an overestimate because most of the AVTP uncertainty is expected to be random.

Aerosol Correction: The aerosol correction allocations below 28 km are based on the use of the Chappuis triplet formulation to determine the spectral dependence of the aerosol extinction by interpolation, and on the retrieval of aerosol profiles using the visible and near-infrared channels (400-1000 nm). We have allocated 4% for the tropopause-20 km region, and 2% for the 20-28 km region based on simulations of the triplet correction with and without knowledge of the aerosol profile.

Above 28 km, the allocation based on simulations is small (0.3%) because the UV wavelengths are relatively insensitive to aerosol scattering due to the dominance of Rayleigh scattering.

Cloud Top or Surface Pressure: The error due to cloud top pressure uncertainties is much smaller for limb radiances than for nadir radiances. The 0.1% allocation (here and in the precision budget) is based on estimates of the pressure sensitivity based on the uncertainty in cloud top pressure measurements using a 1.0 km vertical resolution sensor at a wavelength of 1000 nm.

Non-homogeneous Scene: The error in profile ozone due to non-homogeneous reflecting surfaces is reduced by use of a partial cloud model based on area-weighted averages of cloudy and clear scene radiances. The allocation assumes the 0.1 fractional uncertainty of the external cloud cover EDR. The algorithm minimizes the influence of surface reflectance uncertainties through a radiance normalization using the radiance at 61 km. As shown by Flittner et al. [1998b], 0.1 fractional change in the surface albedo corresponds to less than 1% change in the normalized 600 nm radiance at 20 km. Thus we estimate about a 0.1 sensitivity for a cloud cover uncertainty of 0.1 (for all wavelengths).

Number Density: We allocated neutral number density (NND) systematic error based on the accuracy of the external AVTP EDR. We allocated a 0.5% NND error for a 1 K AVTP error (which actually yields a 0.37% NND error). This results in a 0.75% (1.75%) error for a 1.5 K (3.5 K) temperature error. Consequently, we allocate 1% for retrievals lower than 28 km and 2% for retrievals above 28 km (See the SFR, p. 136).

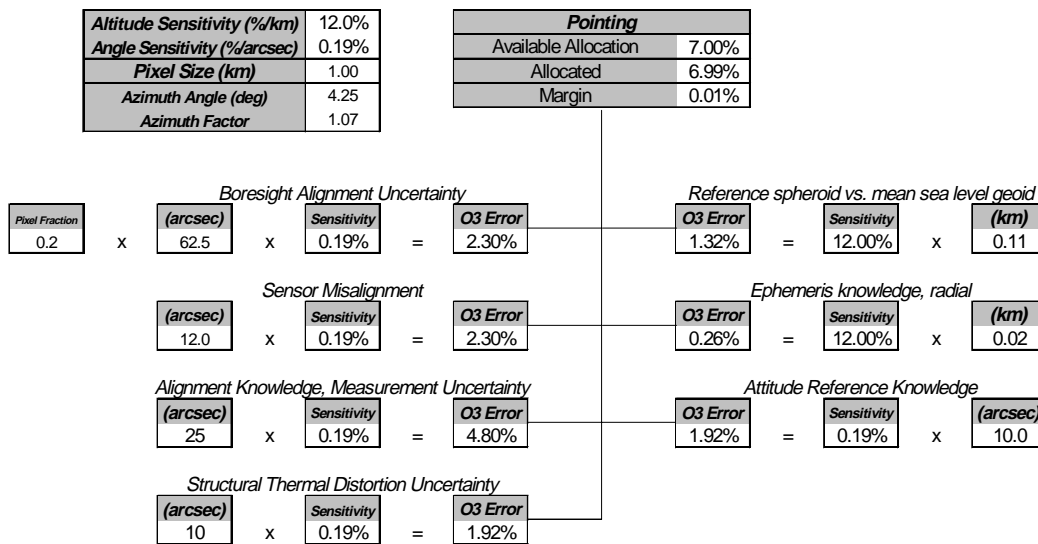
Retrieval Error: The retrieval systematic error allocation of 0.5% is based on the small systematic error appearing in the Monte Carlo simulations of random errors.

Multiple Scattering Table Interpolation: This allocation accounts for the use of pre-computed tables for the multiple scattering calculation. The tables are constructed using atmospheres that differ from the actual atmosphere. The dependence of multiple scattering on the scene albedo is largely removed through the radiance normalization using a reference altitude radiance.

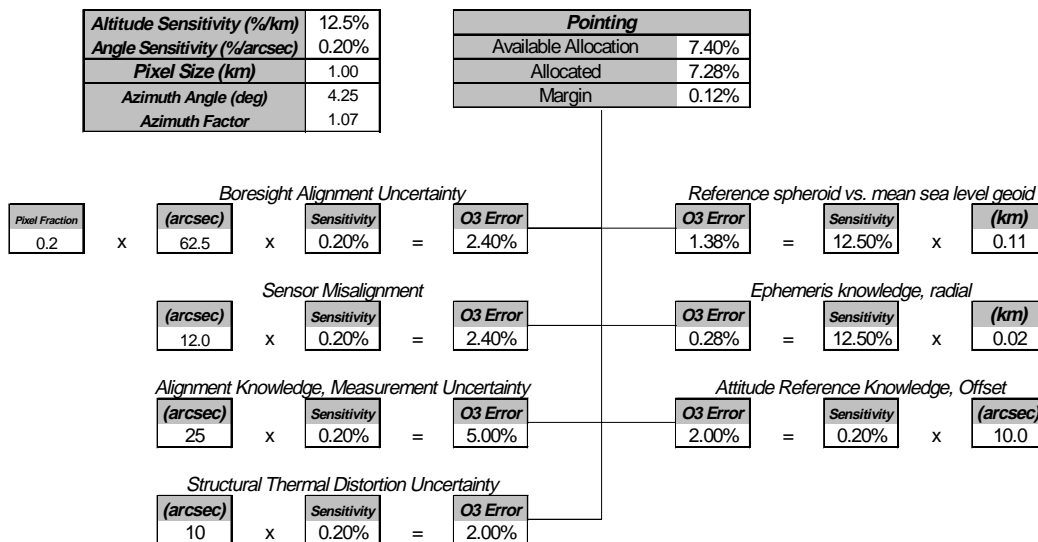
7.1.3 Pointing Accuracy Allocations

The components of the pointing allocation are based on the sensor and spacecraft specifications. The difference in allocated errors for the altitude ranges comes from the differences in the maximum vertical gradient in ozone volume mixing ratio in the three altitude ranges. If the sensitivity of the measured ozone to altitude registration errors (the altitude sensitivity) is exceeded due to a large vertical ozone gradient, it may be accommodated by the 0.1 ppmv accuracy floor which is not explicit in these allocation trees. The allocations shown in **Figure 7.1-7** are based on analysis presented in ICSR E8121802 (18 Dec 98).

Profile Accuracy Allocation, Pointing, 28-60 km (UV)



Profile Accuracy Allocation, Pointing, 15-28 km (vis)



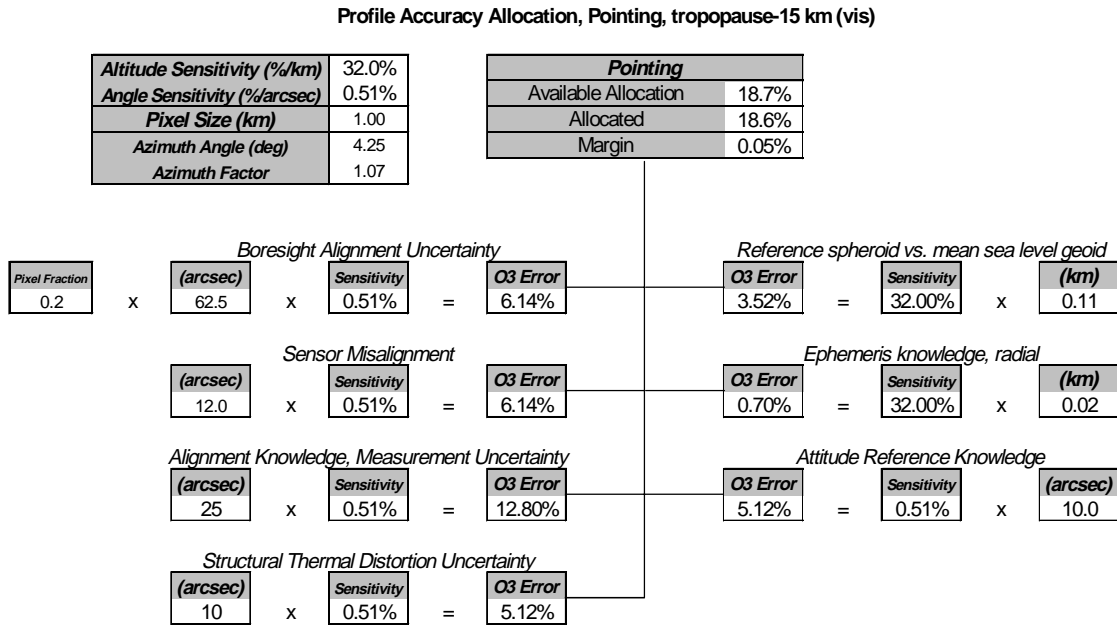


Figure 7.1-7. Error allocation tables for altitude registration (pointing) uncertainties.

7.2 Profile Long Term Stability

Long-term stability is primarily a calibration issue. The sensitivity of the ozone profile determination to calibration errors is discussed in Section 7.1.1. As previously discussed, the Limb ozone profile retrieval uses several normalizations to remove sensitivity to calibration errors. These include the solar flux normalization, the altitude normalization, and multiple-channel combinations. The result is a long-term uncertainty much lower than the SRD requirement.

As with the nadir sensor, long-term calibration errors arise from knowing how the Working solar diffuser changes with time. The diffuser monitoring techniques are discussed in Section 3.1.3.

The long term stability allocations are shown in **Figure 7.2-1**. The sensitivities used here are for the visible wavelengths; the UV sensitivities are an order-of-magnitude lower. The calibration uncertainties assume weekly working diffuser deployment and semi-annual reference diffuser deployment. For details of analysis, see ICSRs E8110501 (5 Nov 98) and E8092901 (29 Sep 98).

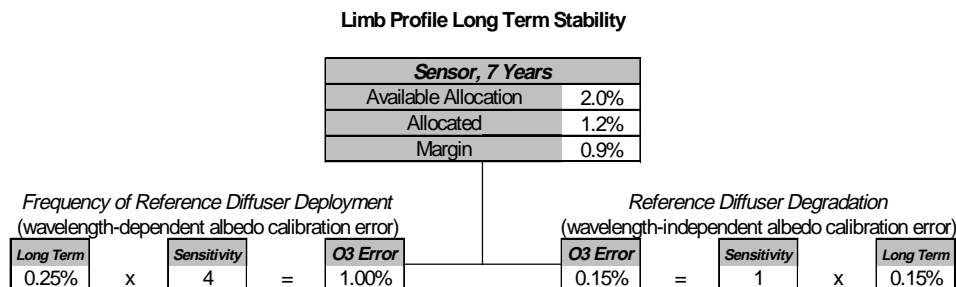


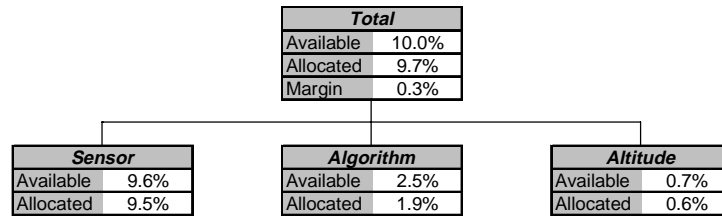
Figure 7.2-1. Allocation of errors affecting long-term stability of the sensor.

We intend to correct for Working diffuser degradation on the Limb sensor. Though the profile retrieval algorithm is mostly self-calibrating, there is a residual ozone sensitivity through the uncertainties in the calculation of surface reflectances. The sensitivity is largest at visible wavelengths (see ICSR E8092901). Similar to the total column case, profile retrievals are more sensitive to wavelength-dependent errors than wavelength-independent errors. But errors which are only linear in wavelength will introduce very little ozone error. The spectral dependence of degradation at visible wavelengths is even less than observed in the ultraviolet (Hilsenrath, *ibid.*), so these errors are not expected to contribute significantly to retrieval errors. The maximum sensitivity of profile errors to wavelength-independent calibration errors is 1:1. We anticipate total wavelength-independent degradation of the Reference diffuser to be less than 0.2%. This value, for which we have assumed no correction, is combined with the 0.25% diffuser monitoring uncertainty to yield the long-term profile ozone uncertainty.

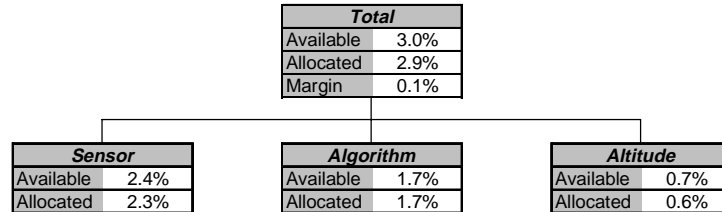
7.3 Profile Precision

The precision of the ozone profile retrievals is determined by random noise in both the sensor and in factors affecting algorithm performance. The system precision for the profile EDR is allocated among the limb sensor, the algorithm, and the altitude registration precision of the profile. The allocations are made for four altitude regions. In the regions tropopause-15 km and 15-28 km, visible wavelengths are used for retrievals and the accuracy requirements are 10% and 3%, respectively. In the regions 28-50 km and 50-60 km, UV wavelengths are used for retrievals and the precision requirements are 3% and 10%, respectively. The total precision allocated for the four altitude regions is shown in **Figure 7.3-1**. At low and high altitudes, sensor noise is the largest factor in the precision error budget. At middle altitudes, the sensor noise and algorithm performance contribute more equally to the total precision.

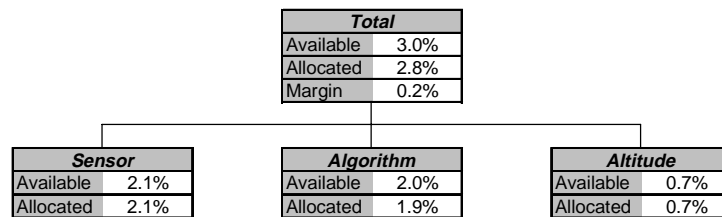
Profile Precision Allocation, 50-60 km (UV)



Profile Precision Allocation, 28-50 km (UV)



Profile Precision Allocation, 15-28 km (visible)



Profile Precision Allocation, tropopause-15 km (visible)

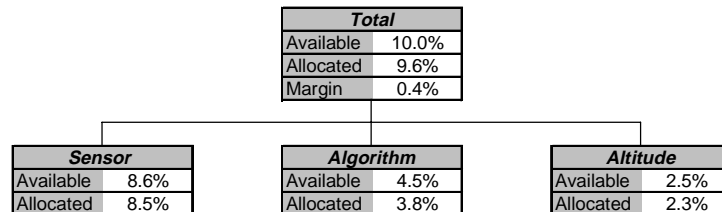


Figure 7.3-1. Allocated ozone precision errors are divided between sensor errors, algorithm errors, and altitude registration.

7.3.1 Sensor Precision Allocations

The major source of uncertainty in the sensor is due to the signal to noise ratio of the limb radiance measurement. The smaller signals used in the high altitude range yield smaller SNRs, driving the scatter of the retrieved ozone values higher. A smaller additional term comes from the uncertainty in the solar irradiance measurement used in finding the albedo. The solar uncertainty comes largely from uncertainty in the goniometric calibration of the solar diffuser.

The radiance SNR requirements derived from this allocation are given in **Table 7.3-1**.

At a given altitude, the effective SNR for the normalized radiance is given by the combination of either, in the UV, two wavelengths and two altitudes, or, in the visible, three wavelengths and two altitudes. One of the altitudes is the normalization altitude at the top of the profile.

For the UV case, the total variance is given by

$$\sigma^2(\lambda, h) = \frac{1}{SNR^2(\lambda, h)} + \frac{1}{SNR^2(350nm, h)} + \frac{1}{SNR^2(\lambda, h_{norm})} + \frac{1}{SNR^2(350nm, h_{norm})}$$

and in the visible, for the Chappuis triplet,

$$\sigma^2(\lambda, h) = \frac{1}{SNR^2(600, h)} + \frac{0.25}{SNR^2(525nm, h)} + \frac{0.25}{SNR^2(675nm, h)} + \frac{1}{SNR^2(600, h_{norm})} + \frac{0.25}{SNR^2(525nm, h_{norm})} + \frac{0.25}{SNR^2(675nm, h_{norm})}$$

Table 7.3-1. Signal-to-noise ratio allocations to the limb sensor channels as a function of wavelength and altitude.

	290 nm	293 nm	296 nm	299 nm	302 nm	310 nm	320 nm	350 nm
Reference	135	135	225	225	225	235	220	370
53-60 km	270	270	n/a	n/a	n/a	n/a	n/a	740
50-53 km	270	270	780	780	780	n/a	n/a	1050
47-50 km	n/a	n/a	780	780	780	n/a	n/a	1050
45-47 km	n/a	n/a	n/a	780	780	n/a	n/a	1050
43-45 km	n/a	n/a	n/a	780	780	950	n/a	1920
38-43 km	n/a	n/a	n/a	n/a	n/a	950	n/a	1920
28-38 km	n/a	n/a	n/a	n/a	n/a	n/a	1390	2530
15-28 km	n/a	n/a	n/a	n/a	n/a	n/a	n/a	TBD
trop-15 km	n/a	n/a	n/a	n/a	n/a	n/a	n/a	n/a

trop = tropopause, 8-15 km depending on
reference = 61-65 altitude

	400 nm	500 nm	525 nm	575 nm	600 nm	675 nm	1000 nm
Reference	n/a	1285	1285	1285	1285	1285	n/a
53-60 km	TBD	n/a	n/a	n/a	n/a	n/a	n/a
50-53 km	TBD	n/a	n/a	n/a	n/a	n/a	n/a
47-50 km	TBD	n/a	n/a	n/a	n/a	n/a	n/a
45-47 km	TBD	n/a	n/a	n/a	n/a	n/a	n/a
43-45 km	TBD	n/a	n/a	n/a	n/a	n/a	TBD
38-43 km	TBD	n/a	n/a	n/a	n/a	n/a	TBD
28-38 km	TBD	n/a	n/a	n/a	n/a	n/a	TBD
15-28 km	TBD	2570	2570	2570	2570	2570	TBD
trop-15 km	n/a	1220	1220	1220	1220	1220	TBD

trop = tropopause, 8-15 km depending on latitude
reference = 61-65 altitude averaged

Figure 7.3-2 shows the effect of expected and allocated SNRs on the retrievals (using a 20-noise-set Monte Carlo simulation). The allocations include significant margin; below 28 km, where the expected SNRs in the visible channels do not meet the current SNR requirements, the expected random error still falls within the allocated value for most of the altitude range.

Figure 7.3-3 and **Figure 7.3-4** show simulations with expected SNRs for a H575 and a H125 profile, respectively. In the case of the H125 profiles, the SNRs permit the allocation to be met except in the ozone hole where the volume mixing ratio is less than 0.3 ppmv. Such relatively rare conditions are specified as exceptions to our specified precision performance.

M325 Ozone
P&T M325

Channels(bw) Rectangular
290(3.0) 293(3.0) 296(3.0) 299(3.0) 302(4.0)
310(4.0) 320(5.0) 350(6.0)
500(9.) 525(11.) 575(14.) 602(16.) 675(21.)

Normalization@ 61.5km, 20 noise sets, OPT EST
Initial Ozone Profile 125M, A Priori Ozone Profile 275L
1km layers, with Multiple Scattering
Aerosol, May 9,1991, 30.1N, Background Volcanic
Monte Carlo uses allocated and expected sensor SNRs
UV Channels are ratioed to 350 nm channel
VIS Channels are; Pair(575,500nm), Triplet(602,525,675nm)

$SZA_{obs}=40.0$ deg
 $\phi_{obs}= 0.0$ deg
 $\rho_{aer}= 0.1$
 $Z_{obs}=833.0$ km

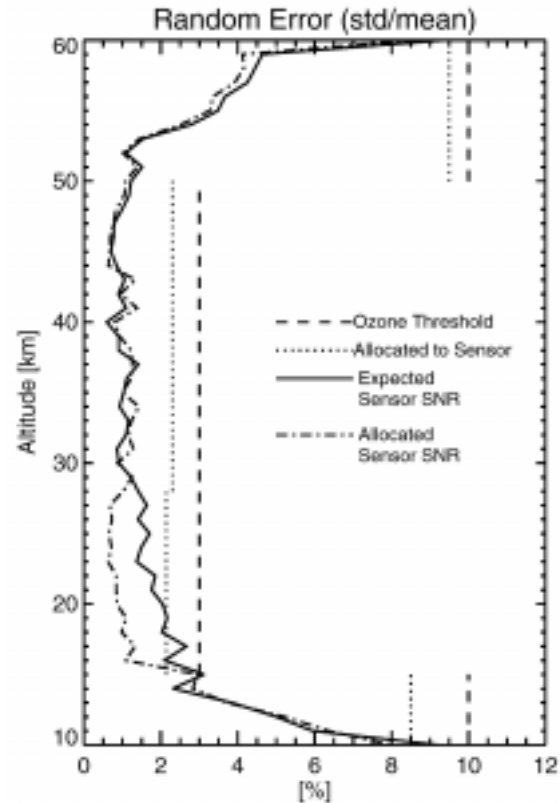


Figure 7.3-2. Precision error for a M325 ozone profile simulated with the expected and allocated limb sensor SNRs.

M575 Ozone
P&T M575

Channels(bw) Rectangular
290(3.0) 293(3.0) 296(3.0) 299(3.0) 302(4.0)
310(4.0) 320(5.0) 350(6.0)
500(9.) 525(11.) 575(14.) 602(16.) 675(21.)

Normalization@ 61.5km, 20 noise sets, OPT EST
Initial Ozone Profile 125M, A Priori Ozone Profile 325M
1km layers, with Multiple Scattering
Aerosol, May 9,1991, 30.1N, Background Volcanic
Monte Carlo uses expected sensor SNRs
UV Channels are ratioed to 350 nm channel
VIS Channels are; Pair(575,500nm), Triplet(602,525,675nm)

$SZA_{obs}=40.0$ deg
 $\phi_{obs}= 0.0$ deg
 $\rho_{aer}= 0.1$
 $Z_{obs}=833.0$ km

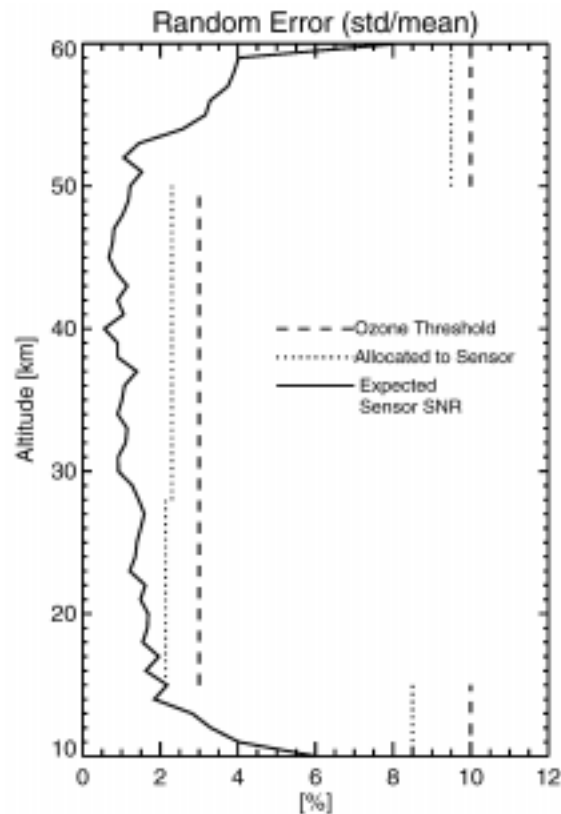


Figure 7.3-3. Precision error for a H575 ozone profile simulated with the expected limb sensor SNRs.

H125 Ozone
P&T H125
Channels(bw) Rectangular
290(3.0) 293(3.0) 296(3.0) 299(3.0) 302(4.0)
310(4.0) 320(5.0) 350(6.0)
500(9.) 525(11.) 575(14.) 602(16.) 675(21.)
Normalization@ 61.5km, 20 noise sets, OPT EST
Initial Ozone Profile 325H, A Priori Ozone Profile 225H
1km layers, with Multiple Scattering
Aerosol, Sept 2, 1991, 60.N, Background Volcanic
Monte Carlo uses expected sensor SNRs
UV Channels are ratioed to 350 nm channel
VIS Channels are; Pair(575,500nm), Triplet(602,525,675nm)
 $SZA_{obs}=40.0$ deg
 $\phi_{obs}=0.0$ deg
 $\rho_{sky}=0.1$
 $Z_{obs}=833.0$ km

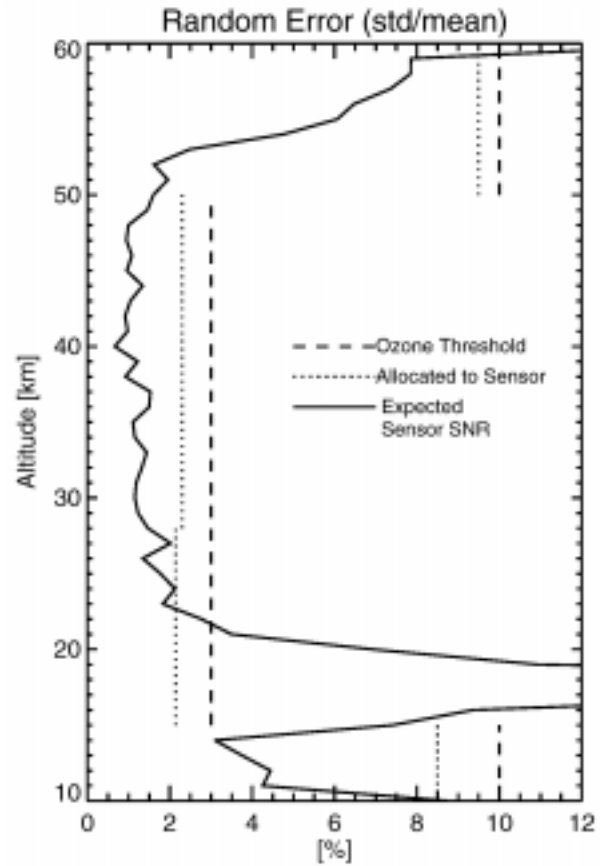
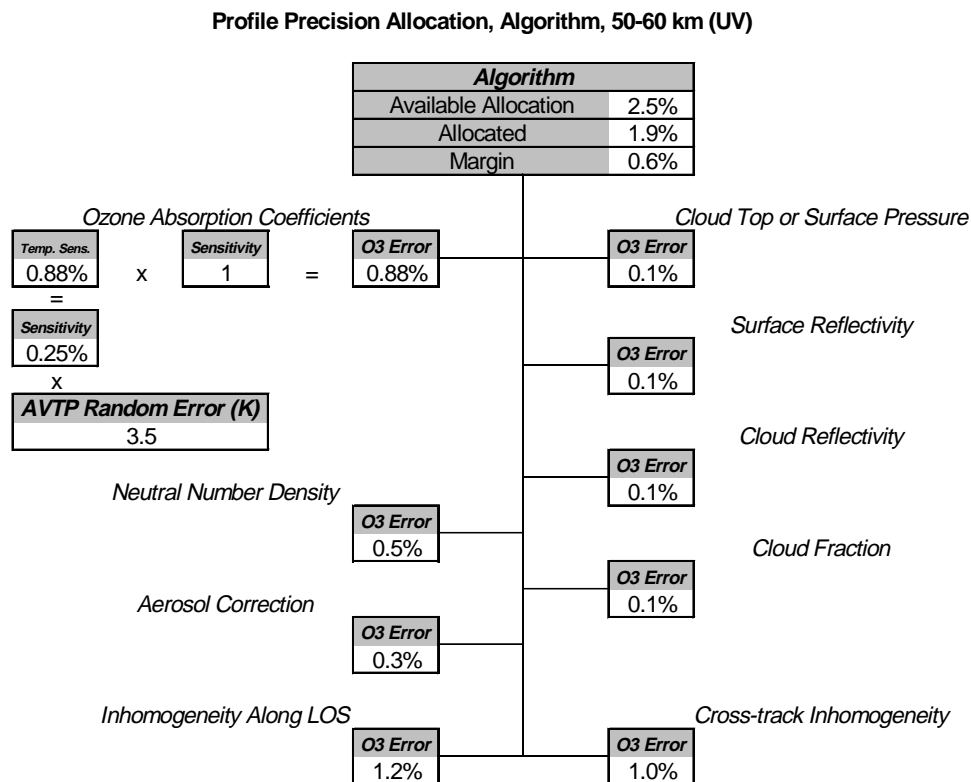


Figure 7.3-4. Precision error for a H125 ozone profile simulated with the expected limb sensor SNRs.

7.3.2 Algorithm Precision Allocations

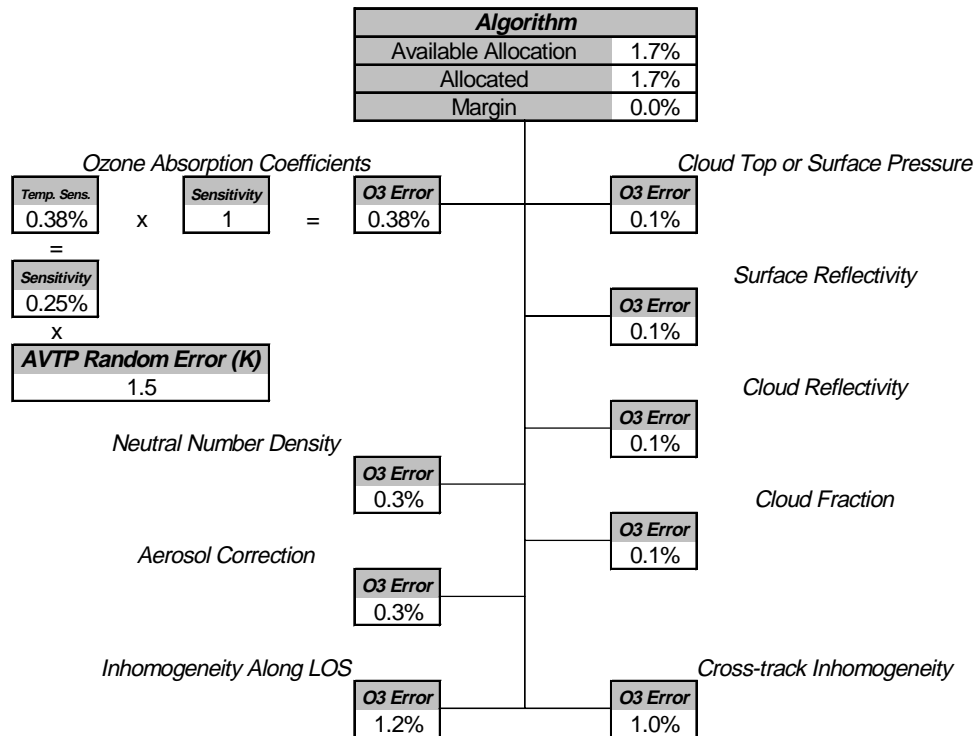
Several atmospheric effects and uncertainties in the model can add noise to the algorithm performance. The dominant factor is inhomogeneity of the atmosphere, both along the line of sight and in the cross track direction (since the cross track cell size is much smaller than the volume it represents). Other factors entering the precision allocation (eg., cloud top or surface pressure, surface reflectivity, cloud reflectivity, cloud fraction, and temperature profile) are constrained through use of other OMPS sensor data, other NPOESS EDRs, or climatology. The limb retrieval includes neutral number density, aerosol corrections, and an altitude normalization (to reduce effects of surface reflectivity uncertainties) to avoid uncertainties inherent in using non-coincident data products.

The algorithm errors affecting the precision of the profile retrieval are listed in error trees (**Figure 7.3-5**) for the four altitude regions defined by the required threshold performance levels. An earlier version of this allocation was described in ICSR E8101301 (13 Oct 98).

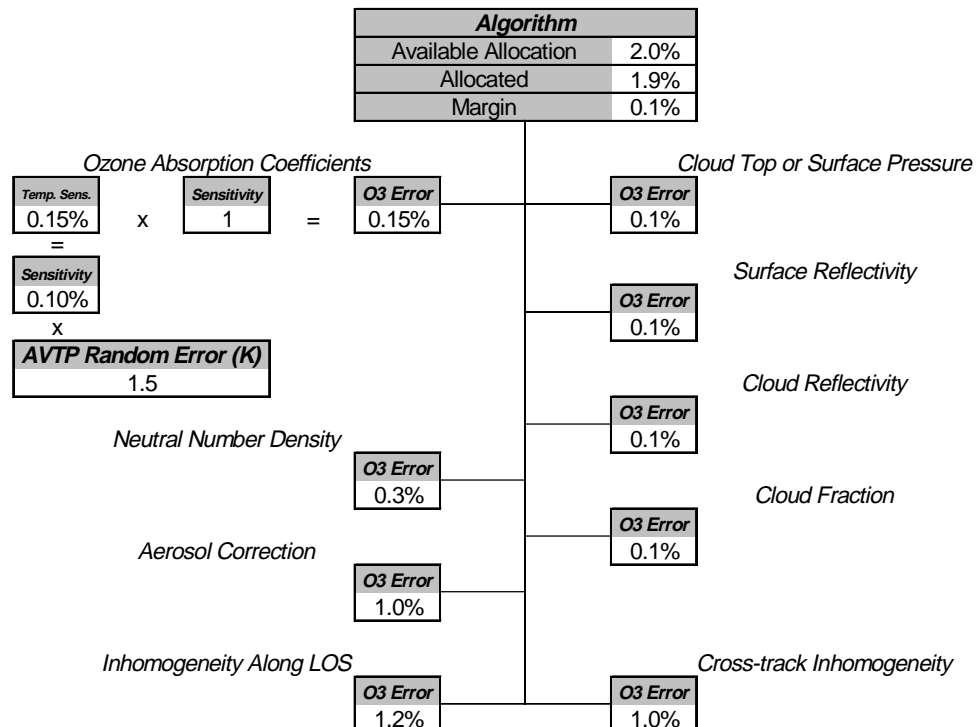




Profile Precision Allocation, Algorithm, 28-50 km (UV)



Profile Precision Allocation, Algorithm, 15-28 km (visible)



Profile Precision Allocation, Algorithm, tropopause-15 km (visible)

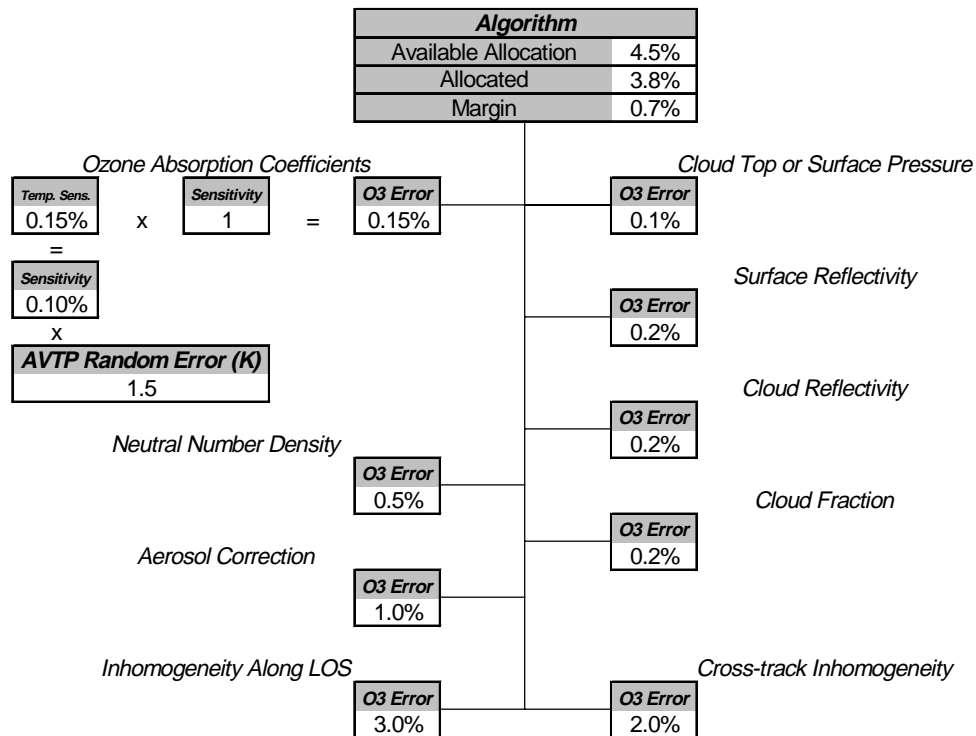


Figure 7.3-5. Error trees for algorithm errors affecting the precision of the ozone retrievals.

Ozone Absorption Coefficients, Temperature Dependence: This error source accounts for uncertainty in the atmospheric temperature as it affects the retrieval through the ozone absorption cross sections. The error is substantially reduced through the altitude ratioing process (normalization).

Based on simulations, we estimate a 0.25% error for every 1 K temperature systematic error at altitudes greater than 28 km where UV wavelengths are used for ozone inversions. The sensitivity is much lower in the visible since the ozone absorption coefficients in the Chappuis band are temperature insensitive.

The external AVTP EDR has its error specified as “uncertainty,” which, in the limiting case, is the RSS of precision and accuracy. Since the uncertainty in AVTP from CrIS and CMIS will not be parsed into precision and accuracy, we assume a worst case situation in which the uncertainty is entirely precision or entirely accuracy and account for the worst case in both precision and accuracy error allocations. Most of the AVTP uncertainty is expected to be random.

Figure 7.3-6 shows the results of Monte Carlo simulations of different AVTP random errors: an EDR profile with 1.5 K or 3.5 K random error, depending on altitude; and two climatological profiles with 5 K and 8 K random error. The simulation includes sensor, neutral density, and ozone cross-section random errors. The climatological temperature profiles are based on SAGE National Weather Service (NWS) profiles. For winter, the standard deviation is about 8 K; for spring, summer, and fall, the standard deviation is about 5 K. The simulations show that the sensitivity to AVTP random error is indeed small. In fact, it may be possible to use the climatology we are deriving from SAGE NWS

profiles and still meet thresholds, but to baseline this would require a reallocation among all precision error sources.

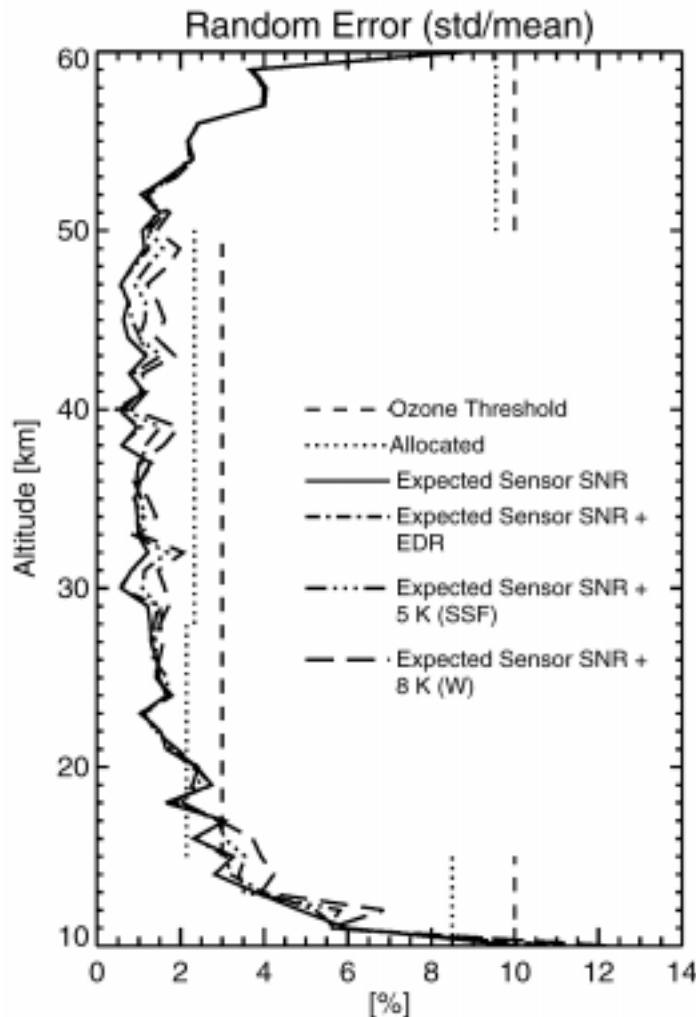


Figure 7.3-6. Random error due to sensor noise, neutral density precision, and ozone absorption cross-section random errors due to temperature sensitivity. The temperature profile errors used are the CrIS/CMIS AVTP EDR uncertainty thresholds and the standard deviations of AVTP climatologies derived from SAGE NWS data.

Neutral Number Density: Through simulations of the effect of sensor noise (above 20 km) or AVTP precision (below 20 km) on the neutral number density retrieval, we determined the effect of this error on the ozone retrieval. Above 20 km, we invert the neutral number density (NND) from Rayleigh-scattered radiances near 350 nm in order to reduce the dependence of our forward and inverse models on external EDRs.

Figure 7.3-2 shows the effect of expected and allocated SNRs on the retrievals. **Figure 7.3-7** shows the results of simulations using the same assumptions as Figure 7.3-2 except that we have included random temperature errors associated with the external AVTP EDR in the modeling process. The temperature errors introduce errors in NND and ozone cross-sections. The resulting ozone error is dominated by temperature-induced NND errors. NND errors are greatly reduced by the pair formulation in the UV and the pair/triplet formulation in the Visible. The mean random error from 25 to 55 km in Figure 7.3-7

increases by only 0.05% relative to the mean for the case shown in Figure 7.3-2, corresponding to a ~0.3% error due to NND alone. Between 15 and 25 km the increase is even smaller, 0.007%.

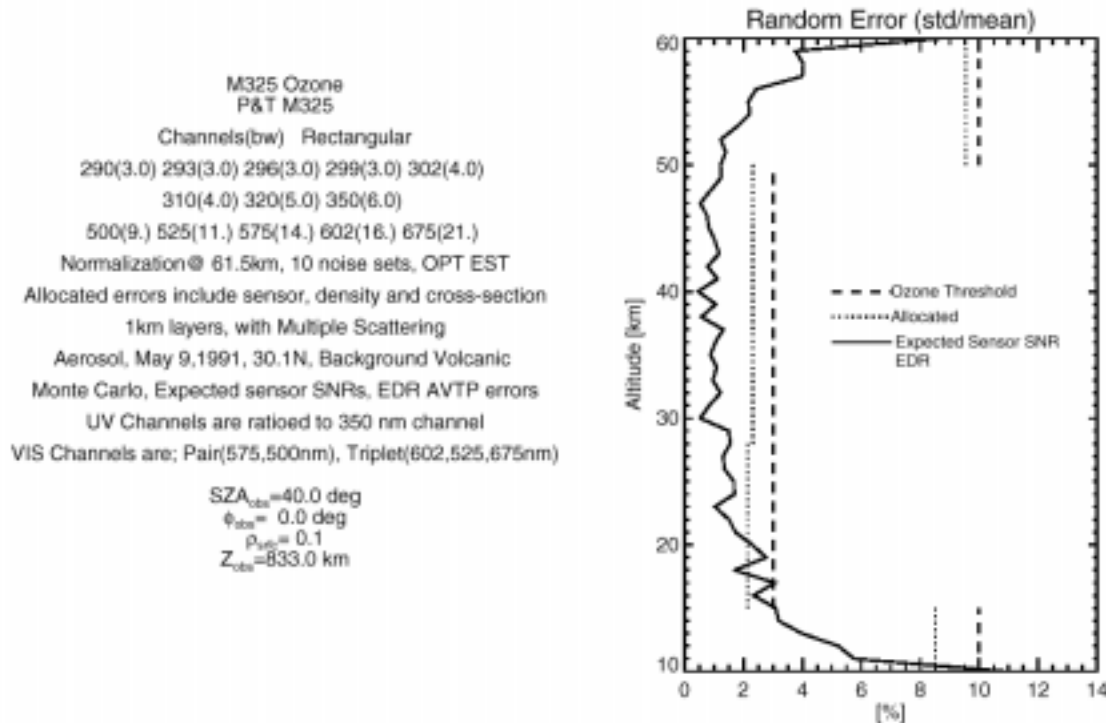


Figure 7.3-7. Simulation of profile precision error including the effect of sensor noise and external temperature profile EDR precision, which affects both cross-section and neutral number density (NND) error.

To enhance the limb profiler standalone capability we invert NND from the 347 and 353 nm channels. Inversions of NND using expected sensor SNRs in these two channels show that the density inversions will have random errors of 0.5 to 1% from 20 to 60 km. Simultaneous inversions of ozone and NND, in which the inverted NND is used in the radiative transfer, show that this level of random NND error again has a small effect on the ozone random error. **Figure 7.3-8** displays the random errors in ozone for this case. Below 20 km the NND kernel amplitudes decrease rapidly (Figure 2.4-4) and it is not possible to invert density with reasonable sensor SNRs. Below 25 km, the effects of the small NND kernel amplitudes appear in ozone. As a result, inverted NND values below 25 km will be replaced with NND values based on external EDRs, or based on climatology if external EDRs are unavailable (see PDR, p. 433).

A 1.5 degree error on a temperature value of 250K gives 0.6% error in NND, which is close to the 0.5-1.0% precision error we have in inverted NND now. Therefore, we can derive an allocation that will hold for NND inverted from our observations or derived from the external EDR. The precision allocations to NND are 0.5% for tropopause-15 km and 50-60 km, and 0.3% for 15-50 km.

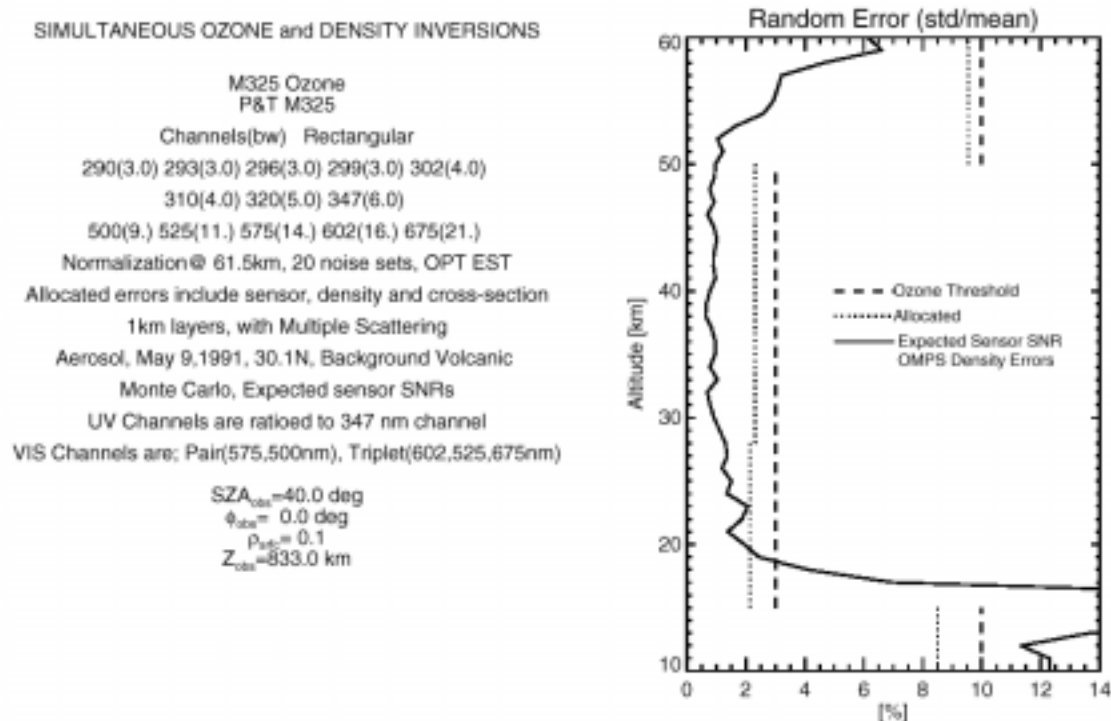


Figure 7.3-8. Simulation of profile precision error including the effects of sensor noise, cross-section precision due to external temperature EDR precision, and the precision of the neutral number density (NND) inverted from the 347 nm Rayleigh scatter channel. Below 20 km, the amplitude of the NND kernels drops rapidly. Consequently, the error in the ozone retrieval increases rapidly. Therefore, below 20 km we use the external temperature profile EDR or climatology to derive neutral number density with precision results as shown in Figure 7.3-7.

Aerosol Correction: The baselined aerosol correction technique is the use of the 525, 600, 675 nm triplet in the visible and the 400 nm observation in the UV. The allocation is based on the sensitivity of the aerosol correction to sensor noise.

Surface/cloud top pressure: The 1000 nm channel is baselined to determine the cloud top pressure. Surface pressure is determined from the external pressure profile EDR, or from a climatology if the external EDR is not available. The allocation is based on estimates of the sensitivity to cloud top pressure and the uncertainty in cloud top pressure from a 1.0 km vertical resolution using observations at a wavelength of 1000 nm.

Surface and cloud reflectivity and cloud fraction: The allocations are based on the sensitivity of the reflectivity and cloud fraction retrievals to sensor noise from the Rayleigh reference channels.

Inhomogeneity along the line of sight (LOS): There are three parts of the radiative transfer where inhomogeneity can cause errors: attenuation of the direct solar beam, the upward diffuse component, and the attenuation due to absorption along the line of sight. The line-of-sight (LOS) component is the largest. This allocation accounts for ozone and aerosol variability along a limb LOS. Although the LOS observation is strongly weighted near the tangent point, it includes significant contributions from the entire 250 km cell as well as from outside the cell. These allocations are based on an evaluation of the

effects of horizontally inhomogeneous aerosol and ozone distributions on solar occultation measurements [Chu and McCormick, 1979].

Cross-track inhomogeneity: This allocation accounts for the ability of a slit observation that is 3 km wide cross-track to represent a 250 km cell. The ozone variability was determined using gridded TOMS data (1 deg x 1 deg) at 60 deg S latitude, where we expect a high level of variability. The profile information is derived from the TOMS standard profiles, whose shape is highly correlated with total ozone. At 60 deg S, 1 degree of longitude is ~5 km and 1 degree of latitude is ~110 km. A 250 x 250 km cell is constructed from 5 longitude grid points and 2 latitude grid points. A total of 72 cells were constructed in this way.

The ten profiles in each cell were averaged to determine a profile representative of a 250 x 250 km cell. The first and last profile plus intervening total column amounts were used to interpolate in between, as could be done with the limb sensor slit measurements. The deviation of the average of the interpolated profiles from the “true” average over the 250 x 250 km cell was determined. The results from 72 cells, shown in **Figure 7.3-9**, were used to derive the allocation. The allocation above 15 km (120 mb) is 1%; below 15 km, it is 2%.

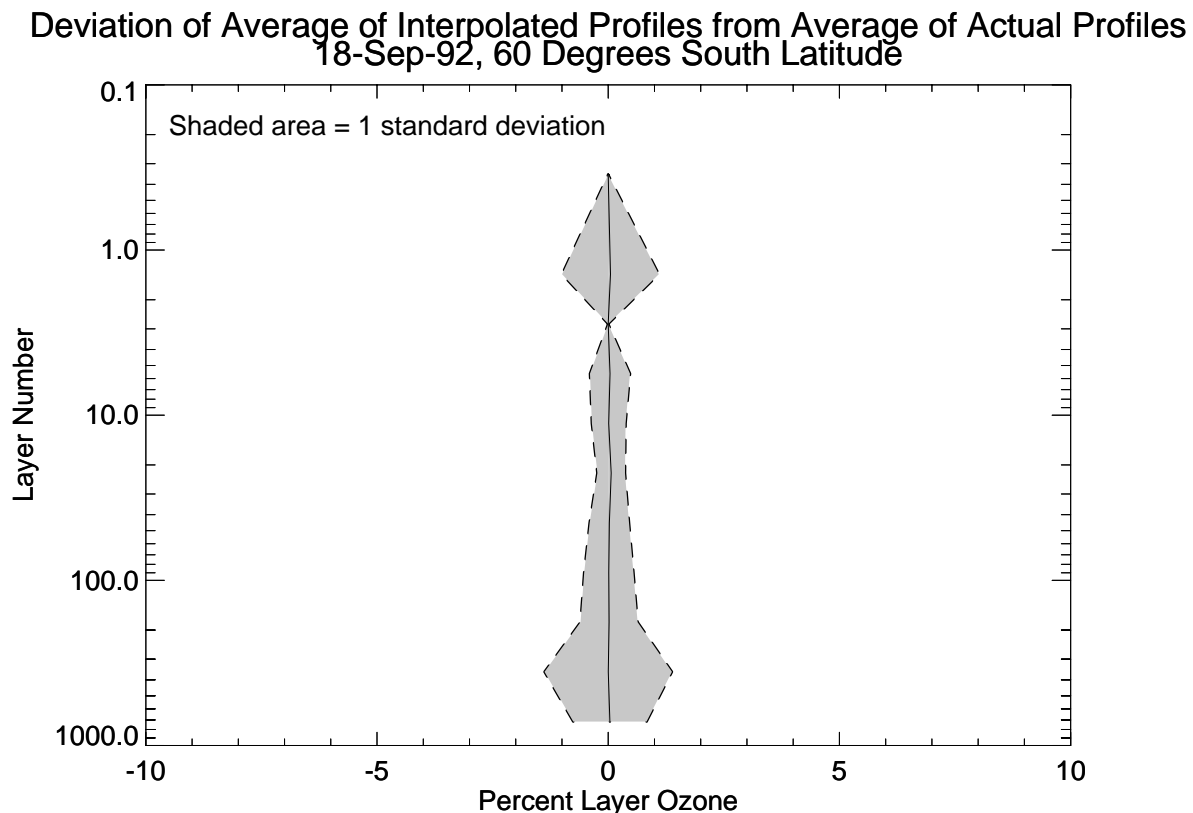


Figure 7.3-9. Deviation of average of interpolated profiles from average of actual profiles over 250 x 250 km near the edge of the ozone hole.

7.3.3 Algorithm Altitude Registration Precision Allocation

In order to meet the system precision requirements, the precision of the altitude registration of the limb profile must be very good. We have allocated 50 meters based on analysis that shows that such precision is needed in order for the requirement to be met in most cases. **Figure 7.3-10** shows the allocated precision for altitude registration and how the ozone retrieval is affected by the registration uncertainty. **Figure 7.3-11** shows analysis for a wide range of profiles. In all cases, except for a very limited range of altitudes, the precision requirement can be met with the current allocations.

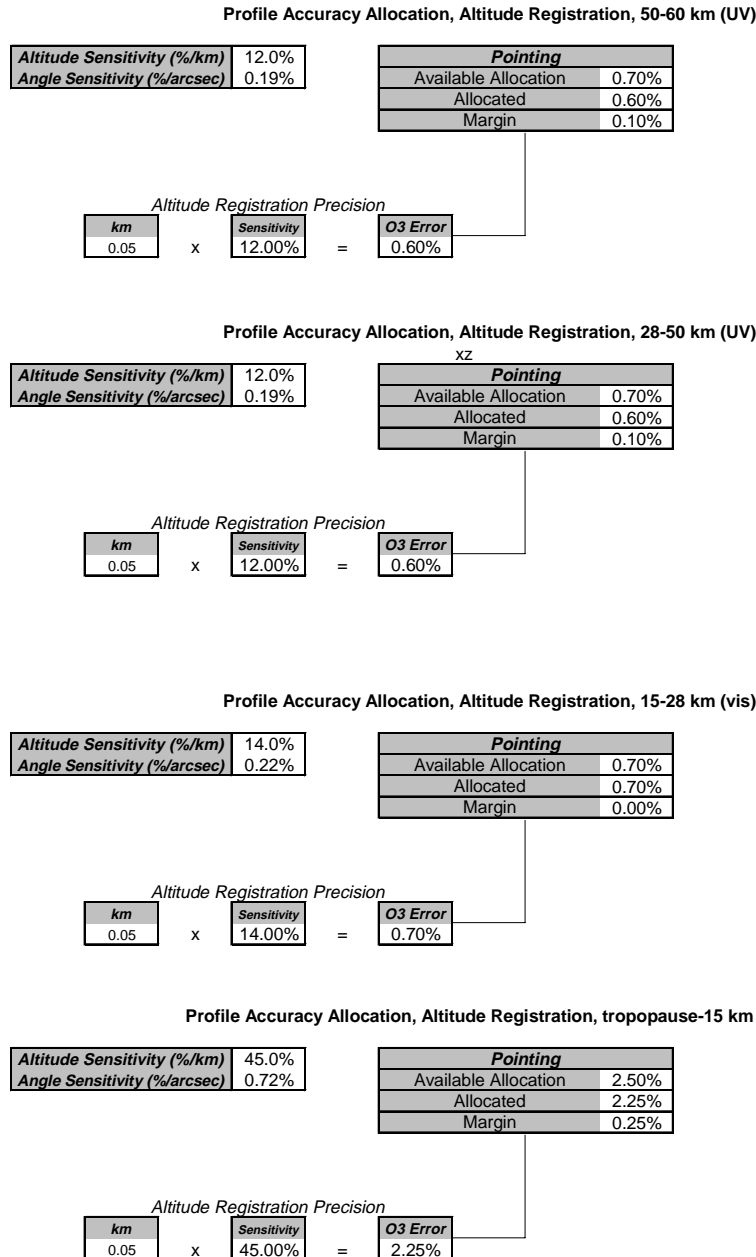


Figure 7.3-10. Allocation of random errors associated with altitude registration of the limb observations. As in Figure 7.1-7, the altitude sensitivity determines the scale of the error for a given pointing uncertainty.

We have investigated a method of altitude registration for the Limb profiler which does not rely on precise attitude information from the spacecraft. Attitude data included in each RDR are first used to establish a baseline altitude registration for the Limb sensor vertical cells. Radiance data from the Nadir profiler are then colocated with a Limb horizontal cell in the SDR algorithm. The Nadir radiance data are used to derive the ozone profile in the “exponential” region of the atmosphere, generally above 3 mbar. An average profile is determined corresponding to the center Limb cell. Using the limb scattering forward model, theoretical limb radiances are generated as a function of altitude using the ozone profile from the Nadir sensor. A χ^2 minimization with the measured Limb radiances yields the most probable altitude registration of the Limb vertical cells.

We have estimated the vertical resolution achievable through such a method by simulating random errors in the various input quantities from the Limb and Nadir profilers. The region between 40 km and 50 km is chosen because the Nadir profiler has consistently good sensitivity here under a variety of solar zenith angles, and because the exponential model of the atmosphere holds reasonably well here. This model states that the total pressure and the ozone concentration both decrease exponentially, though at different rates. The ratio of rates is given by the quantity σ . The relationship between ozone and pressure can be written

$$X = C p^{1/\sigma}$$

where C is the column ozone amount above 1 mbar and X is the column amount above a pressure p. For a standard TOMS ozone profile, M325, the value of C is approximately 1.5 DU and $\sigma \sim 0.57$.

The values of C and σ are standard products for the SBUV instruments, and hence will also be available from the Nadir profiler. The process by which C and σ are determined from nadir data is straightforward, and is described in detail by McPeters [1980]. The SBUV zonal mean value of C varies little, less than 0.2 DU below 40 degrees latitude. For comparison, a Limb inversion of simulated radiances from a M325 profile yielded C values of 1.1 DU and 2.3 DU when the radiances were shifted down 1/4 km and up 1/4 km, respectively. Herein lies the sensitivity of this method to altitude registration.

The vertical resolution achieved using independent knowledge of the ozone profile can be written

$$\Delta z = \Delta X \frac{dz}{dp} \frac{dp}{dX}$$

where ΔX is the error in column ozone above a given Limb cell. **Figure 7.3-12** contains a representation of our simulation of altitude resolution. The error in column ozone can be approximated by the error in layer ozone amounts, as shown. The value of dp/dX is found from the C and σ relationship above:

$$\frac{dp}{dX} = \sigma \frac{p^{1-1/\sigma}}{C}$$

The value of dz/dp is determined from the pressure profile.



In simulating errors we perturbed ΔX randomly in each of 4 cells by 2.4%, the sensor precision allocation. In addition, we randomly varied ozone in the 4 cells together by 1.8% to simulate algorithmic errors, which tend to be correlated between vertical cells. We also introduced variations into the sensitivities dz/dp and dp/dX . Uncertainty in p and dz/dp was simulated using 0.5% uncertainty in neutral density and a 1.5K temperature uncertainty. Finally, errors in C and σ were modeled using the allocated S/N ratios for the Nadir profiler. The resulting distribution of Δz for 10000 samples, shown in **Figure 7.3-13**, has a standard deviation of 0.027 km.

It should be noted that the determination of p is not affected by errors in altitude registration except through the temperature value. Iterations would eliminate this error as well. In this simple analysis, several error sources have been neglected. Some contribute to systematic offsets in the altitude registration, which we are not addressing here. Another precision error source is variations in the degree of non-exponential ozone behavior in the 40-50 km region. We believe that much of this variation may have a predictable dependence on atmospheric path length, and so can be removed.

In summary, this new technique, based on the well-understood capability of nadir buv profiling in the upper stratosphere (40-50 km), has the potential to improve significantly the precision of the limb profile altitude registration. This result would be achieved by a direct comparison between the nadir profile and the along-track limb profile measured from the same spacecraft. The allocated performance is based on 0.05 km altitude registration precision, about twice the expected performance.

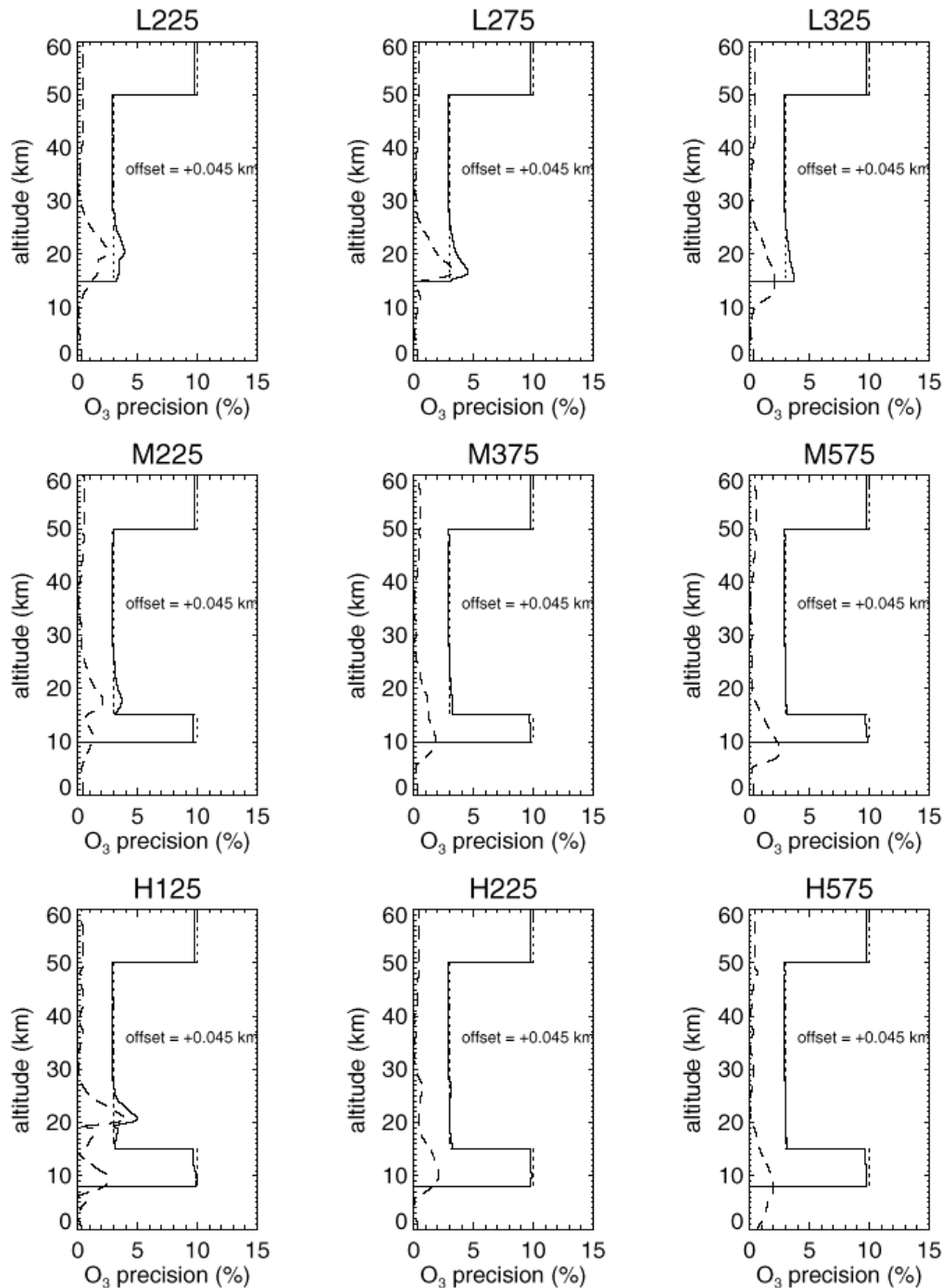


Figure 7.3-11. Ozone profile precision for a wide range of ozone profiles and ~50 meter altitude registration precision. Dotted lines represent the precision threshold. Dashed lines represent the magnitude of the ozone error due to 2.8 arcsec pointing precision. Solid lines represent the total profile accuracy from a RSS of the error due to 50 m altitude precision and the PDR sensor and algorithm precision allocations. Each profile is identified by a letter representing the latitude (L = low, M = mid, H = high) and the total ozone amount in DU. Tropopause at 15 km, 10 km, and 8 km are assumed for low, mid, and high latitude profiles.

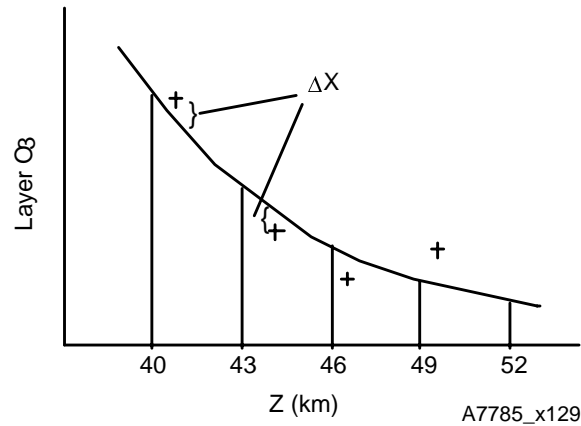


Figure 7.3-12: A representation of our simulation of altitude resolution. X is the column amount above a pressure p . The error in column ozone can be approximated by the error in layer ozone amounts, as shown.

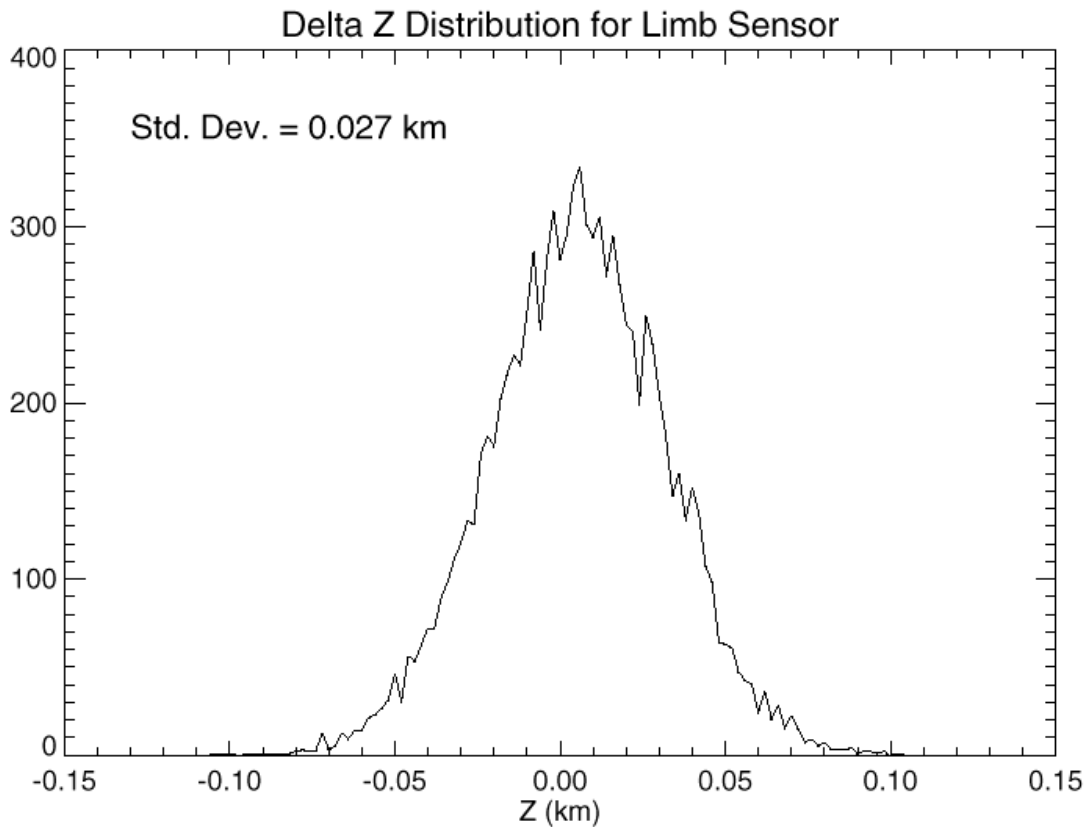
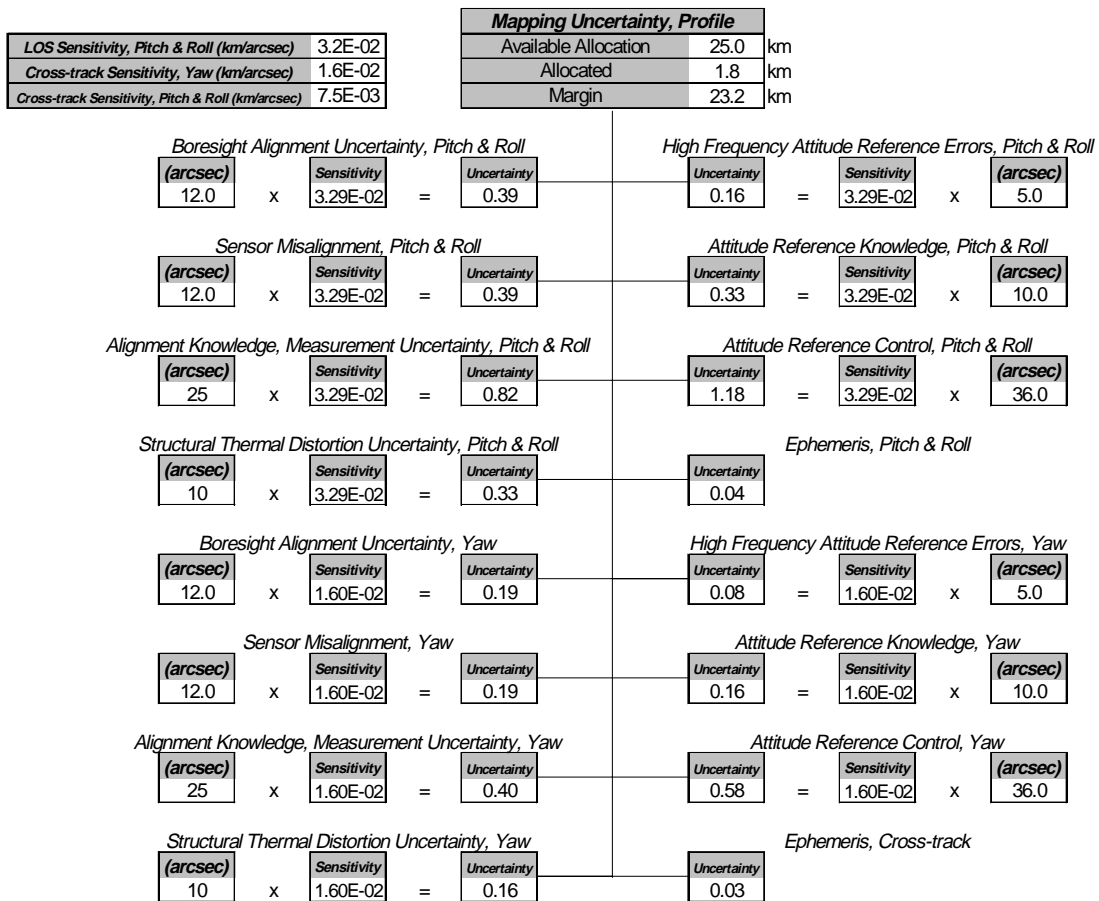


Figure 7.3-13: Distribution of Δz for 10000 samples. The distribution has a standard deviation of 0.027 km. This results suggests that, exploiting the information in the nadir profile, an allocation of 0.05 km for the precision of the limb sensor altitude registration is appropriate.

7.4 Limb Profile Mapping Uncertainty

The limb profile mapping uncertainty allocations are based on the sensor and spacecraft specifications.



8 Test, Validation, and Calibration

8.1 Overview of Plans and Results

The Ball team uses several methods to test and validate the operation of the ozone retrieval algorithm and the algorithm-sensor system. The different approaches use either simulated data (generated from the forward model), actual instrument data (from the SOLSE/LORE mission), or simulated data run through a simulated sensor. All approaches result in a retrieval using the OMPS limb profile algorithm to test the performance of the retrieval. Retrievals using simulated data enable us to determine algorithm sensitivities to various sensor and parameter uncertainties. Retrievals using the limb scatter measurements of the SOLSE and LORE instruments give results from actual instrument data and allow comparisons to retrievals others have done using the same data sets. The end-to-end simulations, in which the full process of sensor measurements and algorithm retrievals are performed, enable system trade studies and performance evaluations.

8.2 Simulation and Retrieval Procedures

We have performed two sets of simulations for the limb profile ozone algorithm. In one set, we generated simulated radiance using the forward version of the Herman Radiative Transfer Model for a given set of viewing conditions, using standard ozone and temperature profiles, the WPTB profiles, SBUV/2 data and SAGE II profiles. These radiances were either fed directly into the retrieval algorithm or sent to Ball to use as input to the sensor model. The first set of tests were decoupled from the sensor model and were designed to validate the numbers given in Section 7 and to test the algorithm performance. The second set includes the sensor model and represent end-to-end simulations designed to validate the sensor-algorithm system and to provide feedback useful in the design of both the sensor and the algorithm. Figure 8.2-1 illustrates our simulation approach.

The simulation process permits flexibility in verifying each module before full system testing. Modular implementation allows flexibility in investigating particular components such as the input ozone and temperature profiles, atmospheric radiative transfer models, instrument models, and algorithm components. In particular, at the component level, we monitor the module performance against operational constraints such as processing time and storage requirements. Only upon completion of the modular development do we pursue full end-to-end system verification and SDR/EDR algorithm performance evaluation.

An additional test of algorithm performance used flight data from the SOLSE/LORE mission and compares ozone retrievals using the GSFC and the OMPS algorithms. Correlative measurements are also used to evaluate the retrieval performance relative to other ozone profile measurement methods.

8.2.1 End-to-End Simulations

After satisfactory performance of the algorithms was demonstrated using the decoupled simulations, a full sensor model was constructed using Ball's TRADES simulation system to perform end-to-end tests. The end-to-end modeling simulations begin with viewing angles determined for a given scene using Ball's sensor model. These angles are used to generate the radiances using the Herman Radiative Transfer Model (RTM). Scene radiance data cubes are used as input to the sensor model and simulated RDRs are produced. Pseudo SDRs are constructed from the RDRs. The limb profile ozone retrieval algorithm is applied to these SDRs to produce limb profile ozone EDRs. Finally, the simulated EDR output is compared with the actual ozone input and with the EDR requirements.

8.2.1.1 TRADES Simulations

TRADES (Toolkit for Remote-sensing Analysis, Design, Evaluation, and Simulation) is a set of software tools, designed and developed at Ball, for simulating, analyzing, evaluating, and conducting design trade studies of remote sensing systems. To generate the input data for the sensor model, data from the Code V optical model of the OMPS sensor is used to define a set of viewing rays that correspond to the pixels on the focal plane. Scene radiance data cubes generated along these viewing rays are oversampled in both the spatial and spectral dimensions, permitting accurate simulation of the spatial and spectral responsivities of the sensor.

As used on OMPS, these input data cubes are run through several TRADES modules to simulate the measurement and calibration of radiance data. First the data cubes are input to the Imaging module where the spatial responsivity functions are applied resulting in an irradiance field at the entrance slit of the spectrometer. The spatial responsivity is composed of the detector aperture, the temporal aperture, a line-of-sight jitter path function, and an optical point-spread function (PSF) that varies across the focal plane. The resulting irradiance data cube at the spectrometer slit is then sampled at the detector spatial resolution. The prism spectrometer model then generates the in-band irradiance falling on each detector pixel in the focal plane array by convolving the spectral slit cube with the prism dispersion function. The spectral transmissivity of the sensor is also applied through the simulation.

The Detection module receives the in-band spectral irradiance cube, applies the detector quantum efficiency, adds dark current, simulated readout effects, adds noise, and simulates the quantization of the analog-to-digital converter. The noise power spectral densities and the transfer function of the readout electronics are used together to generate a noise time series that includes the correlations induced by the readout electronics responsivity and the aliasing effects of the focal plane sampling. Finally, the noisy signal from each detector element is quantized.

The Calibration and Test module is used to test the sensor simulation using point sources, knife-edges, spectral scans, and flat fields and to simulate the calibration of the sensor. The OMPS simulations generate the calibration coefficients that are used in generating SDRs for use in the retrieval algorithm. Finally, the Formatting module is used to aggregate detector elements to the final resolution of the output data.

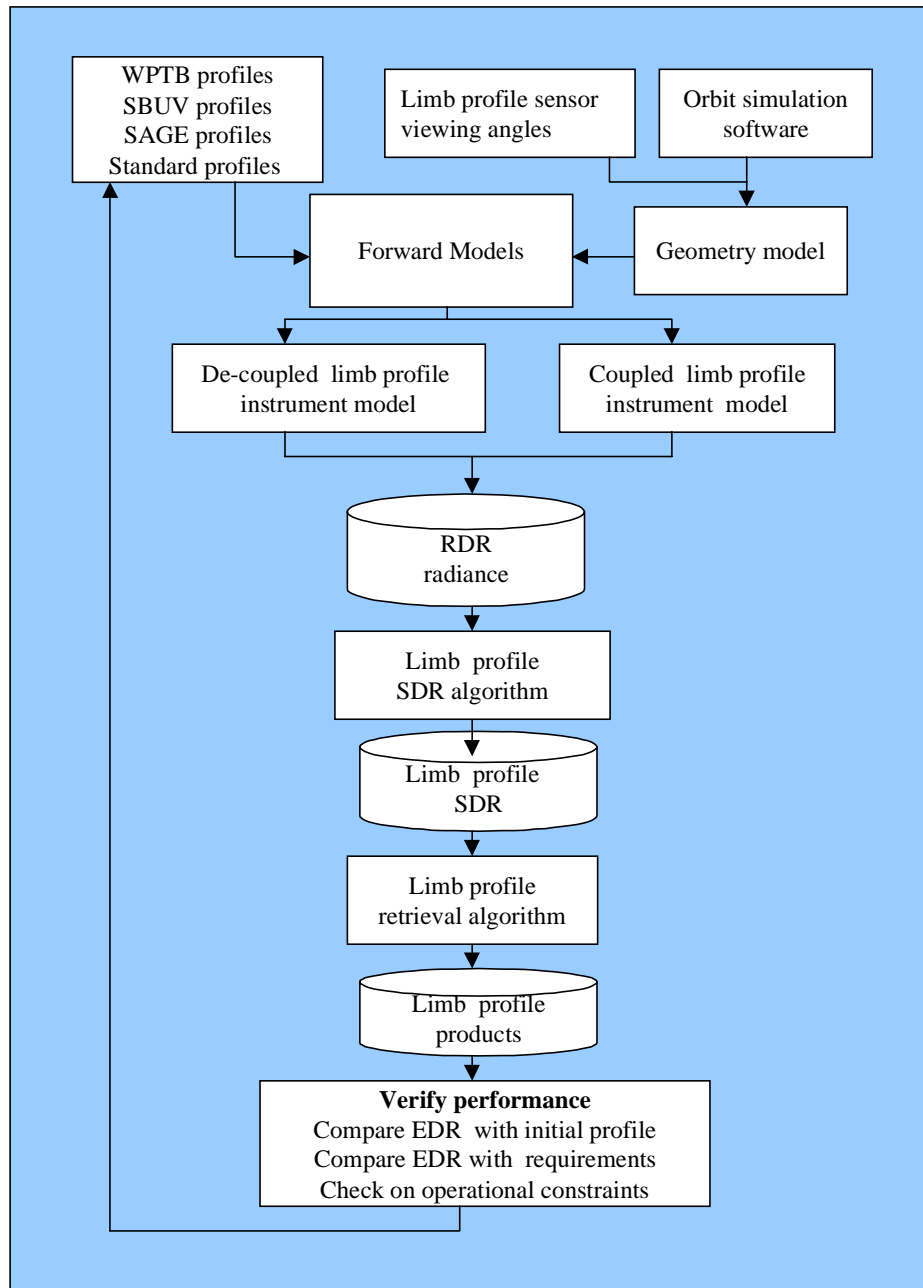


Figure 8.2-1. The Ball team uses an end-to-end approach in testing and validating OMPS limb profile performance of our sensor-algorithm system.

8.3 Test Cases

8.3.1 Algorithm Performance

The simulations for algorithm performance consist of Monte Carlo simulations designed to validate the error budget allocations in Section 7. These simulations used the standard TOMS V7 ozone and temperature profiles, SAGE II profiles and the 91 profiles of ozone and temperature obtained from the WPTB. These latter ozone profiles combined measurements from SAGE II with balloonsonde measurements with corresponding temperature profiles taken from the balloonsonde measurements. **Table 8.3-1** indicates the location and number of profiles from each test site for the WPTB data. The ICSR E8092501 (Tests using WPTB profiles) contains pertinent information regarding our approach.

Table 8.3-1. Location and number of profiles in the WPTB database.

Station Name	Country	# of Profiles	Lat	Long	Category*
Sapporo	Japan	6	43.05	141.333	WS
Alert	Canada	4	82.5	-62.3	WS
Resolute	Canada	4	74.72	-94.98	WS
Goose	Canada	9	53.32	-60.344	WS
Hohenpeisenberg	Germany	8	47.8	11.02	WS
Syowa	Japan	4	-69.0	39.58	WS
Wallops Island	USA	5	37.933	-75.483	WS
Naha	Japan	7	26.2	127.683	WS
Natal	Brazil	3	-5.84	-35.21	WS
Marambao	Argentina	8	-64.233	-56.717	WS
Laverton	Australia	9	-37.867	144.7	WS
Boulder	USA	7	40.03	-105.25	CS
Hilo	USA	6	19.72	-155.07	CS
Pago Pago	USA	5	-14.25	-177.56	CS
Papeete	Tahiti	3	-17.50	-149.5	CS
South Pole	USA	3	-85.26	-89.98	CP

* Category

WS ozone profile (total 67 files) data from WODC sondes and SAGE II matchup.

CS ozone profile (total 21 profiles) data from CMDL and SAGE II matchup.

CP ozone profile (total 3 profiles) data from CMDL SP and POAM matchup.

8.3.2 SOLSE/LORE Retrievals

SOLSE and LORE data from the 1997 Shuttle flight have been processed by GSFC Code 916 using the OMPS limb heritage ozone retrieval algorithm. We obtained a subset of these data and used it to simulate the OMPS limb sensor data. We retrieved ozone profiles using the OMPS limb profile algorithm.

SOLSE and LORE instruments were co-boresighted limb-viewing sensors designed to measure profile ozone concentration. The SOLSE sensor had a continuous spectral range of 270-360 nm with a 0.3 nm spectral resolution. All channels and altitudes were measured simultaneously. The LORE sensor measured limb-scattered radiances at 345 nm, 525 nm, 600 nm, 675 nm, and 1000 nm with a resolution of 3 nm. All altitudes were measured simultaneously, but channel measurements were sequential. Both sensors were flown aboard the November-December, 1997 Space Shuttle flight. Vertical resolutions

were 0.35 km and 0.25 km for SOLSE and LORE, respectively. More information on the sensors is contained in Janz et al., 1998.

Both detector saturation and internal scattered light limit the scope of ozone retrievals from these data. SOLSE and LORE saturated over bright scenes, thus restricting the analysis to data with few clouds. While both sensors had a significant problem with internally scattered light, the situation on LORE was worse. On LORE, light was scattered internally through reflections off an entrance window and through diffuse reflections. Diffuse internal scatter varied from 0.5% to 1.5% in-band and 0.25% and 0.7% out-of-band, depending on wavelength. Scattered light corrections were developed at GSFC based on post-flight instrument testing. The OMPS limb sensor is being designed to minimize such stray light effects.

8.3.3 End-to-End Test Runs

In the end-to-end system simulations, limb radiances were generated from a given ozone profile (from a SAGE II, WPTB, or TOMS ozone profile). The initial test case chosen for testing of the limb retrieval is a 325M standard TOMS profile.

8.4 Analysis and Results

Results from the various simulations are given below.

8.4.1 Algorithm Performance – Monte Carlo Simulations

The test of algorithm performance using simulated radiance data was used to validate sensitivities used in the system error budgets shown in Section 7. Many of the retrievals of test cases are shown in Section 7 with accompanying information on the profile used and the noise and bias terms that were included in the simulation (see Figures 7.1-5, 7.3-2 through 7.3-8).

8.4.2 SOLSE/LORE Retrievals

The data taken on-orbit by the SOLSE and LORE instruments was calibrated and ozone profiles were retrieved using the GSFC retrieval algorithm and the OMPS limb profile algorithm. Comparisons of the two retrievals show very good agreement between the two retrievals and with correlative measurements made by HALOE and by a balloonsonde.

GSFC Retrievals

The two orbits of existing data are comprised of approximately 90 frames of SOLSE data and approximately 130 frames of LORE data. Following saturation screening and scattered light corrections, ozone profiles were retrieved separately for the two data sets using the Herman-Flittner code. Eleven SOLSE channels between 300 nm and 360 nm, degraded to 1 nm resolution, were used in the retrievals. Wavelength pairing and altitude normalization techniques were applied. LORE retrievals were based on the Chappuis triplet (525 nm, 600 nm, 675 nm). Mean results are shown in **Figure 8.4-1**. SOLSE and LORE retrievals converge to consistent profiles even with a retrieval first guess far from the likely ozone profile.

Correlative measurements for the two orbits were obtained from balloon ozone sondes at Ascension and Reunion Islands, and from HALOE retrievals. The Ascension results, which were coincident in time with some of the SOLSE/LORE data, are compared with the GSFC retrievals in Figure 8.4-1. Agreement within 5% was achieved at the ozone peak, even though the GSFC results are the average for a full orbit.

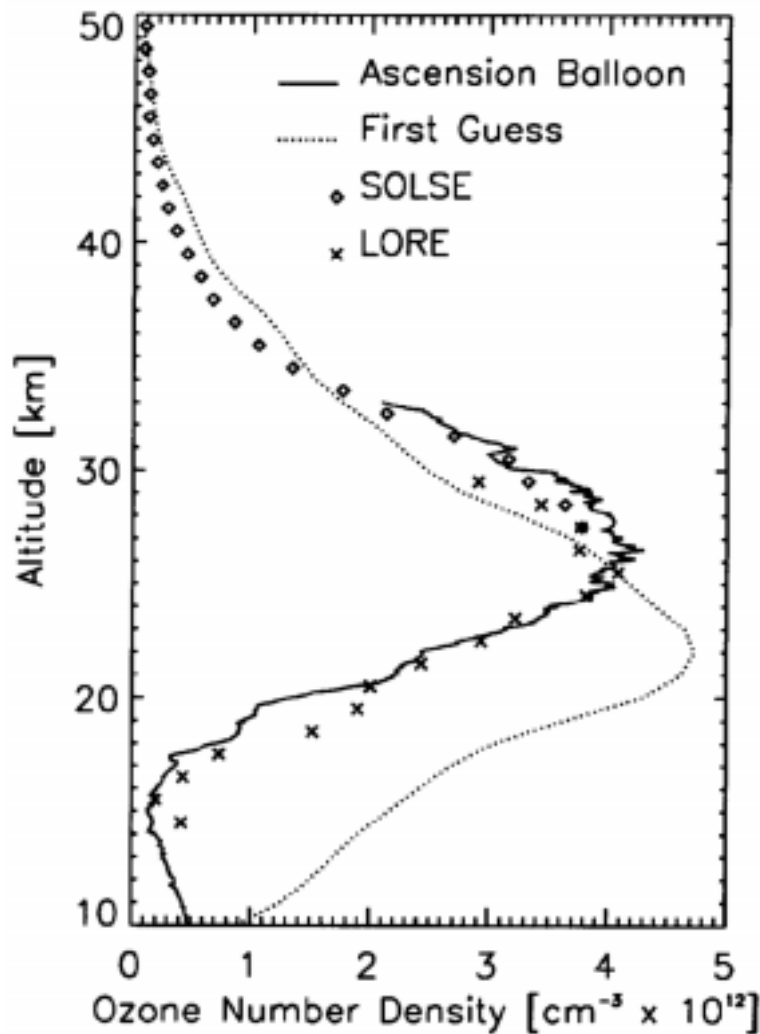


Figure 8.4-1. The mean ozone profile retrievals are shown for a single orbit of SOLSE and LORE data. Differences from the retrieval first guess indicate that the algorithm converges on a unique solution for even poor first guesses. Agreement is within 5% at the peak with balloon sonde profile measurements from Ascension Island.

OMPS Retrievals

We obtained five frames each of clear-scene SOLSE and LORE data and used these to simulate an OMPS limb measurement. The data from each sensor were nearly coincident with one another, and come from a mid-Atlantic region, approximately 10° N and 30° W. These data were coincident in time with the Ascension sonde, but approximately 2000 km distant. These same data are nearly coincident spatially with a scan from HALOE, which was approximately 18 hr. after the SOLSE/LORE measurements.

SOLSE and LORE data were first placed into a pseudo-OMPS SDR format. Since OMPS and SOLSE channels are measured simultaneously at all altitudes, it was necessary to first adjust different LORE channels to a common altitude scale. The Shuttle Orbiter rolled significantly during data acquisition, making such adjustments necessary. Altitude registration of SOLSE and LORE pixels was determined

from the Rayleigh-scattered signal in the 345 nm channel. The altitude registration of the pixel array in a given LORE channel was adjusted up or down by an integral number of pixels so that it corresponded to what the registration would have been were the channel measured simultaneously with the 345 nm channel. Linear interpolation between SOLSE and LORE 345 nm registrations was used to find the most probable registration for a given LORE channel.

Though the SOLSE/LORE data used were already calibrated, it was necessary to subtract an additional $1 - 4 \text{ W/cm}^3/\text{sr}$ from all pixels in a given channel to account for scattered light. No further adjustments were made to LORE data. SOLSE channels were combined to degrade the spectral resolution to 3 nm in each channel. The channels selected for the SOLSE retrievals are listed in **Table 8.4-1**.

Table 8.4-1. SOLSE data
used in OMPS retrieval.

λ	Max. Retrieval	Norm. Altitude
290	71 km	61 km
293	58 km	61 km
296	54 km	61 km
299	49 km	59 km
302	46 km	55 km
310	44 km	50 km
320	38 km	45 km
325	32 km	40 km

A spatial point spread analysis of the SOLSE sensor was also implemented in the OMPS retrieval through an adjustment to the radiances calculated by the forward model. Estimates of random signal noise are required for the sensor covariance matrix used in the inversion. Noise at the native SOLSE resolution ranged from 1% at 290 nm to 0.25% at 350 nm, and was independent of altitude. The noise assumed for LORE was 0.25% at 0 km and 3% at 80 km, independent of channel. Normalization altitudes for some channels were lowered to reduce the effect of internal scattered light at high altitudes. The LORE normalization altitude was 40 km, and SOLSE altitudes are given in Table 8.4-1. In addition, retrievals were restricted to regions where channels have significant contribution functions. This prevents the retrieval from having difficulty when inconsistent radiances are observed in two different channels. Such inconsistencies were primarily a result of inadequate scattered light corrections.

No wavelength pairing was used for SOLSE retrievals. This allowed OMPS UV retrievals to be pushed somewhat lower in altitude than the GSFC retrievals, because saturation was then not an issue. The triplet retrieval was used for LORE data. A surface reflectance of 10% was assumed for all retrievals.

The OMPS retrieval of SOLSE data is shown in **Figure 8.4-2**. Values in each vertical cell are the average of the 5 retrievals. Error bars indicate the standard deviation of those retrievals. The GSFC retrieval average from Figure 8.4-1 is also shown for comparison. Results from the two retrievals are consistent, though the OMPS statistical sample is not as good. These retrievals also compare well with the HALOE results. HALOE data have been found to agree to within 3-4% with correlative data from SAGE and from ozone sondes (J. Russell, personal comm.). Therefore, differences of <14% from HALOE constitute OMPS threshold accuracy performance.

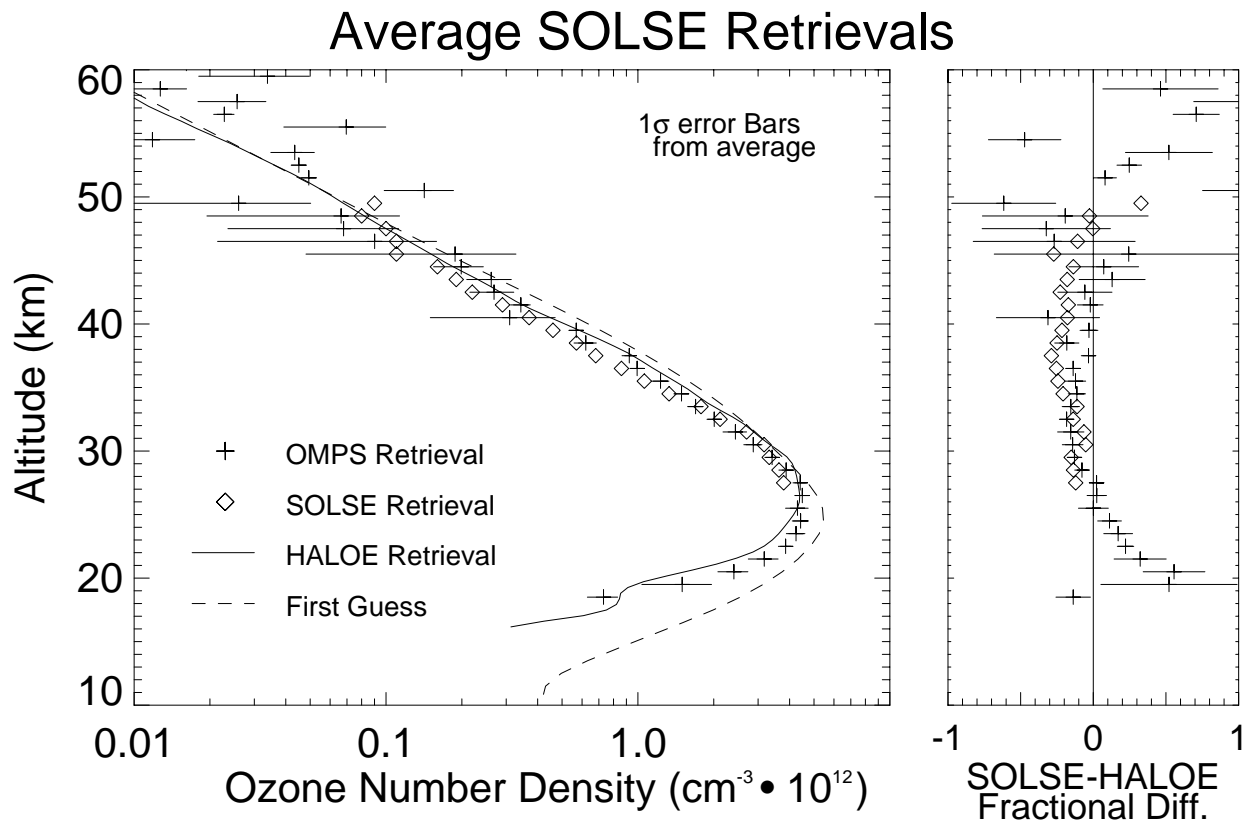


Figure 8.4-2. Ozone profile retrievals of 5 SOLSE frames using the OMPS-Limb retrieval algorithm are shown. The GSFC retrieval average from a full orbit is also shown. Both are compared to a single correlative HALOE retrieval.

The OMPS retrieval of LORE data is shown in **Figure 8.4-3**. Values in each vertical cell are the average of the 5 retrievals. Error bars indicate the standard deviation of those retrievals. Again, the agreement with the GSFC retrievals is very good. A comparison is shown with the Ascension ozone sonde results. Agreement is excellent down to about 20 km. At this point, scattered light and the lowered normalization altitude begin to play a role, drastically increasing the retrieval uncertainties. The tropopause at Ascension Island was 16-17 km.

In addition to the separate retrievals of SOLSE and LORE data, the two were combined to produce a pseudo-SDR and ozone was retrieved. This more closely represents the OMPS limb sensor, where all channels will be measured simultaneously. The LORE altitude registration was adjusted by interpolating radiances on the scale defined by each SOLSE frame. Retrieval results, shown in **Figure 8.4-4** are similar in most respects to a superposition of the individual retrievals. A notable deviation between 40 and 50 km is caused by the first guess. An unrealistic first guess profile was used to demonstrate the robustness of the algorithm. But the random uncertainties that comprise the SOLSE covariance matrix effectively increase with altitude. This is because high altitude retrievals use shorter wavelength, noisier channels. Beginning near 40 km, the uncertainties are too large to pull the retrieval away from the first guess, yet small enough that the *a priori* profile is not dominant. Above 50 km, the *a priori* dominates. This effect is entirely a consequence of the high levels of scattered light in SOLSE.

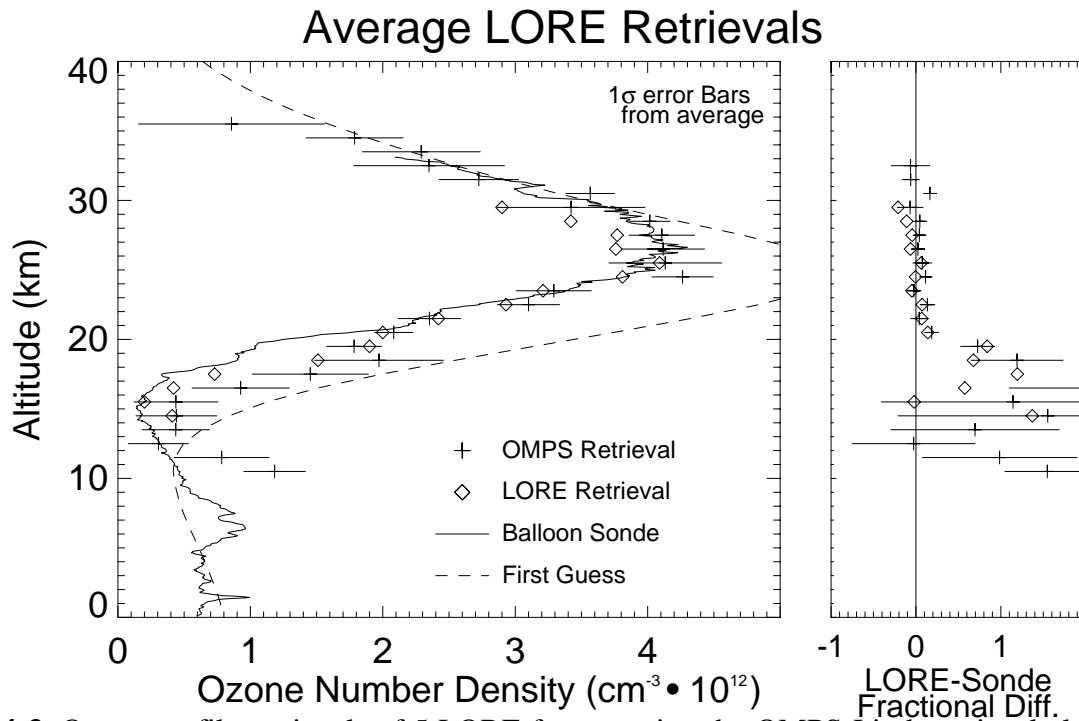


Figure 8.4-3. Ozone profile retrievals of 5 LORE frames using the OMPS-Limb retrieval algorithm are shown. The GSFC retrieval average from a full orbit is also shown. Both are compared to the Ascension Island ozone sonde results.

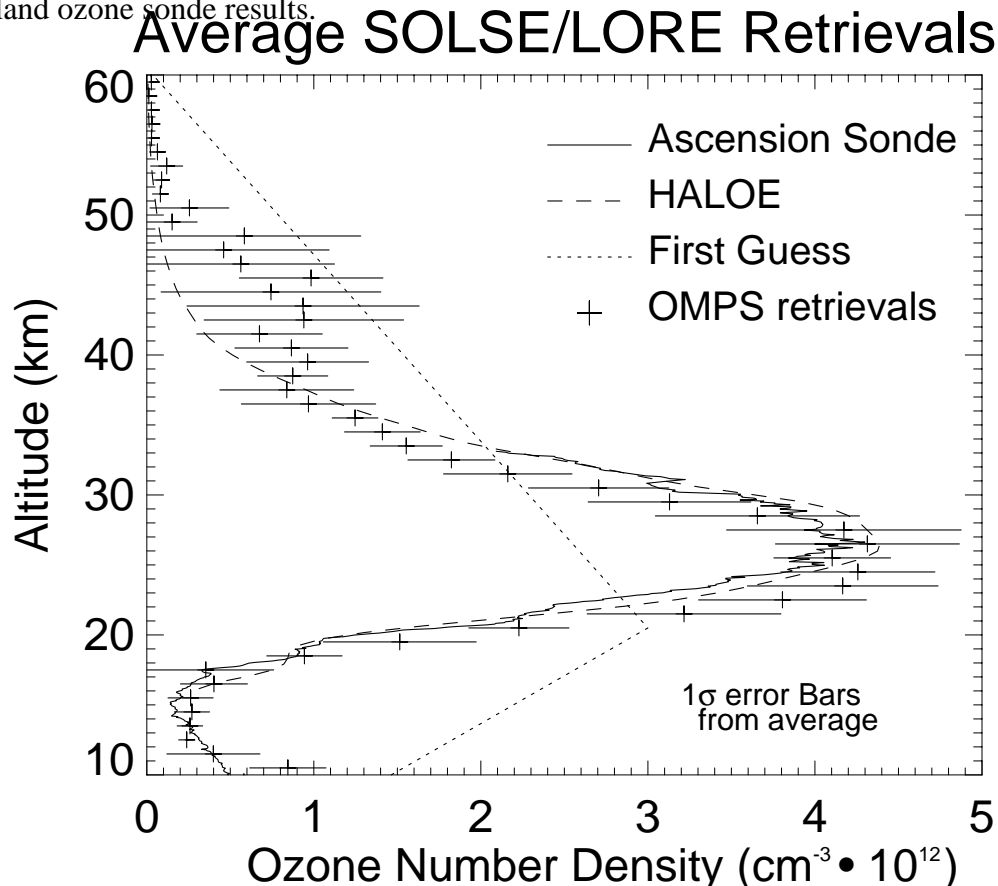


Figure 8.4-4. The average of retrievals of combined SOLSE and LORE data is shown.

Results from the combined retrieval agree well with both the Ascension sonde and with HALOE results, and are consistent with the individual sensor retrievals. A unrealistic first guess ozone profile was used to demonstrate the algorithm's independence of it.

Retrieval Conclusions

The OMPS Limb retrieval algorithm has been successfully applied to SOLSE and LORE data. SOLSE channels were chosen to correspond to the OMPS selection. The close agreement between GSFC and OMPS retrievals indicates

1. Modifications made to the heritage algorithm to produce the OMPS algorithm were made correctly.
2. The OMPS channel selection is no less appropriate for these data than the GSFC selection.
3. The lower OMPS resolution has little effect on retrieval results.

Both sets of retrievals are consistent with existing correlative data. Most instances of large differences can be attributed to the effects of internal scattered light. An examination of Figure 8.4-4 reveals an apparent altitude shift of 1-2 km between SOLSE/LORE retrievals and the HALOE and sonde results. An altitude registration error of this magnitude is consistent with the uncertainty associated with the Rayleigh scattering method used for SOLSE/LORE. If this is the case, the differences with correlative data will be much smaller once this error is corrected. We note that the altitude registration accuracy on OMPS is around 0.5 km (Figure 7.1-7).

We conclude that retrievals using SOLSE/LORE data and the OMPS limb profile algorithm have shown that threshold OMPS performance can be achieved. The OMPS limb sensor is being designed in a manner that is cognizant of the scattered light problem. Our simulations (see ICSR-8120201) indicate that the scattered light levels specified in the sensor design are adequate for threshold ozone profile precision and accuracy performance.

8.4.3 End-to-End Simulations

To date, one data cube has been generated and run through the OMPS limb sensor. This data cube uses a 325 DU, mid-latitude ozone profile. This data cube represents the limb scene radiance at a single instant of time, but has been used to simulate actual sensor output for retrieval assuming that the scene does not change over an integration time. The sensor model currently simulates the output from the focal plane pixels illuminated by the the primary image (the brightest image) of the center slit.

The input radiance data cube is shown in **Figure 8.4-5**. The calibrated sensor output radiance can be seen in **Figure 8.4-6**. Close examination reveals that the bandwidth of the spectrally-binned output pixels varies with wavelength due to the varying dispersion of the prism spectrometer.

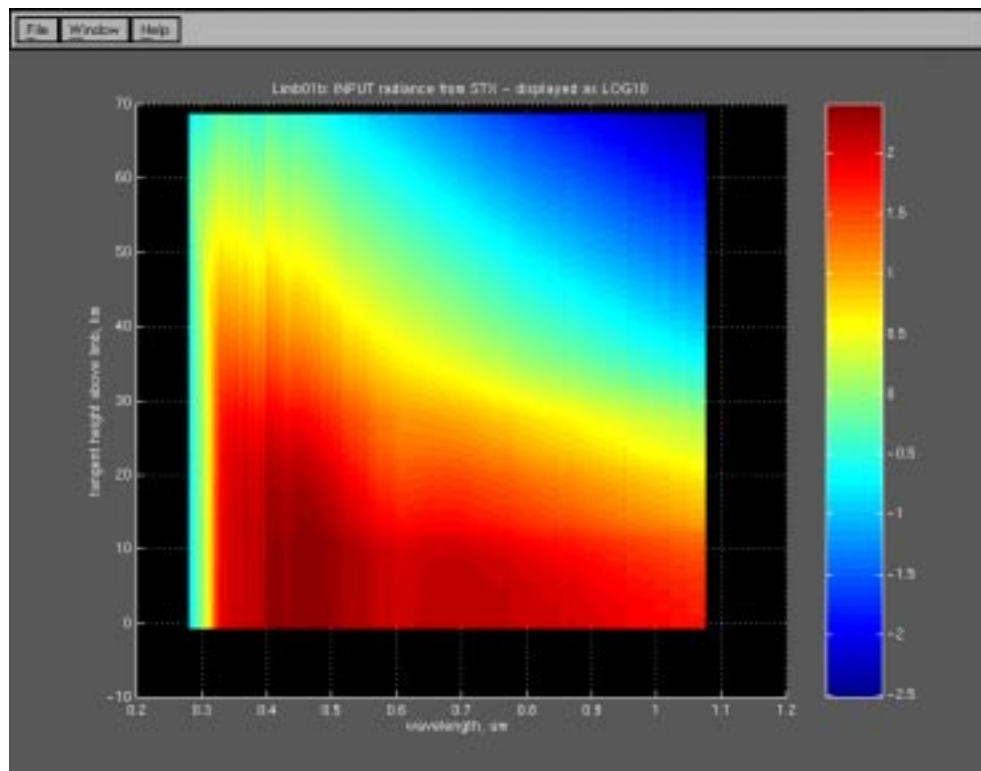


Figure 8.4-5. Limb radiance input data cube for limb profile sensor end-to-end model.

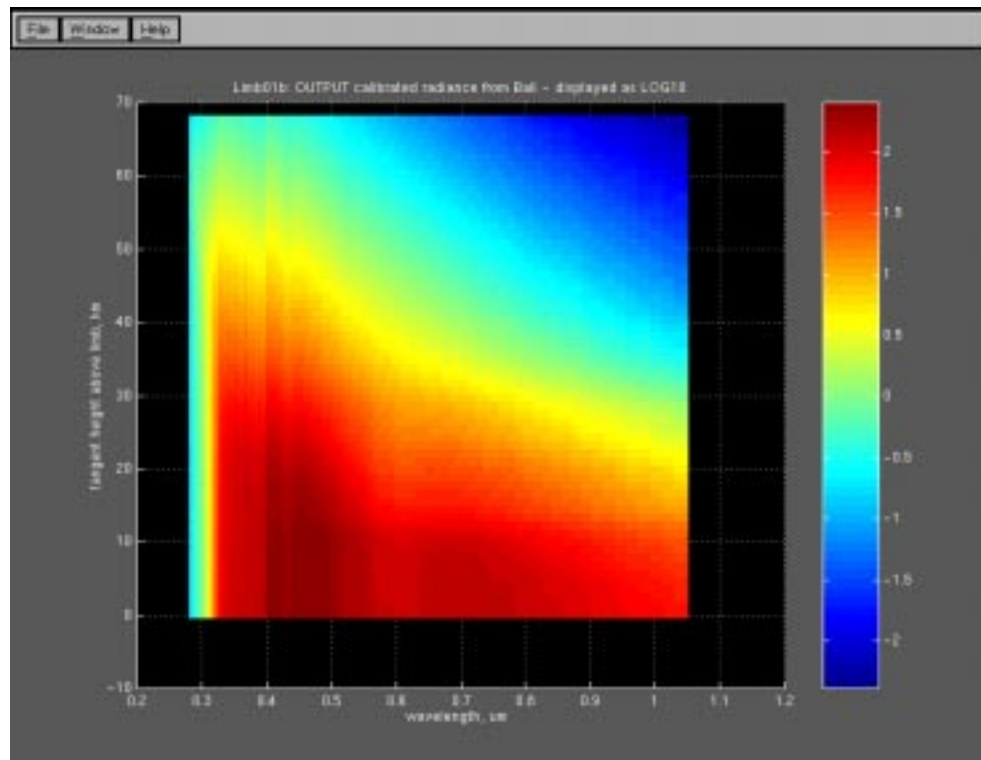


Figure 8.4-6. Sensor output radiance for limb profile sensor (center slit, primary image). The variable dispersion of the prism spectrometer can be seen in the spectral bin size increase with wavelength.



Plans

We plan to validate OMPS limb performances using end-to-end simulation using the shown test case and using other WPTB, SBUV/2, and SAGE II ozone profiles and with simulated solar and viewing geometry. Our results from these end-to-end tests will validate the performance of the algorithm-sensor system. The timing results from these tests will be scaled to estimate the algorithm's performance to produce an orbit's worth of EDRs within 20 minutes from availability of all the data.



8.4.4 Effect of Aerosol Loading on Performance

We test the algorithm performance to variations in aerosol loading by Monte Carlo simulations similar to those shown in section 7 of the limb ATBD. The aerosol data used was constructed from SAGE II aerosol measurements before, during and after the eruption of the Pinatubo volcano, which took place in June of 1991.

The SAGE aerosol data were assembled into zonal means and coupled with the appropriate TOMS V7 standard atmosphere for ozone and temperature. Model atmospheres for four months in 1991, 1992, and 1993 at the Equator, 30N, and 50N were constructed for Monte Carlo testing of the EDR algorithm. The Monte Carlo simulations included the expected sensor SNRs. A solar zenith angle of 40 degrees was used at 30N and 50N while a solar zenith angle of 20 degrees was used in the simulations at the equator.

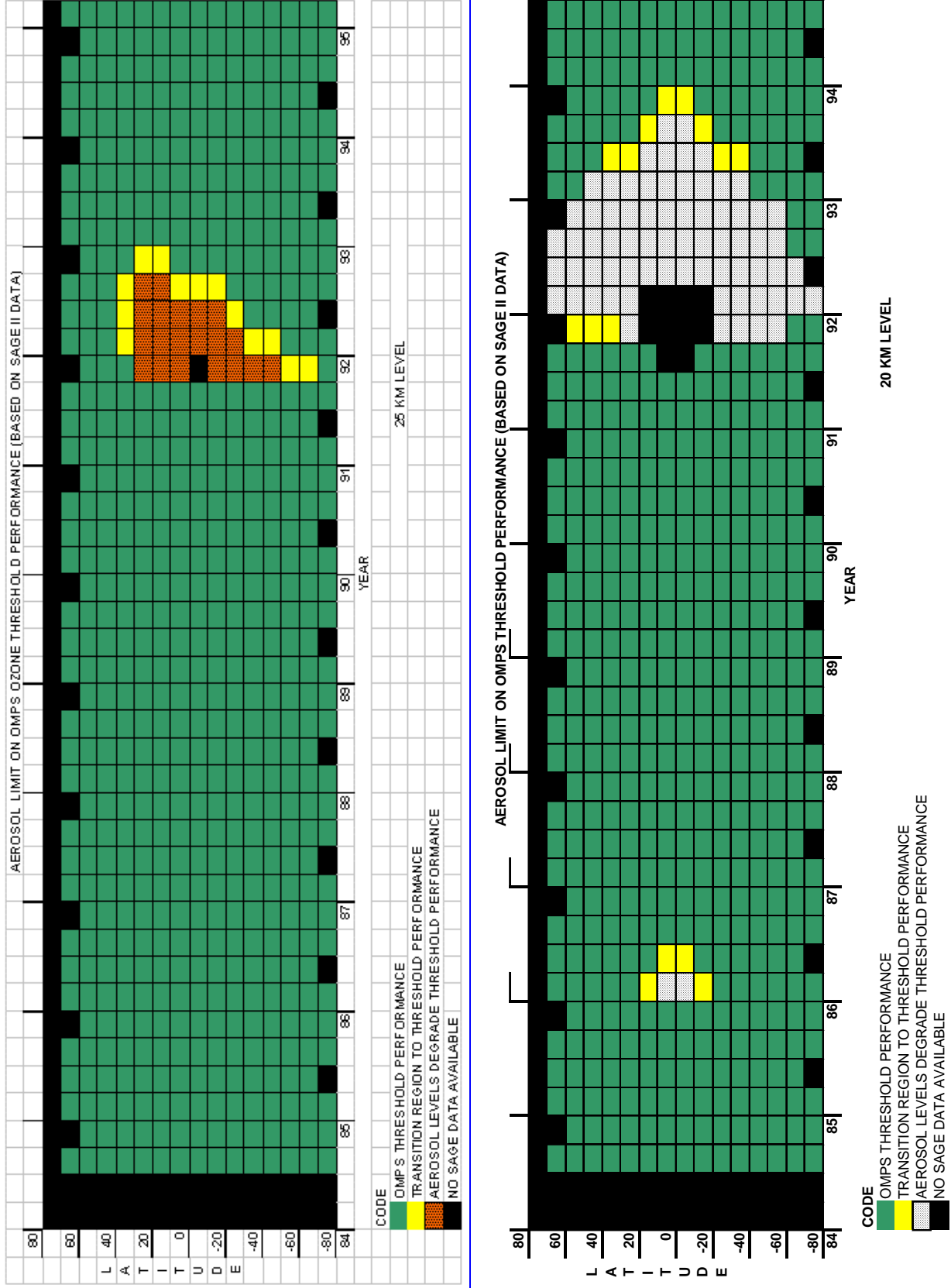
We used these simulated results with the SAGE II global aerosol climatology database of Thomason et al. (JGR, v. 102, p. 8967, 1997) to define latitudes and time periods over which threshold precision is not met. Crossover altitudes, where the simulated random errors exceed the threshold, were plotted as a function of time for each latitude zone. These crossover altitudes were correlated with the aerosol plots of Thomason et al. (1997) in their Plate 1 (b) and (c). The results were categorized as corresponding to OMPS threshold performance (green), degraded OMPS performance (orange), and a transition region between threshold and non-threshold OMPS performance (yellow). This transition region indicates aerosol loadings that span concentrations where threshold performance is marginal.

The aerosol limits on OMPS limb profile threshold performance are indicated in Figure 8.4-7, on the next page. It shows the equivalent OMPS threshold performance as a function of time and latitude at 25 km (top) and 20 km (bottom). The dominant feature of the plots is the degraded performance immediately following the eruption of Pinatubo. Volcanic eruptions of this size occur every 100 years or so. The smaller eruption of Ruiz, appearing in the equatorial region in early 1986, produced aerosol loading typical of that observed every three years or so. Threshold degradation is limited to a small latitude region and the aerosol decays rapidly so threshold performance recovers quickly.



DRAFT

Figure 8.4-7. Aerosol Limits on OMPS Limb Profile Threshold Performance Based on SAGE II Data



9 References

- Anderson, S. M., and K. Mauersberger, Laser measurements of ozone absorption cross sections in the Chappuis band, *Geophys. Res. Lett.*, *19*, 933, 1992.
- Bass, A.M., and Paur, R.J., "The ultraviolet cross-sections of ozone: II. The measurements," Proceedings of the Quadrennial Ozone Symposium, ed. C.S. Zerefos and A. Ghazi, D. Reidel Publishing, 661-671, 1984.
- Bhartia, P.K., K.F. Klenk, C. K. Wong, D. Gordon, and A.J. Fleig, "Intercomparison of the Nimbus 7 SBUV/TOMS total ozone data sets with Dobson and M83 results," *J. Geophys. Res.* *89*, 5239-5247, 1984.
- Boughner, R., J.C. Larsen, and M. Natarajan, "The Influence of NO and CLO variations at twilight on the interpretation of Solar Occultation Measurements", *Geophysical Research Letters*, Vol. 7, No. 4, 231-234, 1980.
- Brasseur, J. *Geophys. Res.*, *98*, 23,079, 1993
- Burkholder, J. B., and R. K. Talukdar, Temperature dependence of the ozone absorption spectrum over the wavelength range 410 to 760 nm, *Geophys. Res. Lett.*, *21*, 581, 1994.
- Caudill, T.R., D.E. Flittner, B.M. Herman, O. Torres, and R.D. McPeters, "Evaluation of the pseudo-spherical approximation for backscattered ultraviolet radiances and ozone retrieval", *J. Geophys. Res.* *102*, 3881-3890, 1997.
- Chandrasekhar, S., "Radiative Transfer", Oxford University Press, London, 1950.
- Chu, W. P., and M. P. McCormick, Inversion of stratospheric aerosol and gaseous constituents from spacecraft solar extinction data in the 0.38-1.0- μ m wavelength range, *Appl. Opt.*, *18*, 1404, 1979.
- Dave, J.V., "Meaning of successive iteration of the auxiliary equation in the theory of radiative transfer," *Astrophys. J.* *140*, 1292-1303, 1964.
- Dave, J. V., Effect of aerosols on the estimation of total ozone in an atmospheric column from the measurement of its ultraviolet radiance, *J. Atmos. Sci.*, *35*, 899-911, 1978.
- DeLand and Cebula, *J. Geophys. Res.*, *98*, 12,809, 1993
- Eck et al., *J. Geophys. Res.*, *92*, 4287, 1987
- Fishman, J., et al., "Distribution of tropospheric ozone determined from satellite data", *J. Geophys. Res.* *95*, 3599-3617, 1990.
- Fleig, A.J., et al., "Nimbus 7 Solar Backscatter Ultraviolet (SBUV) Ozone Products User's Guide", NASA Reference Publication 1234, 1990.

Flittner, D. E., B. M. Herman, R. D. McPeters, E. Hilsenrath, and S. J. Janz, An algorithm for retrieving ozone profiles from shuttle observations of limb scattered UV and visible light, paper presented at AGU Spring Meeting, May 1998a.

Flittner, D. E., B. M. Herman, R. P. Loughman, R. D. McPeters, E. Hilsenrath, S. J. Janz, and P. K. Bhartia, The effect of clouds upon limb scattered radiances and the retrieval of ozone profiles using these radiances, paper prepared for the AGU Fall Meeting, December 1998b.

Fraser, R. S., and Z. Ahmad, The effect of surface reflection and clouds on the estimation of total ozone from satellite measurements. Fourth NASA Weather and Climate Program Science Review, *NASA Conf. Publ.* 2076, [NTIS N79206331 pp.247-252, 1978.

Heath, D.F. et al, *Metrologia* 30, p. 259-264, 1993.

B.M. Herman, D.E. Flittner, R.D. McPeters, and P.K. Bhartia, “Monitoring Atmospheric Ozone from Space Limb Scatter measurements”, *SPIE*, Vol. 2582, 88-99, 1995.

Herman, B.M., T.R. Caudill, D.E. Flittner, K.J. Thome, and A. Ben-David, “Comparison of the Gauss-Seidel Spherical Polarized Radiative Transfer Code with Other Radiative Transfer Codes”, *Applied Optics*, Vol. 34, No. 21, 4563-4572, 1995.

Herman, J.R., P.K. Bhartia, O. Torres, N.C. Hsu, C.J. Seftor, and E. Celarier, “Global distribution of absorbing aerosols from Nimbus-7/TOMS data”, *J. Geophys. Res.*, 102, 16911, 1997.

Herman, J.R. and E.A. Celarier, “Earth surface reflectivity climatology at 340-380 nm from TOMS data,” *J. Geophys. Res.* 102, 28003, 1997.

Hsu, N.C., J.R. Herman, P.K. Bhartia, C.J. Seftor, O. Torres, A.M. Thompson, J.F. Gleason, T.F. Eck, and B.N. Holben, “Detection of biomass burning smoke from TOMS measurements”, *Geophys. Res. Lett.* 23, 745-748, 1996.

Hsu, N.C., R.D. McPeters, C.J. Seftor, and A.M. Thompson, “The effect of an improved cloud climatology on the TOMS total ozone retrieval”, *J. Geophys. Res.* 102, 4247-4255, 1997.

Hsu, N.C., J.R. Herman, O. Torres, T.F. Eck, and B.N. Holben, “Comparisons of the TOMS aerosol index with sun photometer aerosol optical thickness: results and applications”, submitted to *J. Geophys. Res.*, 1998.

Janz, S.J. et.al., “Calibration of limb sounding instruments for ozone and environmental research”, Poster AO.2-0012, 32nd COSPAR Scientific Assembly, Nagoya, Japan, 12-19 July, 1998.

Janz, S.J., E. Hilsenrath, D. Flittner, and D. Heath, “Rayleigh Scattering Attitude Sensor”, *SPIE*, Vol. 2831, 146-153, 1996.

Jaross, G. et al., “Calibration and postlaunch performance of the Meteor 3/TOMS instrument”, *J. Geophys. Res.* 100, 2985—2995, 1995.

Joiner, J. and Bhartia, P.K., *J. Geophys. Res.*, 100, 23,019, 1995



Joiner, J., Bhartia, P.K., Cebula, R.P., Hilsenrath, E., and McPeters, R.D., "Rotational-Raman Scattering (Ring Effect) in Satellite Backscatter Ultraviolet Measurements", *Appl. Opt.*, 34, 4513-4525, 1995.

Klenk, K.F., P.K. Bhartia, A.J. Fleig, V.G. Kaveeshwar, R.D. McPeters, P.M. and Smith, "Total ozone determination from the backscattered ultraviolet (BUV) experiment," *J. Appl. Meteorol.* 21, 1672-1684, 1982.

King, L.V., "On the complex anisotropic molecule in relation to the dispersion and scattering of light," *Pro. Roy. Soc. A* 104, 333-357, 1923.

Klenk, K.F., et al., "Total ozone determination from the backscattered ultraviolet (BUV) experiment", *J. Appl. Meteorol.* 21, 1672, 1982.

Klenk, K.F., et al., "Standard ozone profiles from balloon and satellite data sets," *J. Climate Appl. Meteorol.* 22, 2012-2022, 1983.

Liou, K.N., "An Introduction to Atmospheric Radiation", *International Geophysics Series, Vol 26*, Academic Press, 1980.

McPeters, R.D., A.J. Krueger, P.K. Bhartia, J.R. Herman, A. Oaks, Z. Ahmad, R.P. Cebula, B.M. Schlesinger, T. Swissler, S.L. Taylor, O. Torres, C.G. Wellemeyer, "Nimbus-7 Total Ozone Mapping Spectrometer (TOMS) Data Products User's Guide," *NASA Reference Publication 1323*, Nov (1993).

McPeters, R.D., "The Atmospheric SO₂ Budget for Pinatubo Derived from NOAA-11 SBUV/2 Spectral data," *Geophys. Res. Lett.* 9, 1971-1974, 1993.

McPeters, R.D., P.K. Bhartia, A.J. Krueger, J.R. Herman, B.M. Schlesinger, C.G. Wellemeyer, C.J. Seftor, G. Jaross, S.L. Taylor, T. Swissler, O. Torres, G. Labow, W. Byerly, and R. P. Cebula, "Nimbus-7 TOMS Ozone Mapping Spectrometer (TOMS) Data Products User's Guide", *NASA Reference Publication 1384*, Apr (1996).

McPeters, R. D., The behavior of ozone near the stratopause from two years of BUV operations, *J. Geophys. Res.*, 85, 4545-4550, 1980.

Rinsland, C.P., R.E. Boughner, J.C. Larsen, A. Goldman, F.J. Murcray, and D.G. Murcray, "Stratospheric NO + NO₂ Profiles at Sunset from Analysis of High Resolution Balloon-Borne Infrared Solar Absorption Spectra Obtained at 33N and Calculation with a Time-Dependent Photochemical Model," *NASA TM-86285*, August, 1984.

Rodgers, C.D., "Retrieval of Atmospheric Temperature and Composition from Remote Measurements of Thermal Radiation", *Reviews of Geophysics and Space Physics*, Vol. 14, No. 4, 609-624, 1976.

Seftor, C.J., N.C. Hsu, J.R. Herman, P.K. Bhartia, O. Torres, W.I. Rose, D.J. Schneider, and N. Krotkov, "Detection of volcanic ash clouds from Nimbus-7/TOMS", *J. Geophys. Res.* 102, 16749-16759, 1997.



Seftor, C.J., S.L. Taylor, C.G. Wellemeyer, Z. Ahmad, "Estimated Error in Nimbus 7 TOMS and SBUV Total Ozone Retrieval due to Differences in Profile Shape from Standard Profiles," *Hughes STX Contractor's Report #HSTX-3036-108-CS-93-005*, 1993.

Thomason et al. (JGR, v. 102, p. 8967, 1997)

Torres, O., P.K. Bhartia, J.R. Herman, Z. Ahmad, and J. Gleason, "Derivation of aerosol properties from satellite measurements of backscattered ultraviolet radiation: Theoretical Basis", *J. Geophys. Res.* 103, 17099, 1998.

Wellemeyer, C.G., S.L. Taylor, G. Jaross, M.T. Deland, C.J. Seftor, G. Labow, T.J. Swissler, and R.P. Cebula, "Final report on Nimbus-7 TOMS Version 7 calibration", *NASA Contractor Report 4717*, March (1996).

Wellemeyer, C.G., S.L. Taylor, C.J. Seftor, R.D. McPeters, P.K. Bhartia, "A correction for TOMS profile shape errors at high latitude", *J. Geophys. Res.*, submitted (1996).

Wellemeyer, C.G., et al., *J. Geophys. Res.* 102, p. 9020, 1997.

Wieser, M., 1987, "The global digital terrain model TUG87," Internal Rept on Set-up, Origin and Characteristics, Institute of Mathematical Geodesy, Technical University of Graz, Austria.

Woods, T.N., et al., "Validation of the UARS Solar Ultraviolet Irradiances: Comparison with the ATLAS-1, -2 Measurements," *J. Geophys. Res.*, submitted.



APPENDIX A. SOURCE CODE

SDR Production

The baseline design of the SDR generation software will be based on the TOMS science data processing system. A description of the code design and the processing flow is contained in the document **sdrngen.doc**.

The source code used to generate Level 1 data products (equivalent to SDRs) for the TOMS data is contained in the file **psdr.zip**.

EDR Production

This software package constitutes the code developed during the OMPS risk reduction phase for the limb profiler. The source code is contained in the file **ball_omps_lim_Mar299.tar.gz**.

1) Software Development Environment

The code was developed on an SGI O2 workstation. The code is written in F77 and IDL(v5.0).

2) Modifications Since Last WPTB Delivery

Code functionality remains the same. No modifications have been made to the forward code. Minor modifications have been made to the inverse code (IDL subroutines) to simplify the process of changing the range of tangent altitudes used in simulation/inversion modeling.

3) Functionality

A. Scene Characteristics

Although the cloud fraction and surface reflectance solution methods are coded and tested, a limitation remains with respect to independently specifying terrain altitude and cloud top altitude. At this time, both reflecting surfaces are placed at the same altitude.

Cloud fraction

Code completed and tested.

Surface reflectance

Code completed and tested.

B. Neutral number density inversion

Code completed and tested but uses single scattering kernels calculated from separate perturbation runs. Full functionality requires development of analytical kernel functions.

C. Aerosol Inversion

Not yet coded but code will be very similar to ozone, density inversions.

D. Ozone Inversion

Code is complete.

E. Multiple scattering tables

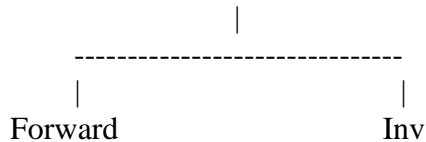
Code associated with 'mgeo' option has not been executed for OMPS. This code was part of the original code delivered by the Univ of Arizona. It contains methods to perform solar zenith angle interpolation and azimuthal angle expansion. It will be the starting point for modifying the 'lgeo' version of the tables to include angular information.

F. Field of View

Coding completed but not yet fully tested. Nominal (rectangular, triangular) functions included.

4) Directory structure

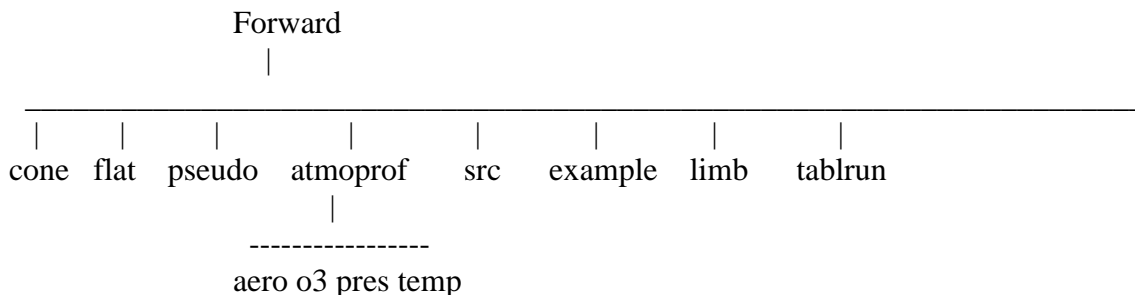
The top level structure is



The forward directory contains the plane-parallel, pseudo-spherical, and spherical versions of the polarized Herman Code. It is used primarily for multiple scattering table generation and to benchmark the inverse code counterpart. The inverse directory contains the IDL based inversion code and the radiative transfer code used by the inverse code. The inverse radiative transfer code is identical to the forward version except that it has been restructured to eliminate repetitive computations that would be performed during each iterative step.

5) Forward Code

A. Directory



cone-spherical source code
 flat-plane parallel source code
 pseudo-pseudo spherical, not used/maintained
 atmopprof-atmospheric model profiles
 src-subroutine source code
 example-flat and spherical example limb radiances
 limb-store tabulated cross-sections

tablrn-multiple scattering table generation directory

B. Execution

To compile the forward code, go to the forward directory and execute:

```
make -f lmflpnew      plane-parallel
make -f lmsspnew      spherical
```

To create sample limb radiances, go to the example directory and

edit the `exexam` file, change the directory names to suit your environment and then enter;

exexamp flp (plane-parallel)
exexamp sp (spherical)

compare results in directory test to test_sgi

after you have done this, edit `src/ray1.f` and change `lsbtop` from `TRUE` to `FALSE`

lsbtop=false means the chapman function is used to estimate atmospheric

amounts above the last defined atmosphere level. The inverse

radiative transfer model uses `lsbtop=true` but compensates for

ozone amounts above the last level by making the last level

20km above the altitude at which accurate radiances are needed.

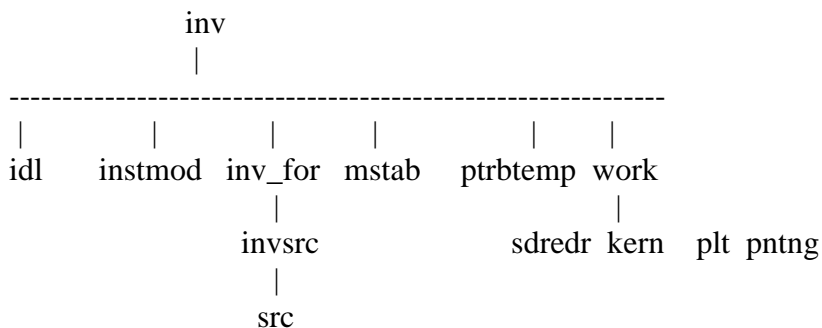
comments in the exexamp shell script describe input variables

more comments may be found in the subroutine `guinfo.f` in the `src` directory

6) Inverse Code

A. Directory Tree

The inverse directory tree is



idl- contains idl code to do simulation and inversions

instmod- instrument model, superceded by TIM snr requirements

inv for- radiative transfer code for inverse model

invsr-modified source code specific to inversion

mstab- store multiple scattering tables

ptrbtemp- contains temperature perturbation files

work- work directory

sdredr-contains simulation example
kern- calculate kernels
plt- selected plot programs for drivomp3 output
pntng- example files for drivomp3

another readme file is located in inv/work/sdredr

B. Execution

edit pathnames in idl batch files

edit pathnames in ivv.in for your set up

for a description of the ivv.in variables please see rdinfo2.pro
most of the options are listed there

to execute dosim3

enter idl

type in @b_sim3 then dosim3

output on file y.ms.new2.dat, copy to yms.thisrun

to execute maksdr

enter idl

type in @b_sdr then maksdr

output on sdr.dat

to execute edr algorithm (lim_edr_alg4.pro)

enter idl

type in @b_omp4 then lea4

output on edr.dat

yms.thisrun.TIMchans is an example output from dosim3 using the channel
set from the TIM

7) Working Code

Drivomp3 contains all the elements found in **dosim**, **maksdr**, and **lim_edr_alg** and is a little bit easier to use. Drivomp3 (**pntng** directory contains sample files) can be used to simulate and invert limb radiances. Set up the run conditions in the Ivv.in file and select the S option (2nd line) to do a simulation. Copy y.ms.new2.dat over to yms.thisrun. Edit Ivv.in and change the S to an I to run the inversion. To look at output in the form presented at the SFR, TIM, and PDR run **stdptND** and **stdpltNDV** in the **plt** directory.

To create density kernels from a perturbation analysis go to the **kern** directory and set the run conditions in Ivv.in.3pertI, execute **Drivk3 (b_k3)** and then **makwf (b_makwf)**. Copy kernel.ss.dens over to the directory where they will be used. The inversion codes can only read kernels for 1 channel. Since the

347 and 353 kernels are nearly identical little error should be introduced by this assumption. Kernels can be calculated this way for ozone and density and with a little more work on the software for aerosol also.

To study the effects of temperature errors on density and ozone cross-sections please use drivomp3. The temperature errors are selected by editing the code in iniprofs.pro to pick up the temperature perturbations stored in the ptrbtemp directory.

8) Multiple scattering tables and associated code

Multiple scattering tables were generated for the H125, H175, H225, H325, H575, L225, L325, M125, M175, M225, M325, M575 model atmospheres for 7 view angle angles each. The tables are located in the **inv/mstab** directory.

A. Directory Structure

```
tablrn
|
lgeo
|
p4    directory to store all 4 pressure limb
      radiances

M325_BGaer
|
f1p files-limb radiances
```

B. Execution

Instructions

- 1) Set run conditions in extimp4_M325
- 2) Execute extimp4_M325 or extimp4__all to do a series of atmospheres
- 3) Copy the file mstabp4M325 from the current directory to the lgeo directory. This file contains the list of limb radiance files created by the shell script
- 4) cd to lgeo
- 5) edit exmstlgeo to match the run conditions used in the shell script
- 6) execute exmstlgeo
- 7) copy the multiple scattering table mstab to the inv/mstab directory for the inversion code to access

Directory paths may have to be edited to match your setup

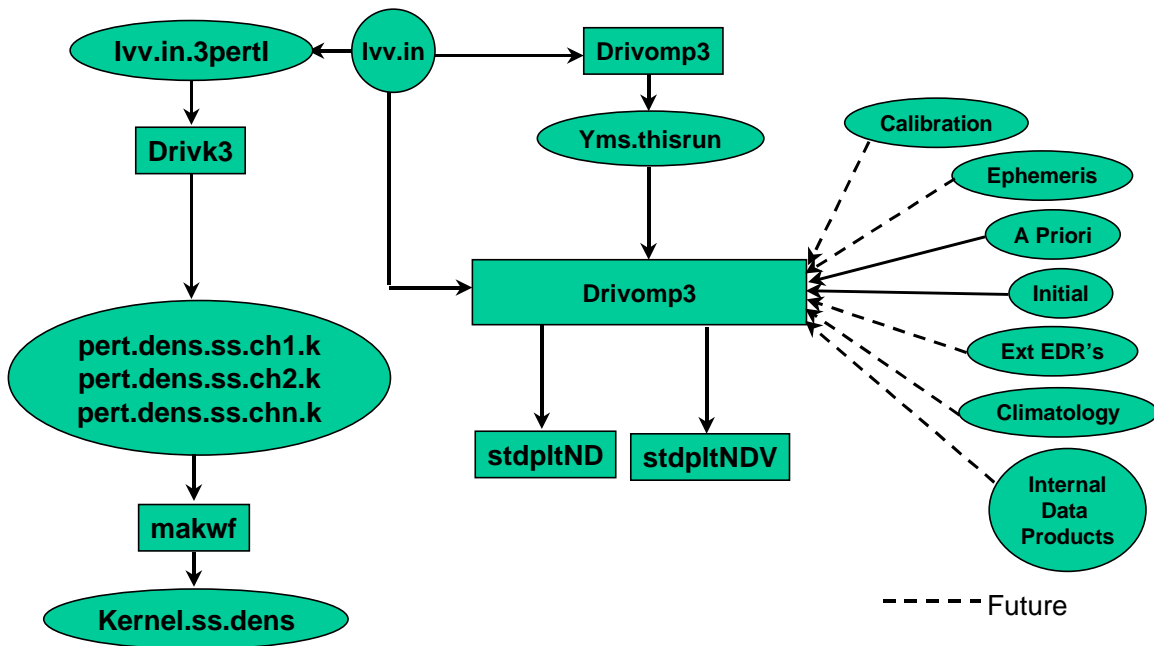


Figure A-1. Limb Profiler working algorithm modules.

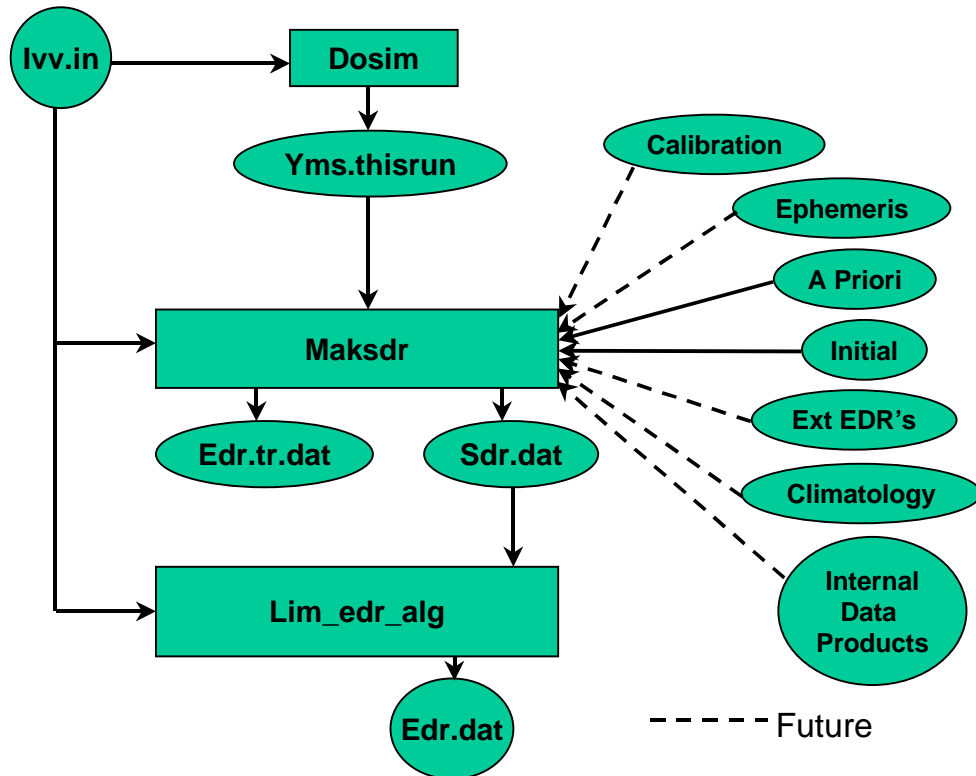


Figure A-2. Limb Profile Algorithm flow diagram.